Titre: Title:	Mechanical Behavior of a Triaxially Braided Textile Composite at High Temperature
Auteur: Author:	Amine El Mourid
Date:	2014
Type:	Mémoire ou thèse / Dissertation or Thesis
Référence: Citation:	El Mourid, A. (2014). Mechanical Behavior of a Triaxially Braided Textile Composite at High Temperature [Thèse de doctorat, École Polytechnique de Montréal]. PolyPublie. https://publications.polymtl.ca/1562/

URL de PolyPublie: PolyPublie URL:	https://publications.polymtl.ca/1562/
Directeurs de recherche: Advisors:	Martin Lévesque, & Ganesan Rajamohan
Programme: Program:	Génie mécanique

UNIVERSITÉ DE MONTRÉAL

MECHANICAL BEHAVIOR OF A TRIAXIALLY BRAIDED TEXTILE COMPOSITE AT HIGH TEMPERATURE.

AMINE EL MOURID
DÉPARTEMENT DE GÉNIE MÉCANIQUE
ÉCOLE POLYTECHNIQUE DE MONTRÉAL

THÈSE PRÉSENTÉE EN VUE DE L'OBTENTION
DU DIPLÔME DE PHILOSOPHIÆ DOCTOR
(GÉNIE MÉCANIQUE)
OCTOBRE 2014

UNIVERSITÉ DE MONTRÉAL

ÉCOLE POLYTECHNIQUE DE MONTRÉAL

Cette thèse intitulée:

MECHANICAL BEHAVIOR OF A TRIAXIALLY BRAIDED TEXTILE COMPOSITE AT HIGH TEMPERATURE.

présentée par: EL MOURID Amine
en vue de l'obtention du diplôme de: Philosophiæ Doctor
a été dûment acceptée par le jury d'examen constitué de:

M. LABERGE-LEBEL Louis, Ph.D., président
M. LÉVESQUE Martin, Ph.D., membre et directeur de recherche
M. GANESAN Rajamohan, Ph.D., membre et codirecteur de recherche
Mme DANO Marie-Laure, Ph.D., membre
Mme LAFARIE-FRENOT Marie-Christine, Docteur ès sciences, membre

DEDICATION

To my father,
Mohammed El Mourid,
who always believed in me

ACKNOWLEDGEMENTS

I would like to first thank Pr. Martin Lévesque and Pr. Rajamohan Ganesan for their guidance and trust throughout this project. Your confidence allowed me to explore hypotheses that made my work interesting, challenging and, I hope, useful.

I would like to acknowledge the contributions of my coworkers on this project, Francois Landry, Simon Dulong and Thibaut Crochon at École Polytechnique de Montréal, John Montesano and Marina Selezneva at Ryerson University in Toronto. The technical advice and support of Benedict Besner, Isabelle Nowlan and Antoine Bouchard (Polytechnique) is also gratefully acknowledged.

I would like to thank the Consortium for Research and Innovation in Aerospace in Quebec (CRIAQ), Rolls Royce Canada and Pratt & Whitney Canada (PWC) for financially supporting this project. I would also like to thank Stephen Caulfeild for welcoming me for a two months internship at PWC. I would also like to thank The Natural Sciences and Engineering Council (NSERC) and the Fonds de Recherche du Quebec - Nature et Technologies for the scholarships I obtained during my PhD studies.

Finally, I would like to express my gratitude to my family and my friends for supporting me throughout the good and bad times for the past years. I could not have done it without you.

RÉSUMÉ

L'utilisation de composites à matrice polymère (CMP) dans l'industrie aéronautique est aujourd'hui une réalité incontournable, tel qu'illustré par les matériaux utilisés dans le Boeing 787 ou le C-series de Bombardier. Ces matériaux, qui possèdent un rapport de rigidité/masse avantageux ainsi qu'une grande flexibilité de propriétés, représentent d'excellents candidats pour des applications de haute performance. En particulier, les composites textiles offrent une grande diversité mécanique résultant du choix de matériau pour les fibres et la matrice, ainsi que de l'agencement de l'architecture textile. Cependant, les CMP sont habituellement restreints à des applications à température ambiante, à cause des faibles propriétés mécaniques de la matrice à haute température.

Le développement de matrices polymère possédant une meilleure résistance à la température crée de nouvelles opportunités pour les CMP, notamment pour les moteurs d'avions. Cependant, le comportement mécanique de la matrice varie en fonction de la température et du temps. De ce fait, les CMP peuvent exhiber un comportement viscoélastique à haute température et être sujets au vieillissement physique et chimique en présence d'un environnement oxydant. Les interactions entre le comportement de la matrice et l'architecture du composite textile doivent être analysés avant de concevoir des pièces avec ces matériaux.

L'objectif principal de cette thèse était de comprendre l'influence de la température, de la viscoélasticité et du vieillissement sur les propriétés mécaniques d'un composite textile tressé. Le matériau étudié est un composite tressé carbone/MVK10 dont les torons sont orientés à $0°/\pm 60°$.

La première étape consistait à développer un cadre d'homogénéisation analytique et numérique afin de prédire le comportement viscoélastique de textiles tissés et tressés. Des simulations ont été réalisées pour plusieurs fractions volumiques et rapports de contraste, en utilisant le modèle numérique comme base de vérification pour les modèles analytiques. L'étude a démontré que le modèle Mori-Tanaka tenant compte de l'ondulation des torons était le plus approprié pour évaluer les propriétés de composites textiles viscoélastiques.

Lors de la deuxième étape, l'influence de la température sur l'endommagement du textile tressé carbone/MVK a été étudiée dans deux directions afin de tenir compte de l'anisotropie du matériau. Une série de tests de traction fut réalisée sur des échantillons de composite à température ambiante et à température de service. Une technique de réplication fut utilisée afin de surveiller l'évolution des fissures à la surface du matériau. Par la suite, la distribution des contraintes dans les torons a été évaluée à l'aide de modèles analytiques et numériques. Une nouvelle approche de maillage a été utilisée pour obtenir un Volume Élé-

mentaire Représentatif de la structure. L'étude a permis de réaliser qu'à haute température, les propriétés élastiques transverses et de cisaillement des torons diminuent, engendrant une redistribution des contraintes au sein de l'architecture textile. Cette redistribution affecte les modes de rupture du composite ainsi que la progression de l'endommagement. L'étude a aussi montré le potentiel des modèles analytiques et numériques à expliquer les modes de ruptures au sein de l'architecture textile.

La troisième étape consistait à évaluer l'influence des vieillissements chimiques et physiques sur les propriétés mécaniques du composite textile. L'observation de coupes et de bords des échantillons a permis de suivre l'évolution de l'endommagement dû au vieillissement, sans chargement mécanique. Par la suite, des essais de traction on permis d'évaluer les changements de rigidité et de résistance mécaniques. À la température de service, le vieillissement physique était négligeable alors que le vieillissement chimique avait une influence considérable sur la résistance mécanique des échantillons testés. Après un mois de vieillissement, des fissures sont apparues sur les torons transverses à la direction de coupe. La densité et la profondeur des fissures ont cru tout au long du vieillissement, causant une réduction significative de la résistance en traction ultime. L'oxydation des surfaces libres des échantillons était à l'origine de l'apparition des fissures causant la diminution des propriétés mécaniques. Cependant, la rétention des propriétés mécaniques du composite comportant la matrice MVK10 est similaire aux composites contenant la matrice PMR15 étudiée dans la littérature. De ce fait, les composites à matrice MVK10 peuvent être utilisés pour des applications structurelles à haute température, si leurs limites sont prises en compte lors de la conception.

ABSTRACT

Polymer Matrix Composite Materials (PMCMs) have gained increasing attention from the aerospace industry over the past several years, as illustrated by their increased use in aircraft, like the Boeing Dreamliner or the Bombardier C-series. Their high strength to weight ratio, combined with the possibility to tailor their properties, provides great opportunities for the replacement of traditional materials, such as steel and aluminum.

Textile composites can yield a broad range of mechanical properties, depending on matrix and fibres properties, fibres orientation and distribution within the composite, and the yarns volume fraction. In particular, carbon fibres provide high tensile modulus and strength, when compared to other reinforcing fibres. The yarns interlacing provides additional impact resistance. However, the use of these materials is usually restricted to low temperature applications due to the matrix properties degradation with temperature.

The development of new temperature resilient polyimide matrices paved the way for new applications for PMCMs, especially in the gas turbine industry. In high temperature oxidative environments, the matrix properties degradation can significantly affect the composite's overall mechanical behaviour, even if the fibres can safely withstand much higher temperatures. Of particular interest are structural components exposed to temperatures of up to 300°C under permanent regimes. The literature has shown that PMCMs behaviour at elevated temperatures depends on the reinforcement specific architecture as well as the matrix' thermal stability.

The work presented in this thesis aimed at understanding the influence of viscoelasticity, temperature and aging on the mechanical behaviour of a textile composite using experimental, analytical and numerical tools. The studied material was a triaxially braided composite with fibres in the $0°/\pm 60°$ directions. The yarns were made of carbon fibres, embedded in an MVK10 temperature resistant polyimide matrix. The first step consisted in developing analytical and numerical frameworks to predict viscoelastic behaviour in textile composites. Simulations were performed for both braided and woven textile architectures, at different stiffness contrasts and yarns volume fractions. The analytical framework accuracy was verified with the help of the numerical simulations. An important finding of this study was that the analytical framework, combined with the Mori-Tanaka model, leads to relatively accurate predictions for both the permanent and transient parts. Therefore, the authors believe that the Mori-Tanaka model with an adjusted aspect ratio to take into account yarn curvature is reliable for predicting viscoelastic behaviour in textile composites. The textile composite that was studied in this project did not display viscoelastic behaviour, due to the high yarn volume

fraction. However, the framework remains relevant for higher temperature applications or lower yarn volume fractions.

The second step was to investigate the temperature effect on the tensile behavior of the carbon/MVK10 triaxially braided composite material studied in this project. To achieve this goal, a series of room and high temperature tensile tests on both matrix and composite samples were performed. The tests on composite samples were performed along two different material directions at the maximum service temperature allowed by the Federal Aviation Administration for aircraft components, and a dedicated replication technique was developed in order to track crack densities as a function of loading, for both test temperatures. Then, both analytical and numerical homogenization models were used to quantify the stress distribution at the yarns level as a function of the applied temperature. Finally, the homogenization models were used to explain the failure mechanisms obtained at both temperatures, for the two material directions tested. The study revealed that the impact of the temperature on the failure mechanisms of the textile composite was dependent on the loading direction. It was observed that the yarns and matrix were more compliant at high temperature, especially for the transverse and shear properties. These changes had negligible effects on the elastic properties of the composite in both directions. However, they created local stress redistributions at the yarns level, which in turn affected the ultimate tensile strength of the composite. The concentration of stress in specific yarns decreased the UTS of the composite and changed the damage profile during loading. The analysis showed the potential of analytical and numerical models to explain failure paths in textile composites. At high temperature, the evolution in the constituent elastic properties was responsible for the changes in the stress profile in the material.

The final step consisted in the study of the aging effect on the tensile strength and the failure mechanisms of a carbon/MVK10 triaxially braided composite for two material directions. The damage evolution was monitored with the help of edge and cross-section microscopical observations. At the maximum service temperature, the effect of physical aging on the composite's stiffness and density was negligible while the effect of chemical aging was gradually detrimental to the UTS. It was found that the UTS decreased by 30% in Direction 1 and by 20% in Direction 2 after 9 months of aging. Cracks initiated after 1 month of aging, preferentially on the edge surfaces of the specimen and grew inward as aging time increased. The yarns that were transverse to the sample cutting direction acted as catalyst to the aging process, creating anisotropy in the reduction of mechanical properties. Thermal oxidation was the main agent behind UTS degradation in the triaxially braided composite, causing the initiation of transverse cracks on transverse yarns at the surface of the specimen. The crack density and depth increased during aging, further weakening the material. The

FAA requirement for a maximum service temperature is suitable to prevent physical aging. However, it does not prevent UTS degradation caused by chemical aging when fibres are in contact with the oxidizing environment. Nevertheless, the MVK10 matrix tested in this work exhibited relative properties retention similar to that of PMR15, which might make this matrix a suitable replacement.

TABLE OF CONTENTS

LIST OF TABLES

LIST OF FIGURES

LIST OF APPENDICES

LIST OF SYMBOLS AND ABBREVIATIONS

Symbols

$\mathbf{A}(\boldsymbol{x})$	Local strain localization tensor
$\mathbf{A}_i$	Average strain localization tensor over phase "i"
$\mathbf{B}(\boldsymbol{x})$	Local stress concentration tensor
$\mathbf{B}_i$	Average stress concentration tensor over phase "i"
$\mathbf{S}$	Eshelby's tensor
$\mathbf{T}$	dilute solution strain localization tensor
$\mathbf{C}_i$	Stiffness tensor of phase "i"
$\widetilde{\mathbf{C}}$, $\check{\mathbf{C}}$	Effective stiffness tensor
$\mathbf{C}^p$	Steady-state part of the stiffness tensor
$\mathbf{C}^t$	Permanent part of the stiffness tensor
$\tilde{\mathbf{C}}^*$	Effective stiffness tensor in Laplace-Carson space
$\mathbf{I}$	Fourth order identity tensor
$\boldsymbol{x}$	Point coordinates vector
$\boldsymbol{\varepsilon}(\boldsymbol{x})$	Local strain tensor
$\boldsymbol{\varepsilon}_i$	Strain within phase "i"
$\boldsymbol{\varepsilon}^*$	Uniform stress-free strain
$\boldsymbol{\sigma}(\boldsymbol{x})$	Local stress tensor
$\boldsymbol{\sigma}_i$	Stress within phase "i"
$\boldsymbol{\Sigma}$	Macroscopic stress tensor
$\bar{\boldsymbol{\sigma}}$	Effective stress tensor
V_f	Fibre volume fraction
V	Volume
N	Number of elements
E	Young's modulus
$E(t)$	Relaxation modulus
σ^u	Ultimate Tensile Strength
ε^u	Tensile strain
τ_i	Inverted relaxation time
(θ, ϕ, ψ)	Euler angles
λ	Curvature ratio
ρ_i	Volume fraction of phase "i"
a_1	Length of an ellipsoid

a_2	First diameter of an ellipsoid
a_3	Second diameter of an ellipsoid
$g(t)$	Prony-series function
g_n	Constant of the prony-series function
t	time
t_e	Aging time

Abbreviations

2D	Two-dimensional
3D	Three-dimensional
BMI	Bismaleimide
FBG	Fiber Bragg Grating
SBS	Short Beam Shear
DIC	Digital Image Correlation
DMA	Dynamic Mechanical Analyzer
CTE	Coefficient of Thermal Expansion
FE	Finite Elements
LCT	Laplace-Carson Transform
$mu-$CT	Computed micro-tomography
MT	Mori-Tanaka
PMCM	Polymer Matrix Composite Material
RVE	Representative Volume Element
RT	Room Temperature
HT	High Temperature
SC	Self-consistent
UD	Unidirectional
UTS	Ultimate Tensile Strength
UCS	Ultimate Compressive Strength

INTRODUCTION

Polymer Matrix Composite Materials (PMCMs) have gained increasing attention from the aerospace industry over the past several years, as illustrated by their increased use in aircraft, like the Boeing Dreamliner or the Bombardier C-series. Their high strength to weight ratio, combined with the possibility to tailor their properties, represent important incentives for the replacement of traditional materials, such as steel and aluminium.

Textile composites can yield a broad range of mechanical properties, depending on matrix and fibres properties, fibres orientation and distribution within the composite, and the yarns volume fraction. In particular, carbon fibres provide high tensile modulus and strength, when compared to other reinforcing fibres. The yarns interlacing provides additional impact resistance. However, the use of these materials is usually restricted to low temperature applications due to the matrix properties degradation with temperature.

Thermoset polymers exhibit a rubber-like behavior beyond their glass transition temperature (T_g). This mechanical properties degradation significantly undermines the composite's overall mechanical behavior, even if the fibres can safely withstand much higher temperatures. The development of new temperature resilient polyimide matrices paved the way for new applications for PMCMs, especially in the gas turbine industry. Of particular interest are structural components exposed to temperatures of up to 300°C under permanent regimes. The literature has shown that PMCMs behaviour at elevated temperatures depends on the reinforcement specific architecture as well as the matrix' thermal stability.

From 2009 to 2014, Pratt and Whitney Canada, Rolls Royce Canada, the Natural Sciences and Engineering Research Council of Canada (NSERC) and the Consortium of Research and Innovation for Aerospace in Quebec (CRIAQ) pooled their resources to fund a collaborative Research and Developement research program to study the static and fatigue properties of a braided composite submitted to high temperature under different sets of loadings. It relied on the expertise of researchers from three universities, École Polytechnique de Montréal, Concordia University and Ryerson University and from the National Research Council (NRC) - Institute for Aerospace Research in Ottawa. The research was carried by 3 PhD and 3 Masters students.

The work presented in this thesis was conducted within that framework and aims at understanding the influence of viscoelasticity, temperature and aging on the mechanical behavior of a textile composite using experimental, analytical and numerical tools. The studied material was a triaxially braided composite with fibres in the $0°/\pm 60°$ directions. The yarns were made of carbon fibres, embedded in an MVK10 high temperature polyimide matrix with

tailored temperature resistance. The study had 3 specific objectives:

- Understand the influence of viscoelasticity on the overall properties of different textile composites, with different stiffness contrasts and yarns volume fractions.
- Evaluate and understand the influence of temperature on the failure mechanisms of the triaxially braided composite studied in the project.
- Quantify the effects of physical and chemical aging on the material.

The thesis is organized as follows. The first chapter presents a literature survey on the mechanical behavior of textile composites at elevated temperatures. It details the temperature, viscoelasticity and aging dependence of composite materials and introduces analytical and numerical homogenization techniques. Chapter 2 explains the objectives and rationale of the thesis and details the scientific approach that was adopted to study the material. Chapter 3 presents a comparison between analytical and numerical homogenization techniques for viscoelastic properties predictions for textile composites. Chapter 4 details the temperature influence on the failure mechanisms for the studied composite. Chapter 5 evaluates experimentally the influence of physical and chemical aging on the composite's mechanical performance. Chapter 6 discusses the main results of the articles, as well as some additional viscoelastic and aging testing on composite samples. The contributions from this thesis are summarized and several recommendations for future works are detailed in the last chapter.

CHAPTER 1

LITERATURE REVIEW

1.1 Convention and notations

First order tensors are represented by lower bold case Roman letters (e.g., $\boldsymbol{a}$, $\boldsymbol{t}$, etc.), second order tensors by bold Greek letters (e.g., $\boldsymbol{\alpha}$, $\boldsymbol{\Theta}$, etc.) and fourth order tensors are represented by bold capital Roman letters (e.g., $\mathbf{A}$, $\mathbf{S}$, etc.). Scalars are represented by any non-bold letter. Tensorial contractions are defined as follows:

$$\begin{aligned} \boldsymbol{a} \cdot \boldsymbol{b} &= a_i b_i = c \\ \boldsymbol{\alpha} \cdot \boldsymbol{b} &= \alpha_{ij} b_j = c_i = \boldsymbol{c} \\ \boldsymbol{\alpha} : \boldsymbol{\beta} &= \alpha_{ij} \beta_{ji} = c \\ \mathbf{A} : \boldsymbol{\beta} &= A_{ijkl} \beta_{kl} = \alpha_{ij} = \boldsymbol{\alpha} \\ \mathbf{A} :: \mathbf{B} &= A_{ijkl} B_{klij} = c \end{aligned} \tag{1.1}$$

According to the modified Voigt notation, a second order tensor $\boldsymbol{\alpha}$ can be represented as:

$$\boldsymbol{\alpha} = \begin{bmatrix} \alpha_{11} \\ \alpha_{22} \\ \alpha_{33} \\ \sqrt{2}\alpha_{23} \\ \sqrt{2}\alpha_{31} \\ \sqrt{2}\alpha_{12} \end{bmatrix} \tag{1.2}$$

and a fourth order tensor $\mathbf{A}$ is represented as:

$$\mathbf{A} = \begin{bmatrix} \mathrm{A}_{1111} & \mathrm{A}_{1122} & \mathrm{A}_{1133} & \sqrt{2}\mathrm{A}_{1123} & \sqrt{2}\mathrm{A}_{1131} & \sqrt{2}\mathrm{A}_{1112} \\ \mathrm{A}_{2211} & \mathrm{A}_{2222} & \mathrm{A}_{2233} & \sqrt{2}\mathrm{A}_{2223} & \sqrt{2}\mathrm{A}_{2231} & \sqrt{2}\mathrm{A}_{2212} \\ \mathrm{A}_{3311} & \mathrm{A}_{3322} & \mathrm{A}_{3333} & \sqrt{2}\mathrm{A}_{3323} & \sqrt{2}\mathrm{A}_{3331} & \sqrt{2}\mathrm{A}_{3312} \\ \sqrt{2}\mathrm{A}_{2311} & \sqrt{2}\mathrm{A}_{2322} & \sqrt{2}\mathrm{A}_{2333} & 2\mathrm{A}_{2323} & 2\mathrm{A}_{2331} & 2\mathrm{A}_{2312} \\ \sqrt{2}\mathrm{A}_{3111} & \sqrt{2}\mathrm{A}_{3122} & \sqrt{2}\mathrm{A}_{3133} & 2\mathrm{A}_{3123} & 2\mathrm{A}_{3131} & 2\mathrm{A}_{3112} \\ \sqrt{2}\mathrm{A}_{1211} & \sqrt{2}\mathrm{A}_{1222} & \sqrt{2}\mathrm{A}_{1233} & 2\mathrm{A}_{1223} & 2\mathrm{A}_{1231} & 2\mathrm{A}_{1212} \end{bmatrix} \tag{1.3}$$

1.2 Matrix mechanical behavior

1.2.1 Polymers and polyimides for high temperature applications

Polymers are used as the matrix phase in PMCMs. They hold the reinforcing architecture together and enable load transfer between the fibres. Polymers are large molecules consisting of a repeated monomers sequence. Thermosets are a subclass of polymers in which monomers are linked by covalent bonds, in addition to the usual van der Waals bonds. Thermosets cannot be melted as a result of these covalent bonds. Polymers' mechanical properties stem from the monomers' nature and arrangement, and are usually temperature and time dependent (Brinson and Gates, 1994).

Polymers have a transition temperature below their melting point called glass transition temperature (T_g). They exhibit a rubbery behavior above this temperature, with a sharp decrease in elastic properties, while their behavior is glassy below this temperature. T_g is usually investigated with a Dynamic Mechanical Analyzer (DMA) according to ASTM D-7028 standard. T_g is typically defined in the aerospace industry as the intersection of the slopes associated with the storage modulus E' for the glassy and rubbery states, respectively.

Gas turbines applications require polymer composites able to withstand temperatures higher than 200°C and high mechanical loadings. Polyimide matrices are a unique class among thermoset polymer resins since they exhibit higher mechanical, as well as better thermal and thermo-oxidative properties (Li *et al.*, 1999). Polyimides are amorphous thermosetting polymers that exhibit very high cross-linking density, which results in a high T_g (Kirby, 1992; Talon, 2007). The development of new polyimides formulas has made high temperature polymer-reinforced composite materials contenders for structural applications. However, the synthetization and processability of such materials remain challenging (Abadie *et al.*, 2006). Even with recent advances in polyimide manufacturing, their high price constrains them to added-value and niche applications.

PMR-15 polyimide has been used in structural applications for many years due to its high maximum service temperature (288°C) and good thermo-oxidative properties. When one of its components was declared carcinogenic, new polyimide resins such as the MVK10, manufactured by Maverick Corporation, were developed in the hope of replacing it. PMR-15 properties are still standards against which new high temperature resins performance are compared to.

1.2.2 Viscoelasticity

Viscoelasticiy manifests itself as a delayed response to a mechanical stimulus (either applied stresses or strains). In a uni-axial creep test, the material is subjected to a constant

stress, with the axial strain increasing slowly over time. In a uni-axial relaxation test, a constant strain is applied and the axial stress gradually decreases over time. Constitutive theories describing viscoelastic behavior can be derived from thermodynamics' first and second laws (Biot, 1954). For an applied strain history, the stress history can be expressed as a convolution integral of the type:

$$\boldsymbol{\sigma}(t) = \int_0^t \mathbf{C}(t-\tau) : \frac{\mathrm{d}\boldsymbol{\varepsilon}}{\mathrm{d}\tau}\mathrm{d}\tau \tag{1.4}$$

where $\mathbf{C}(t-\tau)$ is the relaxation modulus, expressed as:

$$C_{ijkl}(t) = C^0_{ijkl} + \sum_{s=1}^{N} C^s_{ijkl} \exp(-t\tau_s) \tag{1.5}$$

where C^0_{ijkl} and C^s_{ijkl} are positive semi-definite and where $\tau_s > 0$. Viscoelastic materials usually behave linearly at low stress levels. In this case, different mechanical histories are linearly additive and obey Boltzmann's superposition principle (Ferry, 1980). At higher stress levels, the linear behavior does not hold anymore and a more general constitutive theory is needed. Viscoelastic behavior is heavily dependent on the material's service temperature. The increase of temperature results in an increase in the material's compliance. The so-called time-temperature superposition principle can be used to account for the influence of temperature on viscoelastic properties. This principle introduces a factor that shifts the creep compliance or the relaxation modulus from the test temperature to the reference temperature (Andrews and Tobolsky, 1951), according to:

$$E_T(t) = E_{Tr}(a_T t) \tag{1.6}$$

where E_T is the axial relaxation modulus at temperature T, E_{Tr} is the relaxation modulus at a reference temperature T_r and a_T is the temperature shift factor. Similar expressions can be obtained for the creep compliance. This equation can be used under the material simplicity assumption, which specifies that the shapes of the relaxation spectra are independent of the current material state.

1.2.3 Physical aging

Physical aging manifests itself through mechanical properties alteration, without any external loading (Brinson and Gates, 1994), and generally occurs when a material is rapidly cooled below its T_g. Below this temperature, the material is "frozen" outside its thermodynamical equilibrium, and progressively evolves towards its equilibrium state over time through polymeric chains reorientation (Brinson and Gates, 2000). This typically leads to a gradual

Table 1.1 Thermomechanical properties of PMR-15 aged at 288°C

Properties	0h	250h	500h	1000h
Young's Modulus (GPa)	1.75	1.95	1.85	2.00
UTS (MPa)	30	–	20	13

matrix stiffening, accompanied by volume contraction. Physical aging is theoretically reversible through rejuvenation, *i.e.,* heating the material above its T_g for a specific period of time. Physical aging effects can be observed through creep or relaxation loadings close to the material's T_g.

A horizontal shift factor can be introduced (Struik, 1978) to take into account the effects of aging on viscoelastic properties. This shift factor, a_{te}, can be used to superimpose aged creep compliance or relaxation modulus over an original master curve. The material's response can consequently be expressed as:

$$E_{te}(t) = E_{ter}(a_{te}t) \tag{1.7}$$

where E_{te} is the material's axial relaxation modulus at time t of for an aging time t_e. E_{ter} is the material's relaxation modulus for a reference aging time t_{er}. A similar expression can be defined for the creep compliance.

1.2.4 Chemical aging

Thermal degradation is a molecular degradation activated by heat and resulting in mechanical properties degradation. Polymers degradation is the result of monomers chains reactions (Beyler and Hirschler, 2001). The main agents during the degradation process are the chain scissions (breakage of the polymer chain) and cross-linking (new bonds formations). The presence of oxygen and heat catalyzes these reactions.

Chemical aging has been shown by many authors to significantly decrease polymers' Ultimate Tensile Strength (UTS). For example, Ruggles-Wrenn and Broeckert (2009) studied the effects of chemical aging on PMR15's mechanical properties, whose results are summarized in Table 1.1. Young's modulus increased by 14.3% while the UTS decreased by 56% after $1,000$h of aging. Surface oxidation, the main agent in chemical aging, was responsible for the apparition of surface cracks that decreased the UTS according to the authors. To the best of the author's knowledge, the study of the aging effects on the mechanical properties of other polyimides alone (*i.e.,* not parts of composites) such as the Bismaleimide (BMI) was not performed.

1.3 Composites' mechanical behavior

1.3.1 Textile composites

Textile composites are engineered materials constituted of textile preforms embedded into a resin system. The textile preforms can display woven, braided or knitted architectures. Figure 1.1 depicts woven, braided and knitted architectures and Figure 1.2 shows a woven architecture's cross-section. The textile composite's mechanical properties depend on the fibres and matrix properties, the fabric architecture as well as the fibres volume fraction.

1.3.2 Temperature effects

Federal Aviation Administration (FAA) regulations specify the maximum service temperature at which PMCMs can be used as 28°C below the fully water saturated glass transition temperature (wet-$T_g - 28$°C) to prevent drastic degradation in material properties. However, elevated temperature (*i.e.,* above 125°C) still impacts composites' behavior. For example, Odegard and Kumosa (2000) reported temperature-induced decreases in unidirectional carbon/PMR15 composites' elastic properties. Young's modulus decreased by 10% between room temperature and 316°C when the composite was loaded in the fibres direction (E_{11}). The decrease in properties was more pronounced in the transverse direction (E_{22}) and the shear modulus (G_{12}), with decreases of 27% and 80%, respectively, as can be seen from Table 1.2. Ultimate strength in the transverse (σ^u_{22}) and shear directions (σ^u_{12}) decreased

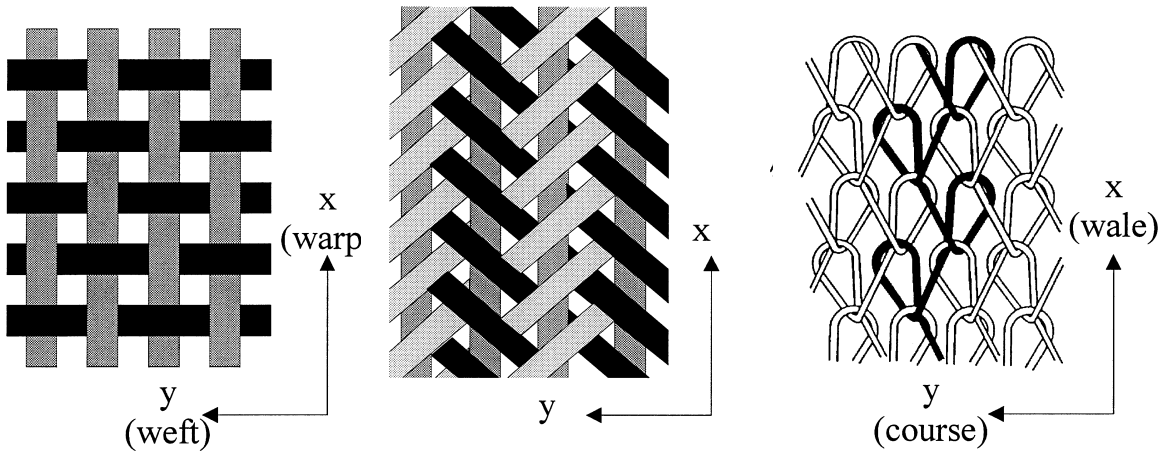

(a) (b) (c)

Figure 1.1 Textile composites architectures representing respectively a) woven, b) braided and c) knitted fabric composites (Gommers *et al.*, 1998a) .

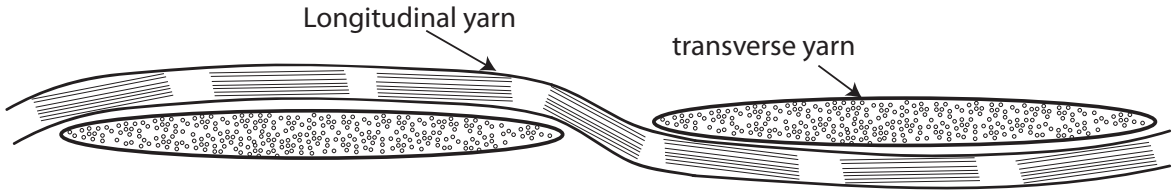

Figure 1.2 Cross-section of a woven architecture

Table 1.2 Elastic properties at different temperatures for UD carbon/PMR15 composite

Data	Room temperature	316°C	Decrease
E_{11} (GPa)	136.5	121.5	10%
E_{21} (GPa)	9.8	7.2	27%
G_{12} (GPa)	6.6	1.4	80%

significantly too, as can be seen in Figure 1.3. (Kobayashi and Takeda, 2002) studied the damage mechanisms in carbon/Bismalmeide (BMI) laminates, both at room temperature and at 180°C. They observed that matrix cracks initiated in transverse plies. However, the damage initiated earlier at high temperature and crack density at failure was lower when compared to that measured at room temperature, probably due to matrix softening.

1.3.3 Damage progression in textile composites

Damage evolution in textile composites at room temperature has been studied by many authors (Lomov *et al.*, 2008; Ivanov *et al.*, 2009) and is relatively well understood. Several damage mechanisms develop throughout the specimen as the tensile loading increases, namely:

- Damage is usually initiated by transverse cracks in transverse yarns.
- Damage propagates when the cracks size and density increase. This phenomenon is associated with a decrease in the composite's stiffness.
- The accumulation of damage creates local yarn/matrix debonding zones.
- Fibre damage causes sample failure.

These mechanisms are depicted in Figure 1.4.

The literature dealing with the high temperature failure of textile composites is, however, much more scarce. For example, Selezneva *et al.* (2011) studied qualitatively the influence

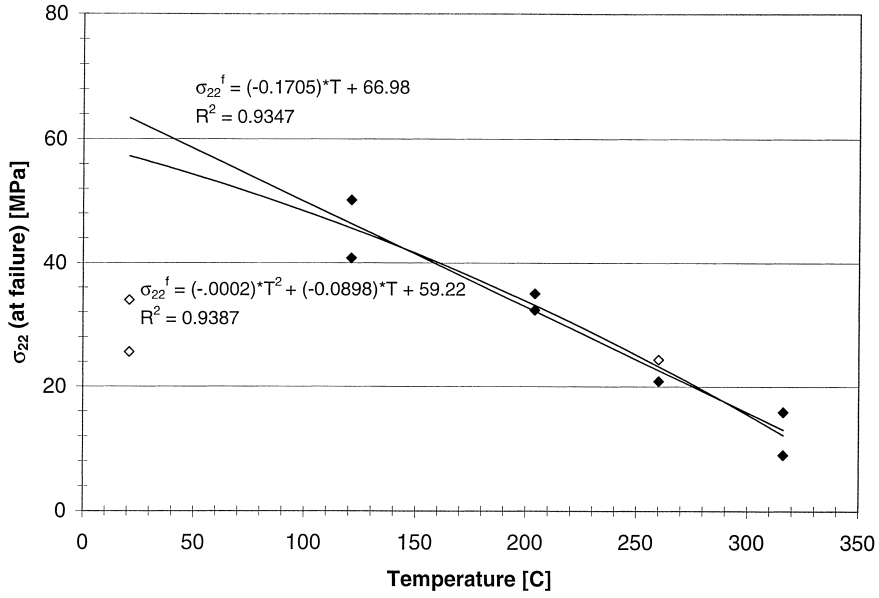

(a)

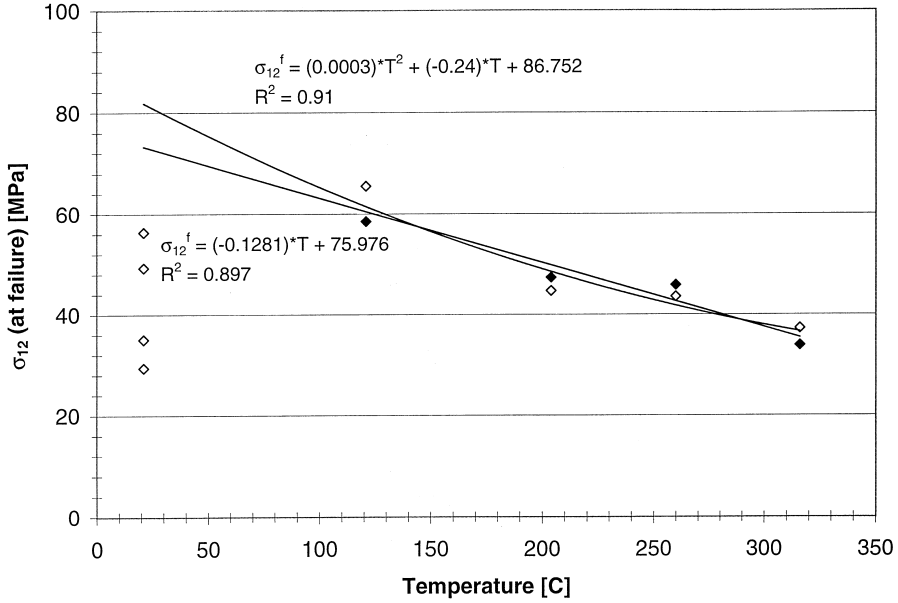

(b)

Figure 1.3 a) Transverse σ_{22}^u and b) shear σ_{12}^u strength retention for a unidirectional carbon/PMR15 composite at different temperatures. Open and solid diamonds indicate failure in grip and gage sections, respectively. (Odegard and Kumosa, 2000)

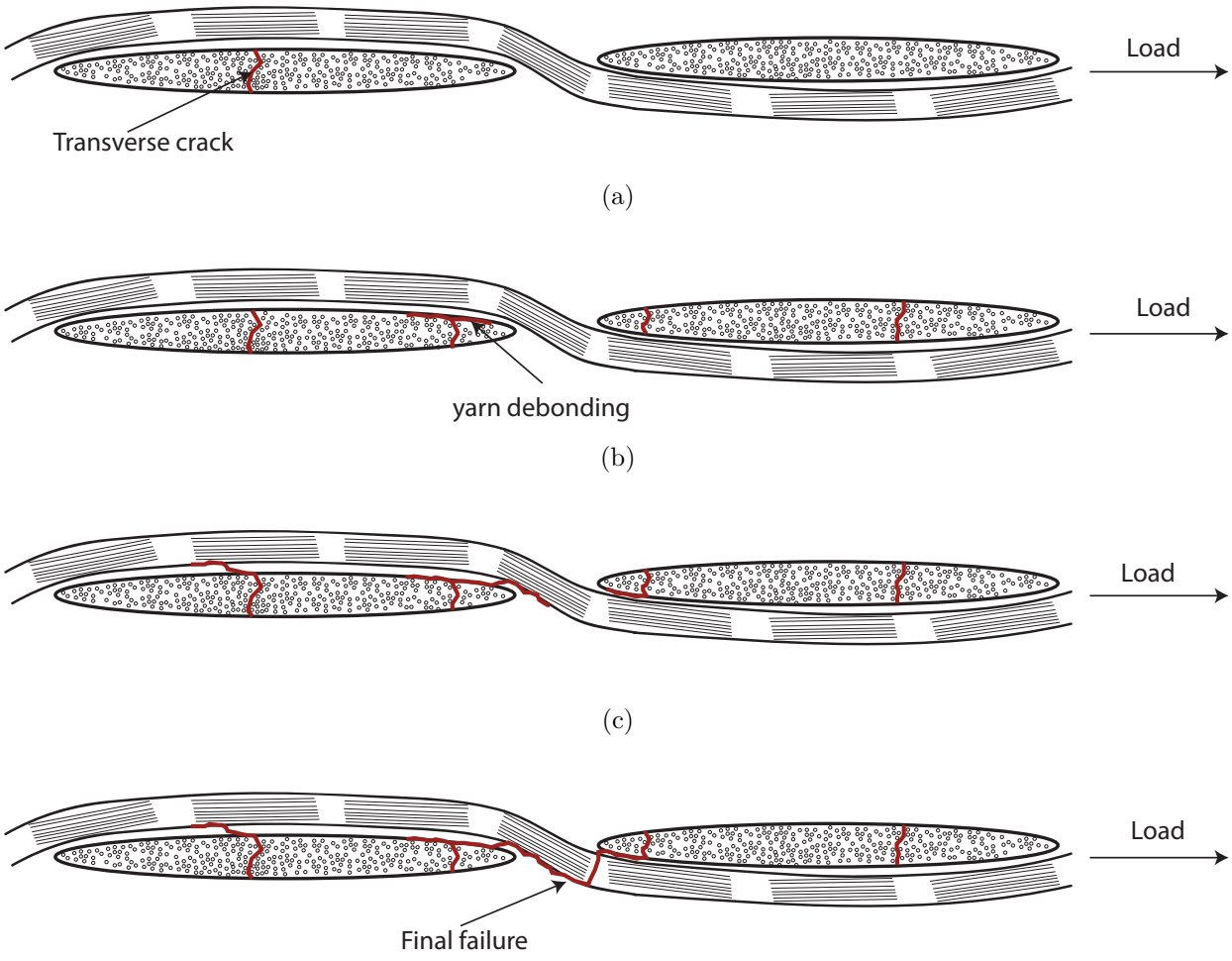

Figure 1.4 Typical failure sequence in a textile composite. a) Transverse cracks b) local yarn debonding c) Transverse cracks cause yarn debonding d) Fibre breakage and failure

of temperature on the failure of carbon/BMI off-axis woven textile composites, for temperatures ranging from 25°C to 205°C. They observed increased brittleness for samples tested at higher temperatures. Montesano *et al.* (2013) studied damage progression in a triaxially braided composite at elevated temperatures and observed fewer surface cracks on samples tested at elevated temperature. They attributed the changes in crack density to the resin's increased ductility and softening. They only performed tensile tests along straight yarns and concluded that temperature had a negligible effect on the composites' mechanical properties. However, the literature review has shown that polyimide resins exhibit a more brittle behavior at elevated temperatures (Ruggles-Wrenn and Broeckert, 2009). Bowles *et al.* (1995) studied the evolution of Ultimate Compressive Strength (UCS) in woven/PMR15 composites, at different temperatures ranging from 204°C to 316°C. As for Montesano *et al.*, they performed tests in only one material direction and concluded that temperature had a limited effect on the UCS. This survey showed the limited amount of studies on the failure of textile composites at elevated temperatures, especially for braided architectures. The damage sequence of textile composites at elevated temperatures is still not fully understood and requires more investigation.

1.3.4 Composites' damage experimental investigation

A literature survey reveals that tensile testing in different directions is the favoured method to study the failure modes of textile composites (Lomov *et al.*, 2008). Two standards dictate the testing parameters, namely:

- Standard ASTM D3039 provides most of the parameters for the tensile testing of composites. It provides guidance on the use of tabs, the measurement of elastic properties, the minimal size of the tested sample and the failure modes.
- Standard ASTM D6856 provides additional guidance on textile composites' specimens widths. The specimen's width should contain at least one Representative Volume Element (RVE) of the composite's textile architecture.

Several techniques have been used in the literature for monitoring damage in textile composites:

- Conventional strain measurement with the help of strain gages. In this case, the strain gage's dimensions should be at least the size of the Representative Volume Element (Lang and Chou, 1998). Changes in the slope of the stress-strain curve can indicate damage events.

- The acoustic emissions technique (Lomov *et al.*, 2008) is the measurement of stress waves resulting from the release of strain energy due to local failures. Changes in the rate of wave generation are qualitatively associated with different damage events.

- Full field strain mapping (Lomov *et al.*, 2008) is performed by analyzing several images of the sample at different load levels. With the help of Digital Image Correlation (DIC) techniques, a strain field is recreated on specimen's surface. This technique is useful for textile composites as the strain field may vary across the textile pattern.

- Samples' cross-sectionning and microscopical observation is a destructive characterization technique (Hayes and Gammon, 2010) that allows for observing the internal damage state. In this case, the sample is loaded to a certain level after which the test is stopped. Several cross-sections of the specimen are observed under a microscope to assess the damage level.

- Edge replication is a non-destructive characterization technique used to track cracks and has been successfully used for composites (Montesano, 2012). It relies on replicating film and acetone, or some other precision impression material (Hayes and Gammon, 2010) to create an imprint of the surface. The sample is kept in the testing apparatus while using edge replication. Several edge replicas can be performed on the same sample at different load levels to track the damage evolution on the specimen's edge.

- Embedded fiber optics can be used to evaluate strains and track damage in composite materials. Fiber Bragg gratings (FBG) are the most commonly used optical fiber sensors in compostes. In this technique, an optical fiber is embedded along the fibres in the composite and reflects specific wavelengths depending on the mechanical loading, enabling their use as strain gages (Okabe *et al.*, 2000). When damage occurs near a FBG sensor, the reflected wavelength changes. Monstesano *et al.* (2011) studied the damage in woven carbon/BMI laminates with the help of FBG sensors.

- Computed tomography and in-situ testing is a technique where the 3D architecture of the material is computed at different stages of the loading to track the damage state inside the material. In this technique, X-rays are processed to create tomographic images of layers of the material. These layers are combined to create a 3 D representation. The samples used are usually very small to fit in the testing apparatus. Na *et al.* (2012) performed in-situ testing of a woven composite to observe damage initiation and propagation inside the architecture.

The most popular technique to measure changes in material properties remains the strain measurement with strain gages or an extensometer. However, the limited amount of spa-

Table 1.3 Strength retention for several aging times for 2 composite materials

Test	Material	Aging time (months)				
		1	4	9	12	17
SBS	Celion/PMR15 (232°C)	100%	100%	96%	93%	75%
Compression	Carbon fabric/PMR15 (204°C)	100%	97 %	88%	83%	63%
Compression	Carbon fabric/PMR15 (288°C)	95%	75 %	NA	NA	NA

tial information provided by this technique requires coupling it with other damage tracking techniques. While acoustic emissions, full-field strain mapping and computed tomography techniques are promising developments, they require access to specialized and expensive equipment to obtain useful results. Edge replication and samples cross-sectioning are relatively inexpensive damage tracking techniques, that require access to a microscope only. They provide important information about the microstructural damage state and can be used to link the macroscopic events (change in strain-stress slope) to microscopic events, such as crack initiations and propagations.

1.3.5 Aging in composites

Aging can alter composites' mechanical properties at elevated temperatures (Leveque *et al.*, 2005). This phenomenon is directly linked to the matrix' aging, as carbon fibres are considered to be thermally stable for temperatures up to $1,000$°C (C. Saucier and Paillier, 2003). Two main phenomena are related to aging:

- Thermo-oxidative (chemical) aging on the surface. Chemical aging can induce cracks at the surface of the sample and promote initial failure.
- Physical aging is observed by the decrease in the volume of the composite and changes in elastic properties.

Several authors studied physical aging in PMCMs for different temperatures and laminate configurations (Brinson and Gates, 1994; Tuttle and Brinson, 1986; Bradshaw and Brinson, 1997; Brinson and Gates, 2000). They determined that physical aging can occur when samples are tested between T_g and $T_g - 35$°C, especially for thermoplastic matrices. At these temperatures, PMCMs display viscoelastic behaviors during creep tests and gradual stiffening of the material response that can be modeled with the help of a shift factor. They also observed that fibre orientation played a determining role in the magnitude of physical aging. For unidirectional laminates, shear and transverse compliance curves were the most affected by physical aging. In off-axis directions, physical aging could change the material

compliance by up to 8-12 %, which is non-negligible.
Lafarie-Frenot (2006) presented the main consequences of chemical aging on PMCMs. In an oxidizing environment, matrix shrinkage, matrix cracks, superficial matrix-fibre debonding and weight loss are all indicative of the chemical aging process. These changes can influence the material's strength in static, fatigue and thermal cycling tests (Lafarie-Frenot, 2006; Lafarie-Frenot *et al.*, 2006; Bertin *et al.*, 2010; Vu *et al.*, 2012). Nelson (Nelson, 1984) studied the decrease in Short Beam Shear (SBS) strength for graphite/PMR-15 composites, for different aging times and temperatures. Figure 1.5 shows the strength retention for samples aged at different temperatures and tested at room temperature, while Figure 1.6 shows the strength reduction for samples aged at 232°C and tested at different temperatures. A carbon fabric/PMR15 aged at 204°C and 288°C was tested under compression (Bowles *et al.*, 1995) and showed similar results to the SBS study. Aging was also studied by Leveque *et al.* (2005) for carbon/epoxy $[\pm 45^\circ]_{4s}$ unidirectional laminates. The authors performed tensile and creep tests and reported a decrease in tensile strength due to aging. The strength deterioration was explained by an increase in the matrix' brittleness, which was a consequence of the formation of a thermo-oxidative layer on the specimens' surfaces. Stress concentrations caused by the thermo-oxidative process, combined with the stress fields caused by the mismatch between Coefficients of Thermal Expansion (CTEs) of the matrix and fibres, could be the reason for the formation of surface cracks. Similar observations were made by Lowe et al. (Lowe *et al.*, 2002), who studied the influence of aging on carbon/BMI composites with a glass transition temperature of 302°C. They studied the evolution of fracture toughness over an aging period of 7 months, at 204°C and 250°C. Initially, there was an increase in the fracture toughness, followed by a significant decrease as aging time increased. They attributed the initial increase in toughness to a post-cure at aging temperature, which increases the cross-linking within the polymer. Once this process was complete, degradation due to surface thermal oxidation decreased the composite's toughness.

Finally, the influence of the fibres' presence on the thermal oxidation process was studied by several authors for PMR15 composites (Pochiraju and Tandon, 2009; Tandon *et al.*, 2006; Schoeppner *et al.*, 2007; Tandon *et al.*, 2008). The authors measured experimentally the oxidizing layer growth for isothermal aging, with the help of dark-field microscopy and provided models to estimate that phenomenon. Degradation occurred in a thin surface layer that grew with aging. Tandon *et al.* (2008) noticed that the oxidation layer thickness growth in unidirectional composites was higher along the fibre length than in the transverse direction. This oxidation resulted in fibre/matrix debonding and the apparition of matrix cracks. In conclusion, surface thermo-oxidation is the main degradation mechanism responsible for

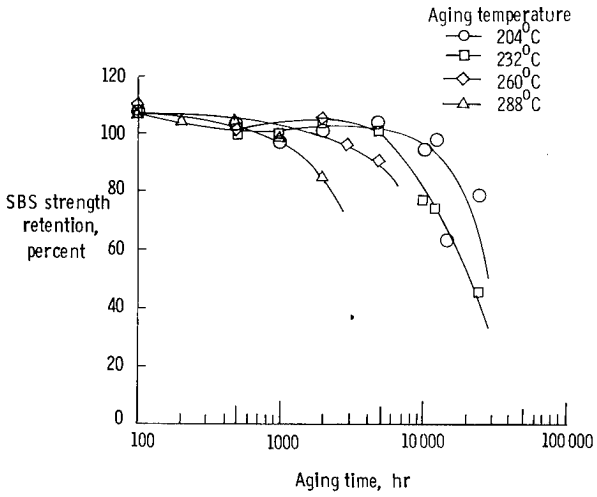

Figure 1.5 Short beam Shear Strength retention in a graphite/PMR15 composite aged at different temperatures. The specimens were tested at room temperature (Nelson, 1984)

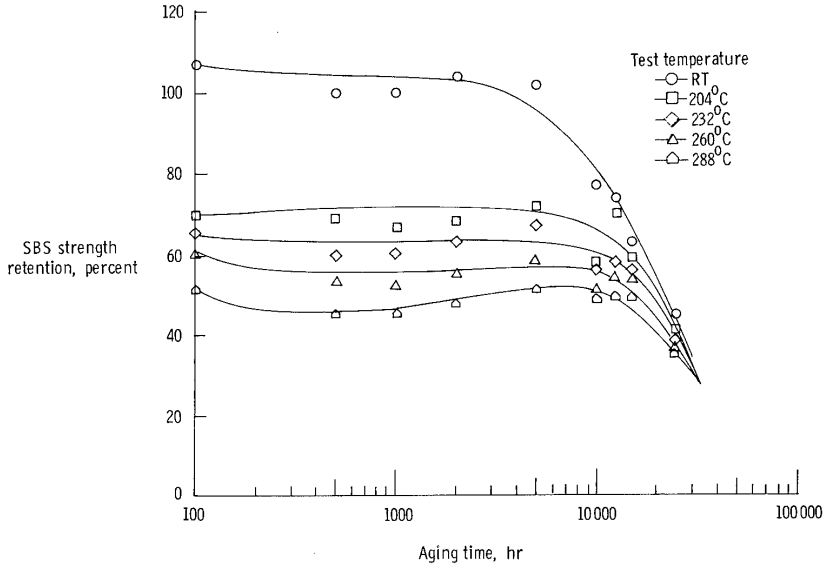

Figure 1.6 Short beam Shear Strength retention in a graphite/PMR15 composite aged at 232°C. The samples were then tested at different temperatures (Nelson, 1984)

the reported composites properties' degradation. The presence of the fibres can increase the growth rate of the oxidized layer and further deteriorate the material's UTS. This phenomenon was observed on composites with different resins (PMR15, BMI and epoxy). The decrease in UTS in different studies is summarized in Table 1.3

1.4 Homogenization

1.4.1 Analytical homogenization

Homogenization aims at predicting composites' effective elastic properties by considering the orientation, mechanical behavior and volume fraction of each constituent (Bornert *et al.*, 2001). Most homogenization techniques were developed to predict elastic behavior and were later extended to viscoelastic problems. Analytical homogenization techniques can be divided into three classes:

- Classical estimates based on the so called rule of mixtures. They rely on basic assumptions about the average stress or strain in each constituting phases. The Voigt method considers that the average strain is the same in all phases while the Reuss method is based on iso-stress assumptions for all phases (Zaoui, 2002). The Voigt and Reuss methods are known to be upper and lower bounds, respectively, of the composite's mechanical behavior. Also, these schemes do not account for the fibres' specific orientation inside the composite. Thus, composites of equal volume fractions but of different morphologies will lead to the same effective properties, according to these models.

- Energy methods based on bounds of strain energy or complementary energy functions. For example, Hashin and Shtrikman developed tighter bounds, when compared to those of Voigt and Reuss, by relying on variational principles (Hashin and Shtrikman, 1962). These bounds were developed for a random distribution of spherical inclusions. Other bounds exist for different architectures. When the contrast between the constituent phases' elastic properties is relatively large (*e.g.* when the fibres are 100 times stiffer than the matrix), most bounds are quite far apart to be useful in a design context.

- Inclusion methods based on Eshelby's solution (Eshelby, 1957) to the problem of an inclusion embedded into an infinite medium. This seminal work opened the field for what is now called *micromechanics*. The most widely used schemes are Mori-Tanaka and self-consistent techniques (Zaoui, 2002), which can be used for the homogenization of many mechanical behaviors. These techniques provide estimates instead of bounds for the composite's behavior, and can be used for many different types of ellipsoidal inclusions and orientation distributions.

Inclusion based methods provide estimates for overall composite properties as well as the strain and stresses inside each phase. The stiffness tensor of a two-phase composite using inclusion based methods is (Benveniste, 1987):

$$\tilde{\mathbf{C}} = \mathbf{C}_0 + \rho_1(< \mathbf{C}_1 : \mathbf{A} > - \mathbf{C}_0 :< \mathbf{A} >) \tag{1.8}$$

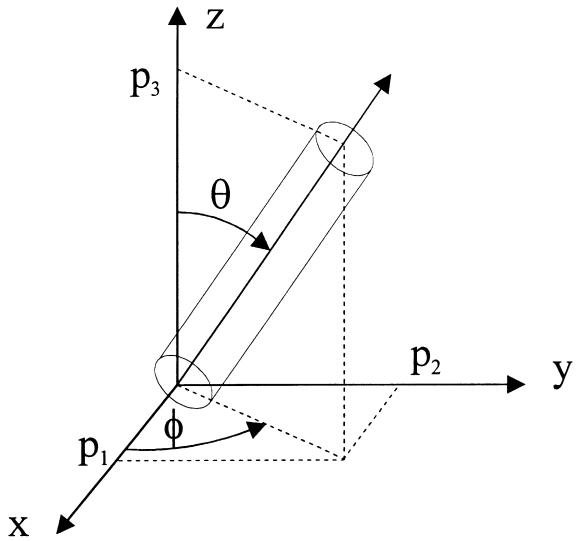

Figure 1.7 Orientation of an inclusion. Euler angles ϕ and θ describe the angular position of a vector $\boldsymbol{p}$ in space (Gommers *et al.*, 1998a).

where $\tilde{\mathbf{C}}$ is the composite's overall stiffness tensor, $\mathbf{A}$ is the so-called 4^{th} order strain localization tensor, ρ_1 the reinforcing phase's volume fraction, $\mathbf{C}_1$ the reinforcing phase's stiffness and $\mathbf{C}_0$ the matrix' stiffness. The symbol $\langle\cdot\rangle$ represents orientation averaging and is defined as:

$$\langle L_{ijkl}\rangle = \int_0^{2\pi}\int_0^{2\pi}\int_0^{\pi} \psi(\theta,\phi,\beta)\alpha_{im}\alpha_{jn}\alpha_{ko}\alpha_{lp}L_{mnop}\sin(\theta)\,\mathrm{d}\theta\mathrm{d}\phi\mathrm{d}\beta \tag{1.9}$$

where α_{im} has as its column the orthonormal basis vectors defined by the Euler angles $\{\theta,\phi,\beta\}$ shown in Figure 1.7 and ψ is an Orientation Distribution Function (ODF). The ODF represents the probability of having an inclusion oriented according to specific values of $\{\phi,\theta\,\beta\}$ and L_{mnop} is a 4^{th} order tensor. The main difference between homogenization schemes lies in the evaluation of the strain localization tensor $\mathbf{A}$, some of which are detailed in the following paragraphs.

The dilute approximation

Inclusion based methods generally rely on Eshelby's work (Eshelby, 1957) to evaluate the composite's effective stiffness tensor. Eshelby considered an ellipsoidal inclusion embedded into an infinite linearly elastic phase. The inclusion is initially stress and strain free and is afterwards loaded with a stress-free strain, like a thermal dilatation, called $\boldsymbol{\varepsilon}^*$. Eshelby

demonstrated that the resulting strain in the inclusion was uniform and computed from:

$$\tilde{\varepsilon} = \mathbf{S} : \varepsilon^* \tag{1.10}$$

where $\mathbf{S}$ is Eshelby's tensor and can be evaluated from equations given in the book by Mura (Mura, 1982). The dilute approximation assumes that the inclusions are far from each other and that they are embedded into an infinite matrix. The interaction between the inclusions is neglected and the methodology is suitable for low fibre volume fractions. The dilute solution's strain concentration tensor $\mathbf{A}_{dil}$ for a two-phase composite can be evaluated as:

$$\mathbf{A}_{dil} = [\mathbf{I} + \mathbf{S} : \mathbf{C}_0^{-1} : (\mathbf{C}_1 - \mathbf{C}_0)]^{-1} \tag{1.11}$$

The Mori-Tanaka method

The Mori-Tanaka method was developed to estimate the internal stresses in the matrix of a composite (Mori and Tanaka, 1973) subjected to external mechanical loadings. The first tensorial formulation was provided by Benveniste in 1987 (Benveniste, 1987). It has been originally designed for aligned inclusions and later extended to non-aligned reinforcements. The strain localization tensor for the Mori-Tanaka scheme $\mathbf{A}_{MT}$ is given by:

$$\begin{aligned} \mathbf{T} &= \mathbf{A}_{dil} \\ \mathbf{A}_M &= \mathbf{T} : [\rho_0 : \mathbf{I} + \rho_1 < \mathbf{T} >]^{-1} \end{aligned} \tag{1.12}$$

The Mori-Tanaka method as presented here yields a diagonally symmetrical tensor only when one of the three following conditions is met (Gommers *et al.*, 1998a):

- Isotropic inclusions.
- Perfectly aligned or randomly oriented inclusions.
- Spherical inclusions.

When the inclusions' orientations or shapes are more complex, or if there are more than two phases in the composite, the Mori-Tanaka method yields asymmetrical results, which is unacceptable since the stiffness tensor has to be symmetric for thermodynamics reasons. Ferrari proposed a reformulation of the Mori-Tanaka method that solves these asymmetry problems (Ferrari, 1990), that was first used under a tensorial formulation by Dunn (Dunn *et al.*, 1996). This reformulation respects the Hashin-Shtrikman bounds, yields the same

prediction as the traditional formulation in some cases, and is given by:

$$\begin{aligned} \mathbf{T} &= \mathbf{A}_{dil} \\ \mathbf{A}_{MT} &= \mathbf{T} : [\rho_0 : \mathbf{I} + \rho_1 \mathbf{T}]^{-1} \end{aligned} \tag{1.13}$$

Self-consistent scheme

Originally developed by Kroner and Hershey (Hershey, 1954) for polycristalline media and extended to composites (Budiansky, 1965; Hill, 1965), the self-consistent scheme assumes that the inclusions are surrounded by the composite media, which leads to the strain localization tensor $\mathbf{A}_{SC}$ being expressed as:

$$\mathbf{A}_{SC} = [\mathbf{I} + \mathbf{S} : \tilde{\mathbf{C}}^{-1} : (\mathbf{C}_1 - \tilde{\mathbf{C}})]^{-1} \tag{1.14}$$

that, when combined to Eq. 1.8, leads to

$$\tilde{\mathbf{C}} = \mathbf{C}_0 + \rho_1(< \mathbf{C}_1 : \mathbf{A}_{SC} > - \mathbf{C}_0 :< \mathbf{A}_{SC} >) \tag{1.15}$$

Equation 1.15 is implicit since the composite's stiffness tensor appears on both sides of the equation. Unless for specific cases, a numerical scheme is required to solve this equation.

1.4.2 Analytical homogenization models for textile composites

Traditionally, analytical homogenization tools developed to predict textile composites' elastic behavior were based on the rule of mixtures and the Classical Laminate Theory (CLT) (Tan *et al.*, 1997). These models, accounting for the yarns' undulations in different ways (Ishikawa and Chou, 1982; Chou and Ishikawa, 1983; Sankar and Marrey, 1997), rely on iso-stress or iso-strain distributions within the reinforcing phases. The iso-stress and iso-strain assumptions negatively affect the accuracy of these methods, especially in textile composite architectures with high fibre volume fractions and significant yarn undulations.
Gommers *et al.* (1998a) developed a methodology based on the Mori-Tanaka method to evaluate the mechanical properties of textile composites. The approach consists in approximating the yarns geometry by a series of "divided" ellipsoidal inclusions, as shown in Figure 1.8, and then use inclusion-based homogenization models for computing the composite's effective properties. Two important steps are required to define the inclusions representing the yarns. First, each ellipsoidal inclusion is defined by three characteristic dimensions a_1, a_2 and a_3. For elongated ellipsoids, a_1 defines the characteristic length while a_2 and a_3 define the cross-section. The specific yarns arrangement is then described by a discrete set of orientations.

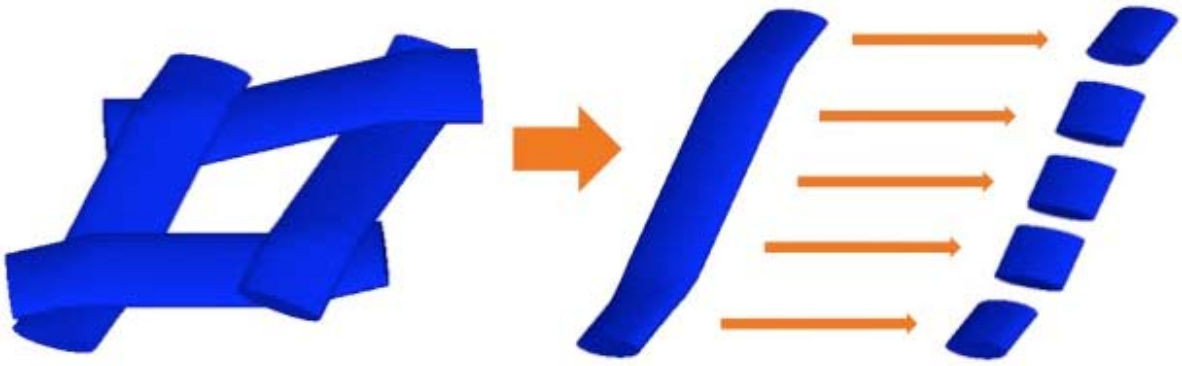

Figure 1.8 Geometrical simplification of a yarn. A single yarn divided into a series of inclusions whose orientations follow the yarns waviness.

Each inclusion is oriented according to specific values of $\{\phi, \theta\}$, as shown in Figure 1.7. The homogenized response is then evaluated with the following equations:

$$\mathbf{D} = (\mathbf{C}_1 - \mathbf{C}_0) : \mathbf{A} \tag{1.16a}$$

$$\tilde{C}_{ijkl} = C_{0_{ijkl}} + \sum_{z=1}^{N} \frac{\rho_1}{n} \alpha_{im}(\theta_z, \phi_z)\, \alpha_{jn}(\theta_z, \phi_z)\, \alpha_{ko}(\theta_z, \phi_z)\, \alpha_{lp}(\theta_z, \phi_z)\, D_{mnop} \tag{1.16b}$$

where $C_{0_{ijkl}}$ is the matrix stiffness tensor, N is the number of inclusions, α is the rotation matrix, and $\mathbf{D}$ is the stiffness contribution of each inclusion. Equation 1.16 reveals that the composite's overall stiffness is the discrete average of the orientation adjusted stiffness of each inclusion and the matrix.

1.4.3 Linear viscoelastic homogenization

Linearly viscoelastic constitutive theories are typically expressed as a convolution integral, as shown in Eq. 1.4. The convolution integral prevents using homogenization equations developed for linearly elastic problems. Many authors used the Laplace-Carson transform to circumvent the problem (Hashin, 1966, 1970; Laws and McLaughlin, 1978a; Lévesque *et al.*, 2004). The Laplace-Carson transform is defined as:

$$c^*(p) = p \int_0^t c(t) \exp(-pt) dt \tag{1.17}$$

where p is the variable in Laplace-Carson space. When the Laplace-Carson transform is applied to linearly viscoelastic constitutive equations, the relationship between strain and stress tensors becomes:

$$\boldsymbol{\sigma}^*(p) = \tilde{\mathbf{C}}^*(p) : \boldsymbol{\varepsilon}^*(p) \tag{1.18}$$

where $\boldsymbol{\sigma}^*(p)$, $\boldsymbol{\varepsilon}^*(p)$ and $\tilde{\mathbf{C}}^*(p)$ are respectively the stress, strain and the relaxation tensor in Laplace-Carson space. According to the viscoelastic correspondence principle, the Laplace-Carson domain solution to a linearly viscoelastic continuum mechanics problem is obtained by replacing the elastic properties involved in the same problem for linearly elastic materials by the Laplace-Carson transform of the linearly viscoelastic material properties. By virtue of that principle, equation 1.8 becomes:

$$\tilde{\mathbf{C}}^* = \mathbf{C}_\mathbf{0}^* + \rho_1 \left[(\langle \mathbf{C}_\mathbf{1}^* : \mathbf{A}^* \rangle - \mathbf{C}_\mathbf{0}^* : \langle \mathbf{A}^* \rangle) \right] \tag{1.19}$$

Equation 1.19 yields the effective properties in the Laplace-Carson domain only and the time-domain solution must be obtained if the effective properties are to be used into a finite element package, for example. While analytical inversion can be perfomed for very specific problems, authors have to resort to numerical inversion to obtain the time-domain solution in most situations. Several algorithms were developed in the literature (Schapery, 1962; Lévesque *et al.*, 2007; Rekik and Brenner, 2011; Brenner and Suquet, 2013) and they all rely on a Prony series approximation $\hat{g}$ to the exact solution $g(t)$ expressed as:

$$\hat{g}(t) = \sum_{n=1}^{N} g_n \exp(-t\tau_n); \tag{1.20}$$

where g_n and τ_n are constants that require optimization to fit the exact solution. In the collocation method, (Schapery, 1962) fixed one τ_n per decade and optimized the g_n so that the integral of the squared difference between $g(t)$ and $\hat{g}(t)$ is minimized. Lévesque *et al.* (2007) fixed the value of the τ_n, performed the optimization on the g_n with the condition $g_n > 0$ to respect thermodynamic conditions and provided a methodology to select the optimization points. Rekik and Brenner (2011) provided a methodology to perform the optimization on both τ_n and g_n.

1.4.4 Numerical homogenization

Numerical homogenization consists in accurately representing a material's microstructure, compute local fields induced by external loading and then compute the effective properties. The essential part of a successful simulation is the definition and the meshing of a Repre-

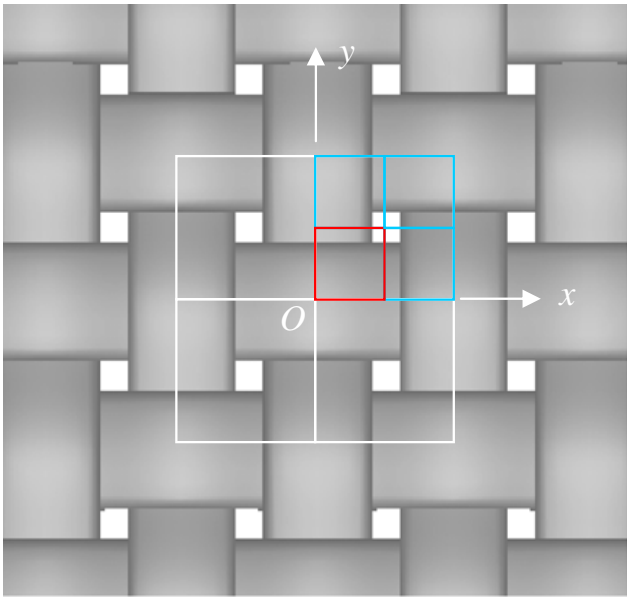

Figure 1.9 Unit cell definition in a woven composite. Each of the squares displays a possible unit cell (Li *et al.*, 2011).

sentative Volume Element (RVE) to obtain representative effective properties (Verpoest and Lomov, 2005a; Wong *et al.*, 2006; Lomov *et al.*, 2007). Because textile composites are already made of a constant and periodic (in theory at least) weaving or braiding pattern, one can find the unit cell representing the RVE intuitively. Figure 1.9 illustrates several possible unit cells of a plain weave fabric. Several integrated textile modelers, such as `Wisetex` (Verpoest and Lomov, 2005b) or `Texgen` (Robitaille *et al.*, 2003) provide efficient tools for creating solid or meshed textile RVEs that can be directly transferred to FE softwares such as `ANSYS` or `ABAQUS`.

The unit cell geometry is defined by several parameters, such as the yarns cross-sections,

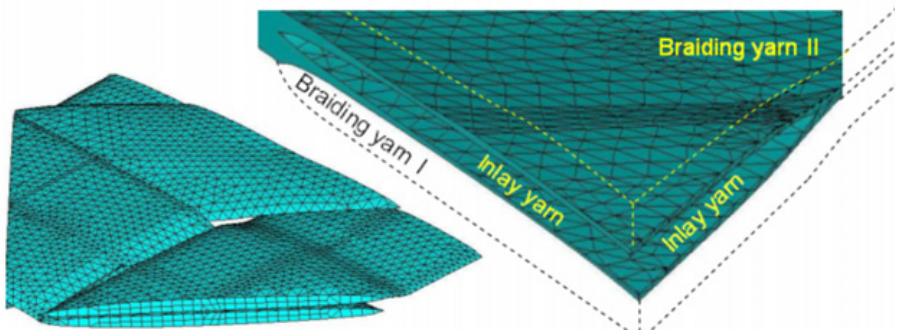

Figure 1.10 Unit cell definition in a triaxially braided composite (Lomov *et al.*, 2007).

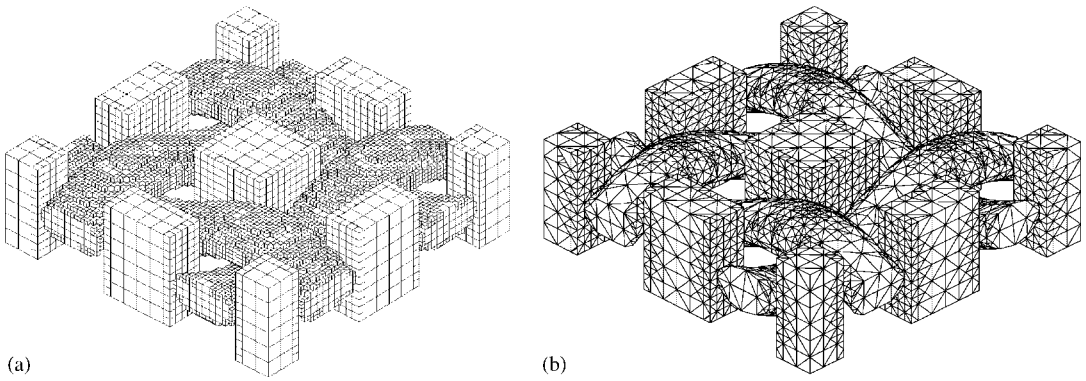

Figure 1.11 a) Voxel-based mesh and b) traditional mesh of a textile composite (Kim and Swan, 2003).

spacing, angles and arrangement. The geometrical description of the tow, consisting of the coordinates of the centerline of each yarn and their corresponding cross-sections, is created in the textile modelers with this data. Once the fibre geometry is created, it is necessary to create a matrix box that encompasses all the vaccuum between the fibres. Correct yarn interspace must be present for the matrix to be meshed. Figure 1.10 shows the meshing of the yarns and the matrix for a triaxially braided composite (Lomov *et al.*, 2007). Additional scrutiny is required for the nodes on the mesh surface boundaries, since their positioning is essential for the boundary conditions' application.

High volume fractions textile composites are quite challenging to mesh, especially for braided architectures (Lomov *et al.*, 2007), since most volume representations present yarn interpenetrations that have to be solved manually before meshing the architecture. The yarn density also creates problems for the matrix meshing due to the limited space between the yarns to create a proper matrix box. Kim and Swan (2003) relied on voxel-like meshes to address that problem. The RVE was meshed by cubic brick elements whose dimensions could potentially vary spatially to better approximate the yarns pattern. The yarns or matrix material properties were then applied to each cube of the mesh depending on its position in the geometry. Figure 1.11 shows the differences between traditional meshing and voxel like meshing for a woven composite.

The effective properties are typically obtained by applying a periodic displacement field, yielding a macroscopically applied strain. So, if a known overall strain is applied to the composite, the effective stiffness tensor $\tilde{\mathbf{C}}$ must meet the condition:

$$\bar{\boldsymbol{\sigma}} = \tilde{\mathbf{C}} : \bar{\boldsymbol{\varepsilon}} \tag{1.21}$$

Table 1.4 Unitary displacements applied to obtain the stiffness tensor and the corresponding components of the stiffness tensor.

Unitary displacement	Applied strain	Components of the stiffness tensor
1	$[0.01; 0; 0; 0; 0; 0]^T$	$\bar{C}_{11}; \bar{C}_{21}; \bar{C}_{31}; \bar{C}_{41}; \bar{C}_{51}; \bar{C}_{61}$
2	$[0; 0.01; 0; 0; 0; 0]^T$	$\bar{C}_{12}; \bar{C}_{22}; \bar{C}_{32}; \bar{C}_{42}; \bar{C}_{52}; \bar{C}_{62}$
3	$[0; 0; 0.01; 0; 0; 0]^T$	$\bar{C}_{13}; \bar{C}_{23}; \bar{C}_{33}; \bar{C}_{43}; \bar{C}_{53}; \bar{C}_{63}$
4	$[0; 0; 0; 0.02; 0; 0]^T$	$\bar{C}_{14}; \bar{C}_{24}; \bar{C}_{34}; \bar{C}_{44}; \bar{C}_{54}; \bar{C}_{64}$
5	$[0; 0; 0; 0; 0.02; 0]^T$	$\bar{C}_{15}; \bar{C}_{25}; \bar{C}_{35}; \bar{C}_{45}; \bar{C}_{55}; \bar{C}_{65}$
6	$[0; 0; 0; 0; 0; 0.02]^T$	$\bar{C}_{16}; \bar{C}_{26}; \bar{C}_{36}; \bar{C}_{46}; \bar{C}_{56}; \bar{C}_{66}$

Six independent periodic unitary displacements, presented in Table 1.4, are required for obtaining all the independent constants of $\tilde{\mathbf{C}}$. The Finite element solution of this problem provides stresses $\boldsymbol{\sigma}(\boldsymbol{x})$ in all elements. The effective stress tensor $\bar{\boldsymbol{\sigma}}$ is obtained according to:

$$\begin{aligned} \bar{\boldsymbol{\sigma}} &= \frac{1}{V}\int_V \boldsymbol{\sigma}(x)\mathrm{d}V \\ &\approx \frac{1}{V}\sum_{n=1}^{N} \boldsymbol{\sigma}_n V_n \end{aligned} \tag{1.22}$$

where N is the number of elements, $\boldsymbol{\sigma}_n$ and V_n are the stress and volume of element n respectively, and V is the total volume of the RVE.

In conclusion, several modeling techniques have been developed to numerically simulate textile composites behavior. The voxel-like meshing of a textile architecture provided by an integrated textile modeler such as `Wisetex` seems to be the most efficient methodology to obtain the RVE for high fibre volume fraction textile composites.

CHAPTER 2

OBJECTIVES AND RATIONALE

2.1 Rationale of the thesis

The general objective of this study was to assess and quantify the critical parameters governing the behavior of a carbon/MVK10 braided textile composite at elevated temperatures. In that regard, the literature survey revealed the following points :

- The use of recently developed polyimide resins requires intensive testing to determine their potential and limitations. In composites, temperature, viscoelasticity, aging and failure mechanisms are important aspects to understand and evaluate before new components are designed. The interactions between the architecture and the intrinsic properties of the matrix yield potentially intricate behaviors that require assessment.

- The failure of textile composites at elevated temperatures has only been recently studied, with the influence of anisotropy still being neglected. The reasons behind the change in failure modes due to temperature are not yet fully understood. A better grasp of the material behavior under these conditions is critical to the design of components with textile architectures.

- The durability of composite structures is of paramount importance in structural applications. Aging can have considerable effects on PMCMs' mechanical properties at elevated temperatures. It is important to assess its influence on the properties of the composite studied in this thesis.

- Several analytical and numerical tools have been used to evaluate the behavior of textile composites. However, these techniques have been mostly used to predict the elastic behavior. An assessment of the performance of these techniques is still required for more complex mechanical behaviors, such as viscoelasticity. Additionally, the Finite Element modeling of high fibre volume fraction textile composites is still challenging.

Based on the project objectives and the summary of the literature survey, 3 sub-objectives have been defined and led to 3 published/submitted journal papers, namely:

1. **Perform analytical and numerical homogenization of textile composites.**
   The first objective focused on the development of analytical and numerical frameworks

able to model linearly viscoelastic textile composites. An evaluation of the performance of analytical methods at predicting viscoelastic behavior of woven and braided composites, using FE simulations as a benchmark, was performed. The framework of textile composites elastic homogenization was extended to viscoelastic composites with the help of the correspondence principle based on Laplace-Carson Transforms. Finite Element simulations of three-dimensional woven and braided fabrics models were performed to obtain the 'exact' viscoelastic behavior. Analytical predictions were compared against the exact behavior predicted by Finite Element simulations. This study covered rigidity contrasts ranging from 10 to 80 between the Young's modulus of the matrix and that of the yarns.

The article "Comparison between analytical and numerical predictions for the linearly viscoelastic behavior of textile composites" was published in Mechanics of Materials in 2013. This journal is a forum for original scientific research on the flow, fracture, and general constitutive behavior of advanced technological and natural materials. This article was written at 85 % the author of this thesis.

2. **Understand failure mechanisms of braided textile composites at elevated temperatures.**
   The second objective investigated the mechanical properties of carbon/MVK10 braided composites at an elevated temperature. Matrix and composite samples were tensile tested at room and elevated temperature to evaluate the temperature-induced changes in the material. The damage evolution was carefully monitored at different temperatures and along different material orientations. The analytical and numerical frameworks developed in the first objective were used to explain room temperature and elevated temperature failure sequences.

   The article "Effect of temperature on the failure modes of a textile braided polymer matrix composite" was submitted to the Journal of the Mechanics and Physics of Solids in August 2014. This journal publishes original research in the field of mechanics of solids. This article was written at 85 % by the author of this thesis. The T_g determination was performed by Thibaut Crochon and the matrix specimens tensile testing was performed by the author of the thesis and Simon Dulong. Myriam Brochu initiated the author to the samples polishing and the edge replication techniques.

3. **Evaluate the durability of braided textile composites at elevated temperature.**
   The third objective consisted in monitoring, analyzing and quantifying the evolution of chemical and physical aging processes at service temperature. Composite samples were

tensile tested up to failure along two directions and for a range of aging times. The damage evolution was monitored with the help of edge and cross-section microscopical observations.

The article "Anisotropic oxidation of a triaxially braided aerospace composite and its influence on tensile failure" was submitted to Composites part B: Engineering in September 2014. This journal publishes original research on mechanics and materials science aspects of composite materials. This article was written at 85 % the author of this thesis. The matrix specimens tensile testing was performed by the author of the thesis (1 months and 4 months) and Thibaut Crochon (4 months, 9 months and 17 months). Myriam Brochu initiated the author to the samples polishing and microscopical observation techniques.

The first paper provided the analytical and numerical framework to predict the analytical and numerical behavior of textile composites. This framework was used in the second paper to predict the properties of the carbon/MVK10 triaxially braided composite studied in this project. In the second paper, the experimental procedure for samples testing at elevated temperatures was detailed. The second paper also provided the unaged matrix and composites mechanical properties, that serve as a benchmark for the aged samples in the third article.

CHAPTER 3

ARTICLE 1: Comparison between analytical and numerical predictions for the linearly viscoelastic behavior of textile composites

A. El Mourid and R. Ganesan and M. Lévesque (2013). *Mechanics of Materials*, 58 , pp. 69–83.

Abstract

Analytical homogenization techniques are developed to predict the viscoelastic behavior of textile composites. The approach consists of extending the framework of elastic homogenization of textile composites to viscoelastic composites with the help of the correspondence principle based on Laplace-Carson Transforms. Finite Element simulations of three-dimensional models of woven and braided fabrics are performed to obtain the 'exact' viscoelastic behavior. Analytical predictions are compared against the exact behavior predicted by Finite Element simulations. The results show that the analytical model based on the Self-Consistent scheme fails to deliver accurate predictions. It is also found that the method based on the Mori-Tanaka model predicts relatively well viscoelastic properties.

Keywords

Finite Element Analysis, textile composites, viscoelastic behavior, analytical models, mechanical properties

3.1 Introduction

Textile composites can be tailored for specific applications by carefully choosing the fabric type (e.g. woven, braided, knitted, etc.) or parameters (e.g. volume fraction, yarns spacing, etc.). Optimizing composites for specific applications requires accurate predictive models in order to reduce as much as possible the trials and errors involved in manufacturing and testing. When used at elevated temperatures, polymer matrix composite materials can exhibit some level of viscoelasticity. For long term applications, like in bolted joints, creep/stress relaxation can become an important issue.

Homogenization predicts the behavior of composites using microstructural information, such as fiber arrangement, fiber and matrix properties, etc. Most analytical homogenization

works for textile composites relied on the Classical Lamination Theory (CLT) (Naik and Shembekar, 1992; Tan *et al.*, 1997). These techniques provide accurate predictions for specific cases, but neglect crimp-related specificities of textile composites. Many authors worked on refined micromechanical models for predicting the elastic behavior of discontinuous reinforcements composites (see Zaoui (2002) for some examples). These techniques provide fairly accurate predictions for specific microstructures. Gommers *et al.* (1998a) extended these results to the cases of textile composites by considering the yarns as ellipsoidal inclusions and their spatial configuration as an orientation distribution function. The main advantage of this technique lied in the possibility of evaluating out-of-plane elastic constants, in addition to calculating local stresses and strains.

Numerical homogenization models estimate, with great accuracy, the effective properties of textile composites. One approach consists of meshing with Finite Elements (FE) a Representative Volume Element (RVE) of the composite. Periodic boundary conditions are applied to the RVE and the effective properties are computed by relating the spatially averaged stress and strain fields. This technique has been used by many authors for elastic behaviors (Verpoest and Lomov, 2005a; Wong *et al.*, 2006; Lomov *et al.*, 2007), but, to the knowledge of authors, viscoelastic behaviors have never been investigated with such a technique.

Homogenization of viscoelastic composites can be performed analytically by solving the homogenization equations in Laplace-Carson space with the so-called correspondence principle (Hashin, 1966, 1970; Laws and McLaughlin, 1978b; Beurthey and Zaoui, 2000; Lévesque *et al.*, 2007). This technique was recently used in combination with the CLT to predict viscoelastic behavior of woven fabrics (Upadhyaya and Upadhyay, 2011). The time domain solution is usually obtained with inversion algorithms, such as the collocation method (Schapery, 1964; Lévesque *et al.*, 2007). The recently developed method of Lévesque *et al.* (2007) is quite accurate, leads to thermodynamically admissible materials but requires a moderate computation time. Another approach consists of a time-integration approach, relying on variational principles (Lahellec and Suquet, 2007). While it avoids Laplace-Carson transforms and solves the viscoelastic problem directly in the time domain, its numerical implementation is challenging. Finally, another technique relies on a direct quasi-elastic approximation in the Laplace-Carson space (Brenner *et al.*, 2002). This method is computationally-efficient but at the expense of accuracy. Finally, Ricaud and Masson (2009) have shown that the Laplace-Carson scheme, making use of the Prony series approximation, is equivalent to a time-integration scheme of the internal variable formulation, establishing a link between the two approaches. So far, the predictions of analytical homogenization models for viscoelastic textiles based on Eshelby's solution have never been verified against FE predictions of the same microstructures.

The first objective of this paper was to extend the methodology developed by Gommers *et al.* (1998a) to evaluate the viscoelastic behavior of textile composites. The second objective was to verify the predictions of the analytical models against FE simulations of the same microstructures. Woven as well as braided fabrics were studied. The matrix was assumed to be isotropic and linearly viscoelastic while the yarns were assumed to be elastic, isotropic or transversly isotropic. A broad range of yarns properties and volume fractions were simulated in order to estimate the validity domains of the various analytical models tested.

The background required to understand analytical and numerical viscoelastic homogenization is presented at Section 2. The methodology used to compare these techniques is presented at Section 3. The performance of the models is compared for woven and braided architectures in Section 4. The paper ends with a discussion and a summary of the findings.

3.2 Background

3.2.1 Analytical homogenization models for ellipsoids-reinforced composites

The effective stiffness tensor of a two-phase composite is defined by Dunn *et al.* (1996) as:

$$\tilde{\mathbf{C}} = \mathbf{C}_0 + \rho_1(< \mathbf{C}_1 : \mathbf{A} > - \mathbf{C}_0 :< \mathbf{A} >) \tag{3.1}$$

where $\tilde{\mathbf{C}}$ is the composite's predicted stiffness tensor, $\mathbf{A}$ is the so-called 4^{th} order strain localization tensor, ρ_1 the volume fraction of the reinforcing phase, $\mathbf{C}_1$ the stiffness of the reinforcing phase and $\mathbf{C}_0$ the stiffness of the matrix. The symbol $< . >$ represents orientation averaging and is defined as:

$$< L_{ijkl} >= \int_0^{2\pi} \int_0^{2\pi} \int_0^{\pi} \psi(\theta, \phi, \beta) \alpha_{im} \alpha_{jn} \alpha_{ko} \alpha_{lp} L_{mnop} \sin(\theta) \, \mathrm{d}\theta \mathrm{d}\phi \mathrm{d}\beta \tag{3.2}$$

where α_{im} has as its column the orthornomal basis vectors defined by the Euler angles $\{\theta, \phi, \beta\}$ and ψ is an Orientation Distribution Function (ODF). The ODF represents the probability to find an inclusion oriented according to specific values of $\{\phi, \theta\, \beta\}$ and L_{mnop} is a 4^{th} order tensor. The main difference between homogenization schemes lies in the evaluation of the strain localization tensor $\mathbf{A}$. According to the Mori-Tanaka method (Benveniste, 1987), the strain localization tensor $\mathbf{A}_{\text{MT}}$ is given by:

$$\mathbf{A}_{\text{MT}} = \mathbf{T} : [\rho_0 \mathbf{I} + \rho_1 \mathbf{T}]^{-1} \tag{3.3a}$$

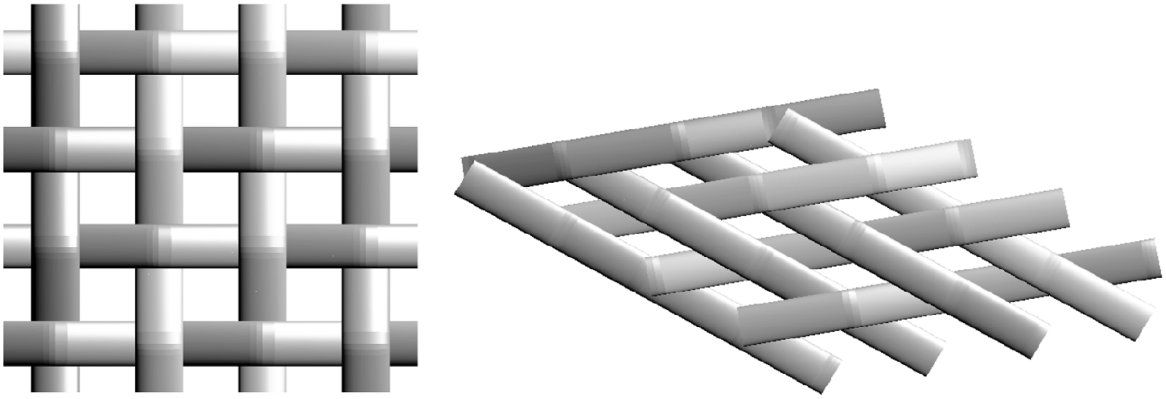

(a) (b)

Figure 3.1 Textile composite architectures representing respectively a) woven and b) braided fabric composites.

$$\mathbf{T} = [\mathbf{I} + \mathbf{E} : \mathbf{C}_0^{-1} : (\mathbf{C}_1 - \mathbf{C}_0)]^{-1} \tag{3.3b}$$

where $\mathbf{E}$ is Eshelby's tensor and ρ_0 the matrix volume fraction. It is well know that, when the orientation or the shape of the inclusions is general or if there is more than two phases in the composite, the Mori-Tanka method delivers asymmetrical stiffness tensors. Ferrari (1990) proposed a reformulation of the Mori-Tanaka method that solves asymmetry problems and that was first used in a tensorial formulation by Dunn *et al.* (1996). The strain localization tensor for the Self-Consistent scheme (Hershey, 1954; Budiansky, 1965; Hill, 1965), $\mathbf{A}_{\mathrm{SC}}$, is given by:

$$\mathbf{A}_{\mathrm{SC}} = [\mathbf{I} + \mathbf{E} : \tilde{\mathbf{C}}^{-1} : (\mathbf{C}_1 - \tilde{\mathbf{C}})]^{-1} \tag{3.4}$$

Substituting Equation (3.4) into Equation (3.1) leads to an implicit equation since the effective stiffness tensor of the composite appears on both sides of the equation. This nonlinear equation is usually solved numerically.

3.2.2 Analytical homogenization models for textile composites

Gommers *et al.* (1998a) developed a methodology based on the Mori-Tanaka method to evaluate the mechanical properties of textile composites, like that shown in Figure 3.1. The approach consists of approximating the yarns geometry by a series of "divided" inclusions, as shown in Figure 3.2, and then use inclusion-based homogenization models for computing the composite's effective properties.

The first step consists of defining inclusions that match the yarns geometry. In a real

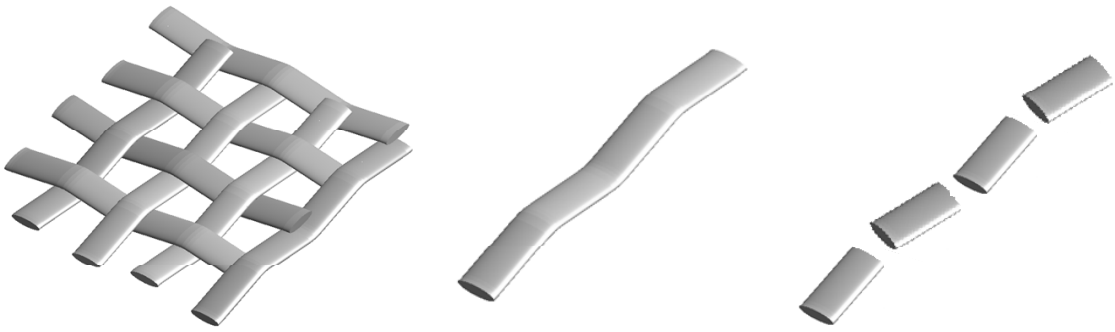

(a) (b) (c)

Figure 3.2 Geometrical simplification of a yarn. a) Woven fabric; b) A single yarn; c) A single yarn divided into a series of inclusions whose orientations follow the yarns waviness.

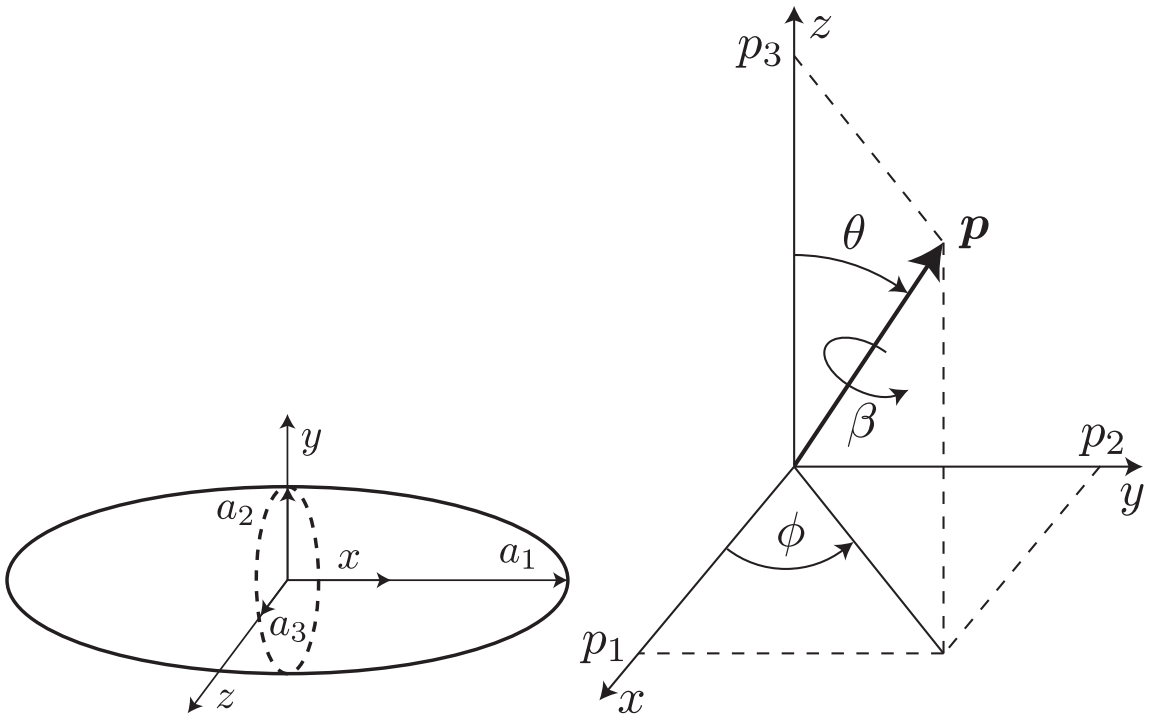

(a) (b)

Figure 3.3 Geometry and orientation of an inclusion. (a) Each inclusion is described by three characteristic dimensions, a_1, a_2 and a_3. (b) Euler angles ϕ and θ describe the angular position of a vector $\boldsymbol{p}$ in space. .

textile composite, the yarns usually have a lenticular cross-section. In this work, the yarns cross sections were assumed to be elliptical. An ellipsoidal inclusion is defined by three

characteristic dimensions a_1, a_2 and a_3, as shown in Figure 3.3. For a prolate spheroid, a_1 defines its characteristic length while a_2 and a_3 define its cross-section. Ratios $\frac{a_1}{a_2}$, $\frac{a_2}{a_3}$ and $\frac{a_1}{a_3}$ are used to compute Eshelby's tensor $\mathbf{E}$ (Mura, 1982). On one hand, the choice of a_2 and a_3 is straightforward since they represent the yarn's cross-section. On the other hand, the choice of a_1 is somewhat arbitrary. In their work, Gommers *et al.* (1998a) set a_1 as infinity for simulating yarns' continuity. While this assumption makes sense for long and relatively straight yarns, it loses its validity as waviness increases for high volume fractions. In order to correct this shortcoming, Huysman *et al.* (1998) proposed taking into account the yarn curvature by decreasing the aspect ratio with the following equation:

$$a_1 = \lambda \frac{k}{a_2} \tag{3.5}$$

where k is the yarn's local curvature radius and λ is a calibration factor. In their paper, Huysman *et al.* (1998) set $\lambda = \pi$. The stiffness equation is evaluated in this methodology by replacing every yarn by a discrete set of inclusions, for which a_1 is evaluated using their local curvature . The specific yarns arrangement is then described by a discrete set of orientations. Each inclusion is oriented according to specific values of $\{\phi, \theta\}$, as shown in Figure3.3b. The third angle β is not required since there is almost no rotation of the yarns around their principal axis. For example, if the yarns are divided into 20 ellipsoidal inclusions, the homogenization equation will be performed over 20 different inclusions, each with its own set of angles $\{\phi, \theta\}$ and aspect ratio $\{a_1, a_2, a_3\}$.The homogenized response is then evaluated with the following equations:

$$\mathbf{D} = (\mathbf{C}_1 - \mathbf{C}_0) : \mathbf{A} \tag{3.6a}$$

$$\tilde{C}_{ijkl} = C_{0_{ijkl}} + \sum_{z=1}^{N} \frac{\rho_1}{n} \alpha_{im}(\theta_z, \phi_z) \alpha_{jn}(\theta_z, \phi_z) \alpha_{ko}(\theta_z, \phi_z) \alpha_{lp}(\theta_z, \phi_z) D_{mnop} \tag{3.6b}$$

Equations (3.6) are therefore discrete representations of Equations (3.1) and (3.2) (See section 3.1 for more details).

3.2.3 Finite Element simulations

Textile composites effective properties can be accurately predicted with FE simulations. The approach consists of first meshing a representative pattern. Then, boundary conditions are applied to the model and the resulting stresses and strains are computed. The effective properties are computed using the volume averaged stress and strain fields. Authors like Verpoest and Lomov (2005a); Lomov *et al.* (2005) have successfully used this technique, and

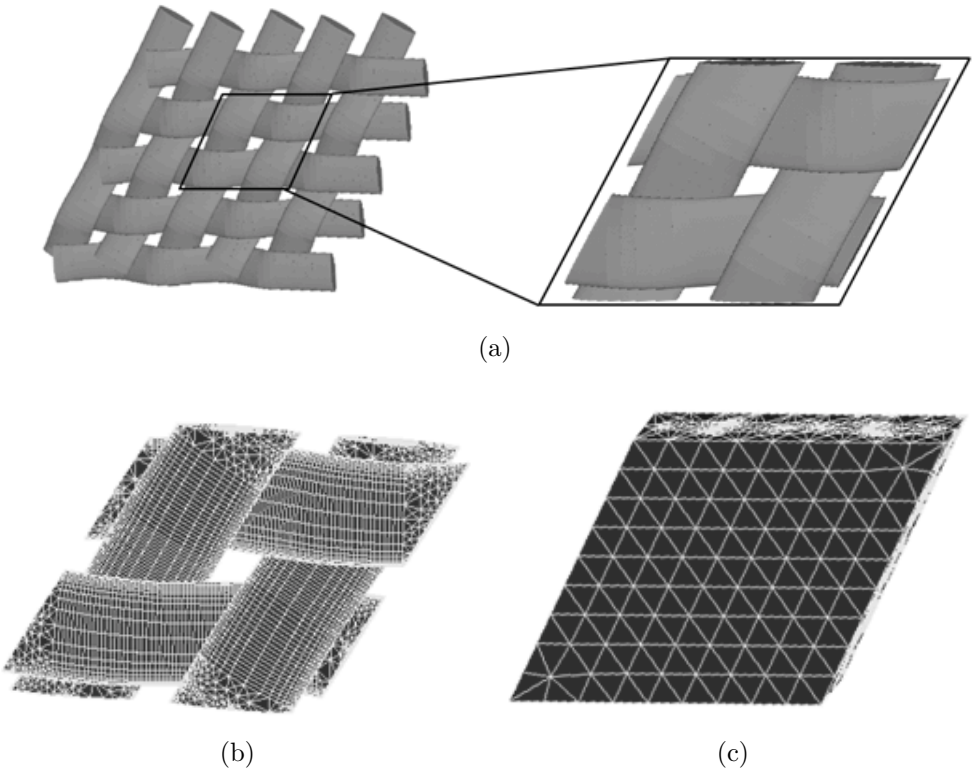

(a)

(b)

(c)

Figure 3.4 Necessary steps for the creation of the RVE in the software ANSYS. a) A solid model of the textile architecture is modeled in the software Wisetex and a periodic unit cell is selected b) The periodic yarns are meshed. c) The matrix is modeled and meshed.

the procedure was detailed in the reviews of Lomov *et al.* (2007); Wong *et al.* (2006).

Wisetex software (Verpoest and Lomov, 2005a) provides efficient tools to create solid or meshed representations of 2.5 D and 3D textiles. The software FETex can be used to transfer the geometrical information of the yarns obtained from WiseTex and their meshing specifications to ANSYS. In order to reduce the calculation time, only a periodic pattern of the textile is represented. Figure 3.4 illustrates the meshing procedure. Periodic boundary conditions are applied and the problem is solved. In order to apply this type of boundary conditions, meshes on opposite faces must be identical. The periodic boundary conditions can be applied with Multiple Point Constraints (MPC) according to the relations derived by Lomov *et al.* (2007).

3.2.4 Viscoelastic homogenization

The stress response to an applied strain history on a linearly viscoelastic material is given by:

$$\boldsymbol{\sigma}(t) = \int_0^t \mathbf{C}(t-\tau) : \frac{\mathrm{d}\boldsymbol{\varepsilon}}{\mathrm{d}\tau}\mathrm{d}\tau \tag{3.7}$$

where $\mathbf{C}(t)$ is the relaxation modulus, expressed as:

$$\mathbf{C}(t) = \mathbf{C}^0 + \sum_{s=1}^{N} \mathbf{C}^s \exp(-t\tau_s) \tag{3.8}$$

where $\mathbf{C}^0$ and $\mathbf{C}^s$ are positive semi-definite and $\tau_s > 0$ are the inverted relaxation times. The Laplace-Carson transform is defined as:

$$c^*(v) = v \int_0^\infty c(t) \exp(-vt)\mathrm{d}t \tag{3.9}$$

where v is the variable in Laplace-Carson space. When the Laplace-Carson transform is applied to Equation (3.7), the relationship between strain and stress tensors becomes :

$$\boldsymbol{\sigma}^*(v) = \mathbf{C}^*(v) : \boldsymbol{\varepsilon}^*(v) \tag{3.10}$$

The so-called viscoelastic correspondence principle enables computing effective properties in the Laplace-Carson space with analytical homogenization models. The methodology consists of replacing the elastic properties appearing in Equations (3.1,3.3,3.4) by their Laplace-Carson transform expressions, such that:

$$\tilde{\mathbf{C}}^* = \mathbf{C}_0^* + \rho_1(< \mathbf{C}_1^* : \mathbf{A}^* > - \mathbf{C}_0^* :< \mathbf{A}^* >) \tag{3.11}$$

For very specific cases, inversion to the time domain can be obtained analytically. Most of the time, numerical inversions of the Laplace-Carson transform must be performed to obtain the effective properties in the time domain. The recent works of Lévesque *et al.* (2007) assume that one component of $\tilde{\mathbf{C}}(t)$, labelled as $\hat{g}(t)$, is given by:

$$\hat{g}(t) = g_0 + \sum_{m=1}^{M} g_m \exp(-t\tau_m) \tag{3.12}$$

where the τ_m are chosen a priori, the g_m are unknown and g_0 is obtained from the limit value theorem. Then, if $\tilde{g}^*(v)$ is one component of $\tilde{\mathbf{C}}^*$ computed from an analytical homogenization

Table 3.1 Matrix properties used for homogenization techniques validation.

$E_m(t)$(GPa)	ν
$3 + 2\exp(-2t)$	0.3

model, the inversion algorithm consists of solving the following minimization problem:

$$\inf_{g_m} \sum_{s=1}^{S} \left[\tilde{g}^*(v_s) - \hat{g}^*(v_s)\right]^2 \tag{3.13}$$

where the v_s are computed so that $\tilde{g}^*(v_{s+1}) - \tilde{g}^*(v_s)$ is a constant value.

3.3 Methodology

The general methodology consists of comparing the predicted mechanical response from analytical and numerical homogenization models for a broad range of textile composites. The following subsections detail the implementation of the analytical and numerical models, as well as the methodology for interpreting the results.

Woven and braided textile architectures were studied, for five different yarn volume fractions, ranging from 10 % to 45%. The yarns were placed at a $\pm 30°$ for the biaxiallly braided composite with a 1x1 diamond pattern while a plain weave design was chosen for the woven fabric. The same elliptical yarn cross-section was chosen for both textiles. The matrix was an artificial material assumed to be isotropic, linearly viscoelastic and with a constant Poisson's ratio. Relaxation modulus and Poisson's ratio are given in Table 1. Isotropic and transversely isotropic yarns, whose properties are listed in Table 2 and 3, were simulated. The results were analyzed as a function of the constituents mechanical properties contrast R, defined as:

$$R = \frac{E_{11}}{E_m(0)} \tag{3.14}$$

where E_{11} is the yarns axial Young's modulus and $E_m(t)$ is the matrix relaxation modulus. Stiffness contrasts ranging from 5 to 80 were simulated. In total, 2 architectures, 5 volume fractions and 10 yarns properties, for a total of 100 models, were simulated by FE.

3.3.1 Analytical models

For each volume fraction and architecture, WiseTex was used to obtain the orientation as well as the curvature of each yarn segment. Laplace-Carson transform was applied to $\mathbf{C}_0(t)$ and $\tilde{\mathbf{C}}^*(v)$ was computed with the correspondence principle according to Equation (3.2).

Table 3.2 Isotropic yarn properties for different stiffness contrasts (R).

Stiffness contrast (R)	E_{11}(GPa)	ν
5	25	0.3
10	50	0.3
20	100	0.3
40	200	0.3
80	400	0.3

Table 3.3 Transversely isotropic yarn properties for different stiffness contrasts (R).

Stiffness contrast (R)	E_{11}(GPa)	E_{22} (GPa)	$G_{12}(GPa)$	ν_{12}	ν_{23}
5	25	5	5	0.3	0.27
10	50	10	10	0.3	0.27
20	100	20	20	0.3	0.27
40	200	40	40	0.3	0.27
80	400	80	80	0.3	0.27

$\mathbf{A}$ was evaluated according to the Mori-Tanaka ($\mathbf{A}_{\mathrm{MT}}$) or Self-Consistent ($\mathbf{A}_{\mathrm{SC}}$) schemes. For the computations, ratio $\frac{a_3}{a_2}$ was set to 0.29 and kept constant for all textile architectures modeled. For the Self-Consistent scheme, $\frac{a_1}{a_2}$ was set to 1000 to simulate continuous yarns. For the Mori-Tanaka model, two different configurations were studied. In the first configuration, $\frac{a_1}{a_2}$ was also set to 1000 to simulate infinitely long yarns. In the second configuration, the aspect ratio $\frac{a_1}{a_2}$ was adjusted using Huysman's methodology, presented in Equation (3.5), in order to account for the influence of the yarns curvature. Both configurations are presented in the results section. Eshelby's tensor was computed for ellipsoid yarns oriented along x (see Figure 3.3a) with the numerical scheme of Gavazzi and Lagoudas (1990). Strain localization tensors $\mathbf{A}_{\mathrm{MT}}$ and $\mathbf{A}_{\mathrm{SC}}$ were computed according to Equations (3.3) and (3.4).

Inversion to the time domain was performed according to the procedure of Lévesque *et al.* (2007). In this paper, only the components $\tilde{C}_{11}(t)$, $\tilde{C}_{22}(t)$, $\tilde{C}_{33}(t)$ and $\tilde{C}_{66}(t)$ were studied. Let $\tilde{g}(t)$ be one of these components and $\hat{g}(t)$, as defined in Equation (3.12), be an approximation of $\tilde{g}(t)$. g_0 of Equation (3.12) was obtained as:

$$g_0 = \lim_{v \to 0} \tilde{g}^*(v) \tag{3.15}$$

Now, define ζ as:

$$\zeta = \lim_{v \to \infty} \tilde{g}^*(v) - g_0 \tag{3.16}$$

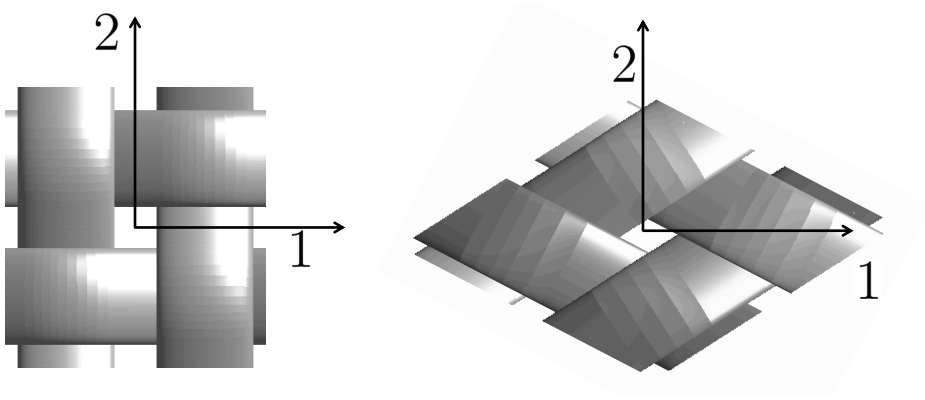

(a) (b)

Figure 3.5 Coordinate systems for which the results are presented for the (a) woven architectures and (b) braided architectures.

then the v_s of Equation (15) were obtained by solving:

$$\tilde{g}^*(v_s) = g_0 + s\frac{0.98\zeta}{S} \quad \text{for } s = \{1, 2, \ldots, S\} \tag{3.17}$$

In this work, S was set to 60. Finally, $\hat{g}(t)$ was obtained by solving optimization problem (3.13).

3.3.2 Numerical models

The textile yarns were generated with Wisetex and transferred to ANSYS with FETex. The prismatic matrix box for the woven architecture was generated automatically by FETex while that of the braided architecture required manual input. The yarns were meshed with 20-node brick elements (SOLID 95) and the matrix box was meshed with 10-node tetrahedron elements (SOLID 187) suitable for viscoelastic analysis in ANSYS. Figure 3.4 illustrates the main steps for simulating the braided composites. The fabrics lied in the 1-2 plane. Axis 1 was placed such that braids were at 30° in the 1-2 plane. Figure 3.5 illustrates these axes.

No assumptions were made regarding the effective properties material symmetries. The periodic boundary conditions were programmed with the help of ANSYS Parametric Design Language (APDL), for both architectures. Six independent periodic unitary displacements, presented in Table 3.4, were consecutively applied to simulate relaxation tests. Finite element solution of this problem provided stresses $\boldsymbol{\sigma}(\boldsymbol{x}, t)$ in all elements and for a discrete number to times, typically 10. The effective stress tensor $\boldsymbol{\Sigma}(t)$ was obtained according to:

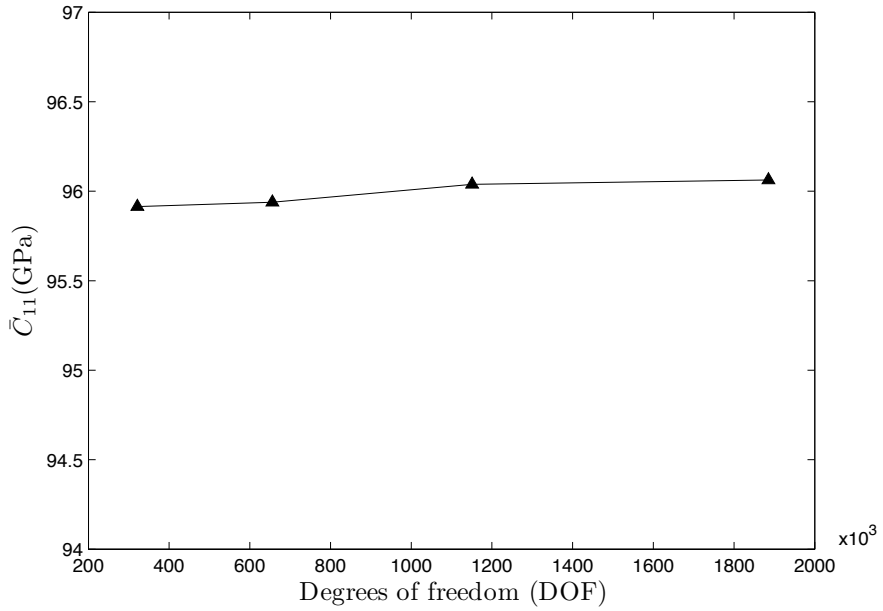

Figure 3.6 Effect of the mesh size on the component $\bar{C}_{11}$ for $t = 0$, for a braided composite with a yarns volume fraction of 45 %, and a stiffness contrast of 80.

$$\boldsymbol{\Sigma}(t) = \frac{1}{V}\sum_{n=1}^{N} \boldsymbol{\sigma}_n(t) V_n \tag{3.18}$$

where V is the volume of the RVE, N is the total number of elements, $\boldsymbol{\sigma}_n(t)$ and V_n are respectively the stress at the center of an element n and the volume of this element. The effective strain tensor was deduced from the applied displacement and the effective relaxation modulus $\bar{\mathbf{C}}(t)$ was computed. Convergence of the FE meshes was evaluated by studying the evolution of $\bar{C}_{11}(0)$ as a function of the number of Degrees of Freedom (DOF). The convergence was verified for each yarns volume fraction, for both textile architectures and for $R = 80$. It was assumed that, if convergence was reached for $R = 80$, it was also reached for any lower values. Therefore, the mesh density at $R = 80$ was used for all lower values of R (for the same volume fraction and fabric type). Figure 3.6 shows for example the evolution of $\bar{C}_{11}(0)$ as a function of the number of DOF for a braided fabric for a yarns volume fraction of 45 % and for a stiffness contrast of 80. The figure shows that $\bar{C}_{11}(0)$ varies from 95.9 to 96.03 when the number of DOF varies from 3.21×10^5 to 1.88×10^6. Therefore, simulations were performed with 3.2×10^5 DOF for this specific case.

Table 3.4 Unitary displacements applied to obtain the stiffness tensor and the corresponding components of the relaxation tensor obtained. $H(t)$ represents the Heaviside function.

Unitary displacement	Applied strain	Components of the relaxation tensor
1	$[0.01; 0; 0; 0; 0; 0]^T \times H(t)$	$\bar{C}_{11}; \bar{C}_{21}; \bar{C}_{31}; \bar{C}_{41}; \bar{C}_{51}; \bar{C}_{61}$
2	$[0; 0.01; 0; 0; 0; 0]^T \times H(t)$	$\bar{C}_{12}; \bar{C}_{22}; \bar{C}_{32}; \bar{C}_{42}; \bar{C}_{52}; \bar{C}_{62}$
3	$[0; 0; 0.01; 0; 0; 0]^T \times H(t)$	$\bar{C}_{13}; \bar{C}_{23}; \bar{C}_{33}; \bar{C}_{43}; \bar{C}_{53}; \bar{C}_{63}$
4	$[0; 0; 0; 0.02; 0; 0]^T \times H(t)$	$\bar{C}_{14}; \bar{C}_{24}; \bar{C}_{34}; \bar{C}_{44}; \bar{C}_{54}; \bar{C}_{64}$
5	$[0; 0; 0; 0; 0.02; 0]^T \times H(t)$	$\bar{C}_{15}; \bar{C}_{25}; \bar{C}_{35}; \bar{C}_{45}; \bar{C}_{55}; \bar{C}_{65}$
6	$[0; 0; 0; 0; 0; 0.02]^T \times H(t)$	$\bar{C}_{16}; \bar{C}_{26}; \bar{C}_{36}; \bar{C}_{46}; \bar{C}_{56}; \bar{C}_{66}$

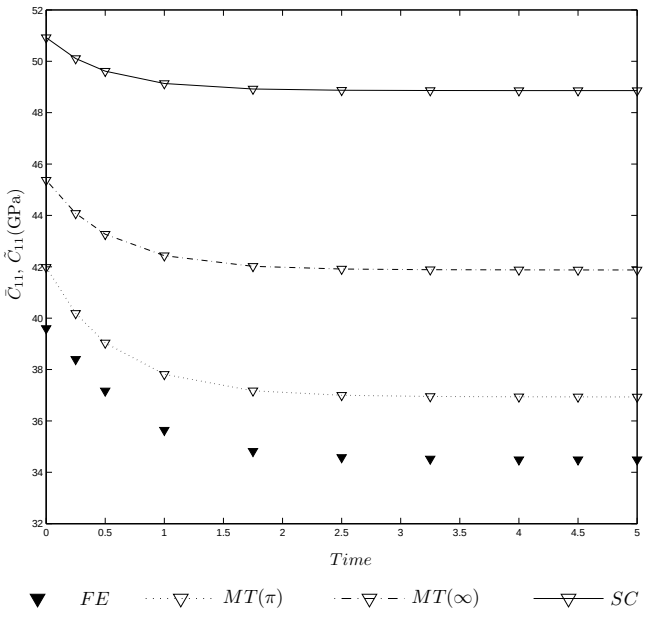

Figure 3.7 $\check{C}_{11}(t)$ for a yarn volume fraction ($V_f(\%) = 40\%$), and stiffness contrast $R = 40$. The results are presented for a woven fabric with transversely isotropic yarns.

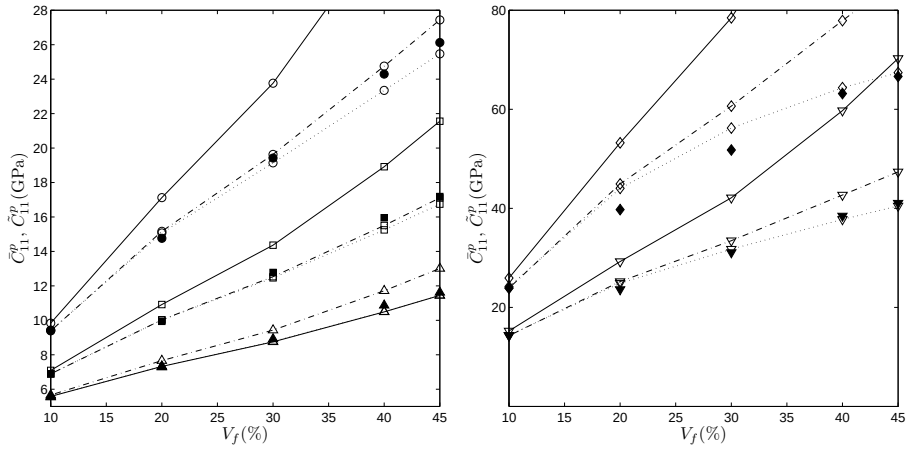

(a)

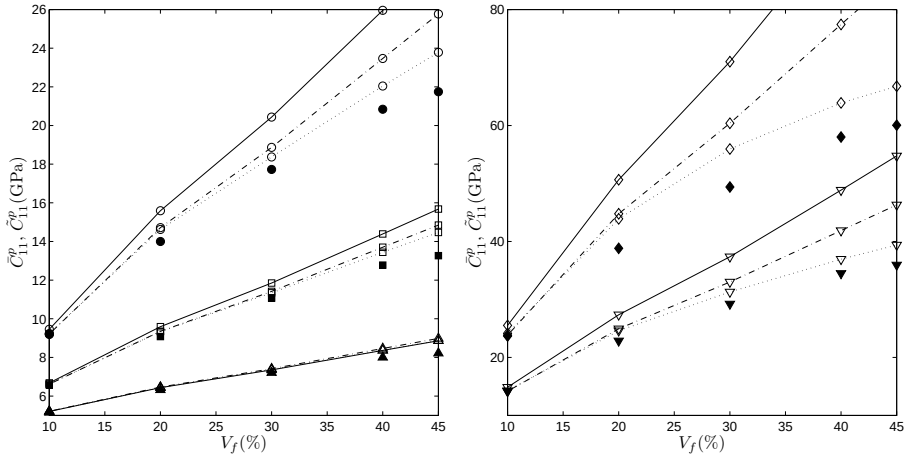

(b)

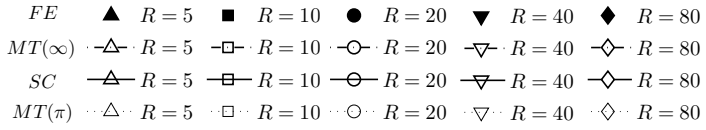

Figure 3.8 $\check{C}^p_{11}$ for woven architectures, for different yarns volume fractions ($V_f(\%)$), and stiffness contrasts R. The results are presented for FE simulations, Mori-Tanaka (MT) method and the Self-Consistent scheme (SC) for (a) isotropic yarns and (b) transversely isotropic yarns.

3.3.3 Data reduction procedure

Three elements of comparison were selected to analyze the performance of the analytical models studied: i) the steady-state modulus; ii) the transient part; iii) the relaxation rate. The steady-state modulus $\check{\mathbf{C}}^p$, for either $\tilde{\mathbf{C}}^p$ or $\bar{\mathbf{C}}^p$, is defined as:

$$\check{\mathbf{C}}^p = \lim_{t\to\infty} \check{\mathbf{C}}(t) \tag{3.19}$$

Since it is impossible to reach infinity in practical calculations, this state was considered to be reached when:

$$\frac{\check{\mathbf{C}}(t_{k+1}) - \check{\mathbf{C}}(t_k)}{t_{k+1} - t_k} < 0.001 \tag{3.20}$$

were k refers to the time step. Equation (3.20) is in fact an estimation of the relaxation rate at a given time t_k. For each simulated cases and for each component of the effective properties, the relaxation rate was computed at $t = 0$. Values ranging from 0.49 to 9.47 GPa/(time unit) were obtained. Therefore, Equation (3.20) implies that $\check{\mathbf{C}}^p$ is obtained when the relaxation rate is at least 500 times slower than that at $t = 0$. Five time units were usually sufficient to reach that threshold for the composites studied. The transient part $\check{\mathbf{C}}^t$ is defined as:

$$\check{\mathbf{C}}^t = \check{\mathbf{C}}(0) - \check{\mathbf{C}}^p \tag{3.21}$$

and relates to the amount of relaxed stresses. The rate of relaxation was assessed by extracting the times at which the transient part lost 50% and 90% of its values, which reduces to solving for t_ω:

$$\check{\mathbf{C}}(t_\omega) = \omega\check{\mathbf{C}}^t \quad \text{where } \omega = \{10\%, 50\%\} \tag{3.22}$$

3.4 Results

3.4.1 In-plane properties

The FE and analytical predictions provided in the sequel are expressed in the coordinates systems illustrated in Figure 3.5 for the woven and braided fabrics. For in-plane properties, the Mori-Tanaka method and Self-Consistent scheme were first compared to Finite Elements simulations for $\tilde{C}_{11}(t)$ and $\tilde{C}_{66}(t)$. In this section, the Mori-Tanaka model with $\frac{a_1}{a_2} = 1000$ is referred to as $MT(\infty)$ while the formulation taking into account the curvature of the yarns is referred to as $MT(\pi)$. Figure 3.7 shows the viscoelastic behavior of component $\check{C}_{11}$ for a yarn volume fraction of 40%, and stiffness contrast $R = 40$, for a woven fabric with transversely isotropic yarns. The results presented show that the Mori-Tanaka method is better than the Self-Consistent scheme at predicting the viscoelastic behavior of textile composites. $MT(\pi)$

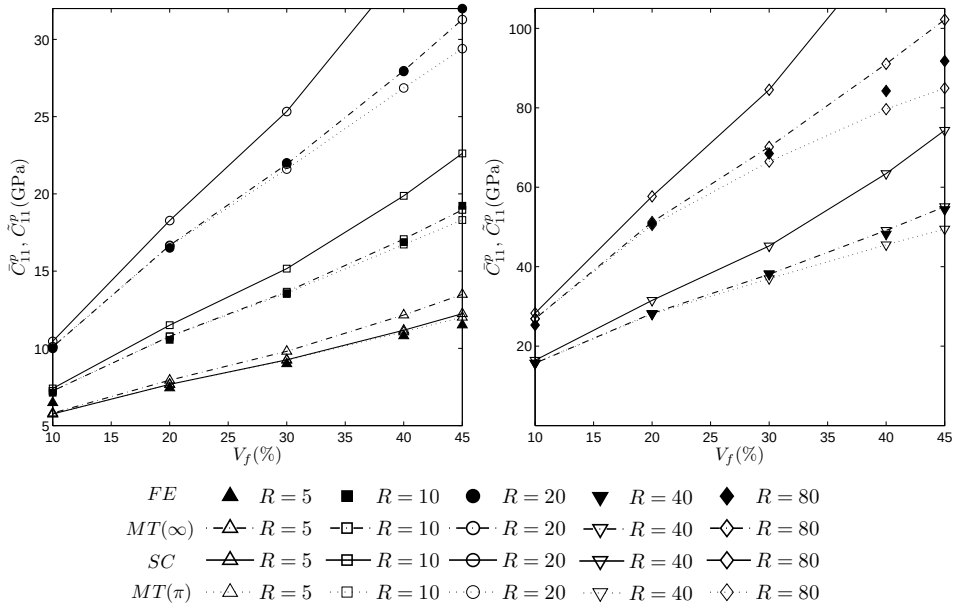

Figure 3.9 $\check{C}_{11}$ for braided architectures, for different yarns volume fractions ($V_f(\%)$), and stiffness contrasts R for isotropic yarns.

is better than $MT(\infty)$ at evaluating viscoelastic behavior. Similar plots were obtained for all the other cases studied and are not shown here.

Steady-state part

The predictions of $\check{C}^p_{11}$ for a woven composite with isotropic yarns are presented in Figures 3.8a and 3.8b, respectively, for several volume fractions and stiffness contrasts. For this type of fabric, $\check{C}_{11} = \check{C}_{22}$. Figure 3.8 shows that analytical models tend to overestimate the stiffness of the composite when compared to Finite Element simulations, for almost all the stiffness contrasts and yarns volume fractions studied. The Mori-Tanaka method is more accurate than the Self-Consistent scheme for this range of contrasts and volume fractions. Also, the difference between FE models and $MT(\infty)$ method increases with increasing yarns volume fraction and stiffness contrasts. For isotropic fibers, the difference varied from 0.72 % for $V_f = 10\%$ and $R = 5$ to 29.77 % for $V_f = 45\%$ and $R = 80$. Using an adjusted aspect ratio increased the accuracy significantly. For isotropic fibers, the discrepency varied from 0.81 % for $V_f = 10\%$ and $R = 5$ to 3 % for $V_f = 45\%$ and $R = 80$. Figure 3.9 shows the same results but for the braided architecture. Trends similar to those of woven fabrics are observed. In this case, the Mori-Tanaka method with $\frac{a_1}{a_2} = 1000$ ($MT(\infty)$) predictions are close to FE simulations. For C^p_{11}, $MT(\pi)$ yielded the most accurate results when compared to FE simulations. Similar results were obtained for transversely isotropic yarns.

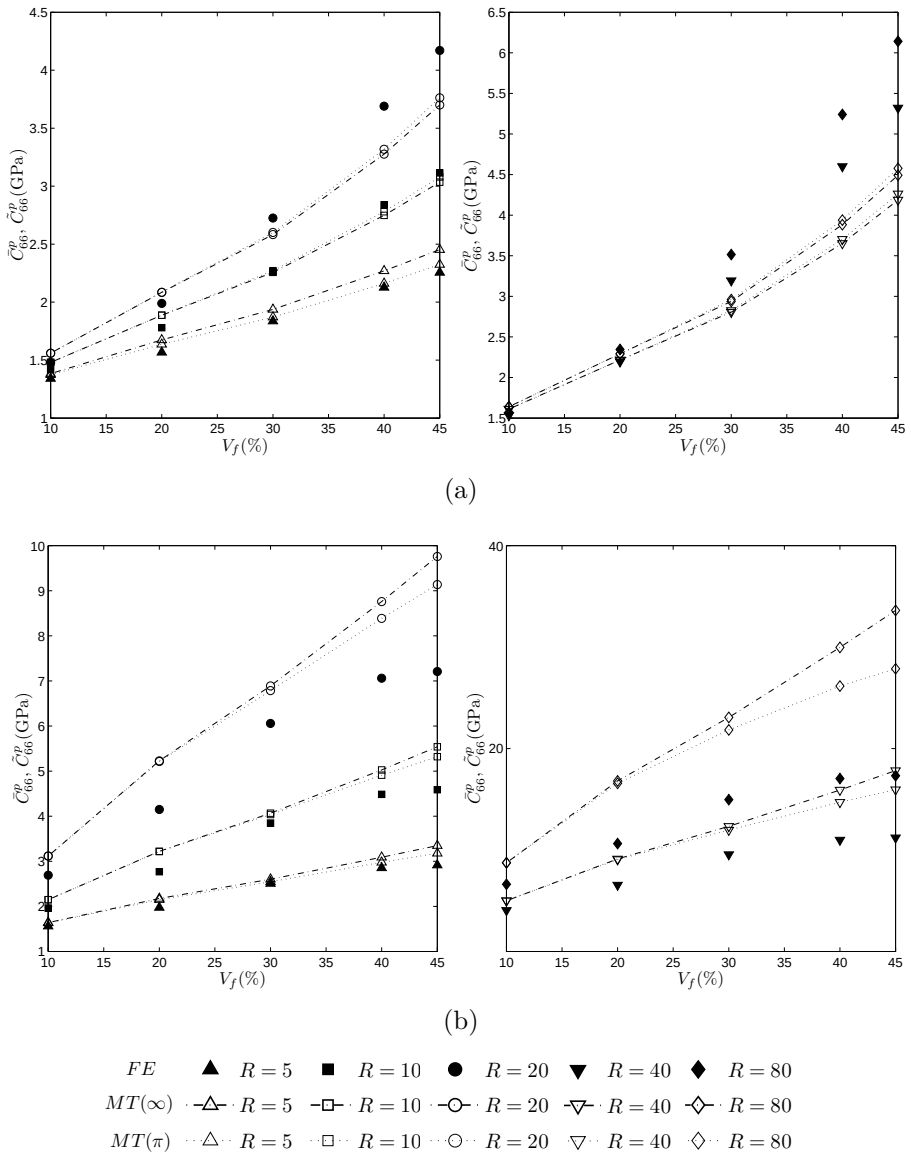

Figure 3.10 $\check{C}^p_{66}$ for different yarns volume fractions ($V_f(\%)$), and stiffness contrasts R. The results are presented for (a) woven and (b) braided fabrics with transversely isotropic yarns. Only the predictions of the Mori-Tanaka models are shown since those of the Self-Consitent model yielded poor accuracy.

Figure 3.10 shows $\check{C}^p_{66}$ for woven and braided fabrics with transversly isotropic yarns. Only the predictions of the Mori-Tanaka models are shown since those of the Self-Consitent model yielded poor accuracy. The analytical prediction for the shear relaxation modulus for the woven composite, presented in Figure 3.10a are much closer to FE simulations than the predictions for the braided composite, presented in Figure 3.10b. In the woven composite, the yarns are disposed in the 0° and 90° directions, which means that they have a minimal influence on the shear modulus. In contrast, the yarns are disposed at ± 30° for the braided composite, closer to the 45° angle for which the influence of the yarns on in-plane shear properties would be maximal. The Mori-Tanaka method predicts the results of the shear relaxation modulus with better accuracy for the woven composite than for the braided composite. $MT(\pi)$ yielded more accurate results than $MT(\infty)$. The observations presented are similar for the isotropic case. The results for the other in-plane components (not shown here) yielded similar observations.

Transient part

The analysis of the transient part confirms some of the observations made for the steady-state part. For all components studied, $MT(\pi)$ shows a clear superiority over other micromechanical models, when compared to FE simulations. Figure 3.11 shows $\check{C}^t_{11}$ predictions for transversely isotropic yarns for both woven and braided architectures. It can be seen that Mori-Tanaka delivers much more accurate predictions than those of the Self-Consistent scheme. For stiffness contrasts up to 20, the results of Mori-Tanaka method match FE simulations. One can also notice that Mori-Tanaka method and FE simulations predict an increase of the transient part, whereas the Self-Consistent scheme predicts a decrease. For $R \geq 40$ and $V_f \geq 40\%$, $MT(\infty)$ fails to capture the significant increase of the transient part, while $MT(\pi)$ yields closer results to FE simulations. Figure 11 shows $\check{C}^t_{66}$ for woven and braided fabrics. As for $\check{C}^p_{66}$, the predictions for the woven fabrics are much more accurate than those of the braided fabrics. Again, $(MT(\pi))$ offers the most accurate predictions.

Decay time

For the matrix alone, the decay times are $t_{50\%} = 0.346$ and $t_{90\%} = 1.151$. Table 3.5 presents the decay times for the braided architectures for $\check{C}_{11}(t)$ with transversely isotropic yarns and a volume fraction of 40%. The decay times predicted by analytical methods with an infinite aspect ratio are much closer to the decay times of the matrix alone than those predicted by FE simulations. Independently of the stiffness contrasts, these models fail to predict accurately the transient part rate of decay. However, $MT(\pi)$ yields closer results

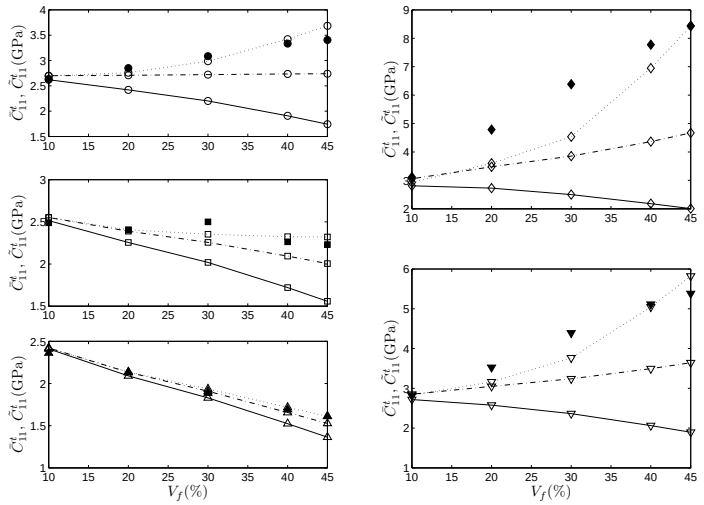

(a)

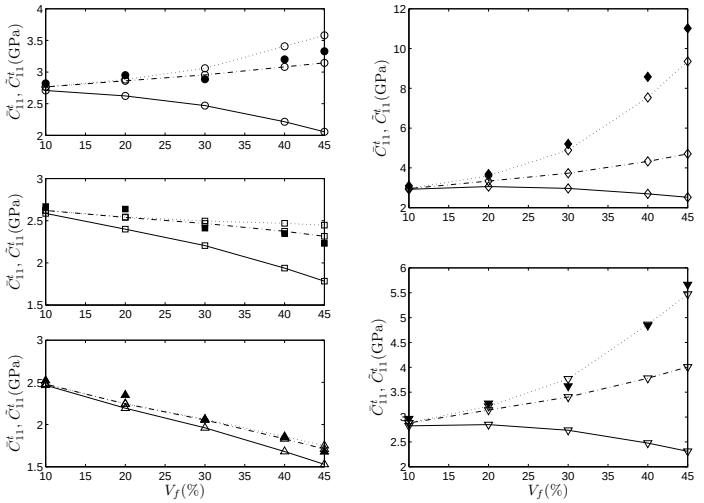

(b)

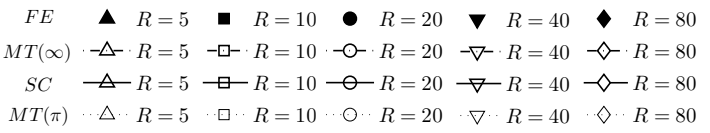

Figure 3.11 $\check{C}^t_{11}$ for different yarns volume fractions ($V_f(\%)$), and stiffness contrasts R. The results are presented for (a) woven and (b) braided fabrics with transversely isotropic yarns.

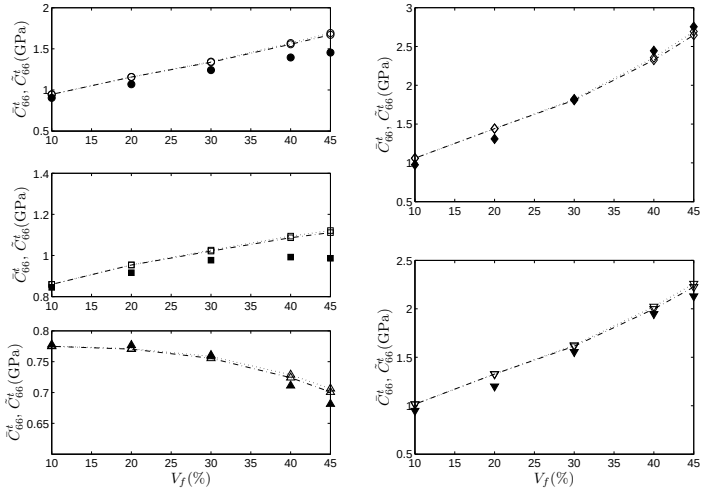

(a)

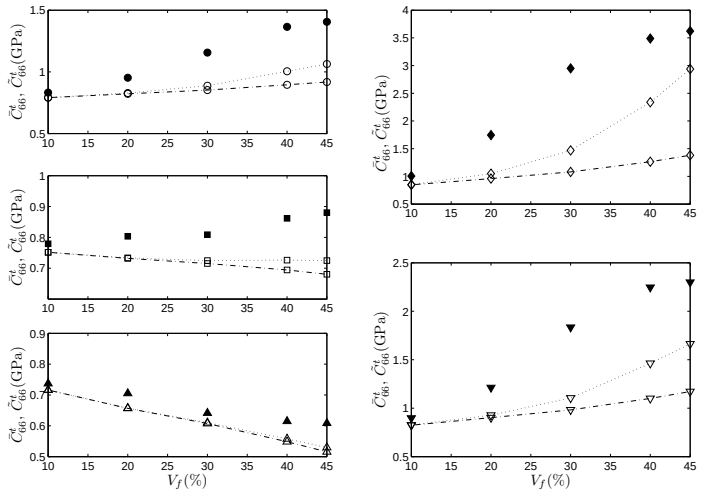

(b)

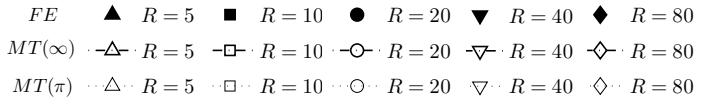

Figure 3.12 $\check{C}^t_{66}$ for different yarns volume fractions ($V_f(\%)$), and stiffness contrasts R. The results are presented for (a) woven and (b) braided fabrics with transversely isotropic yarns. The Self-Consitent model yielded poor accuracy and its results are not presented.

Table 3.5 Comparison of decay times (in time units) for a braided composite with $V_f = 40\%$ for different stiffness contrasts and transversely isotropic yarns.

	FE		$MT(\infty)$		$MT(\pi)$		Self-Consistent	
Contrast R	$t_{50\%}$	$t_{90\%}$	$t_{50\%}$	$t_{90\%}$	$t_{50\%}$	$t_{90\%}$	$t_{50\%}$	$t_{90\%}$
5	0.498	1.50	0.392	1.39	0.392	1.40	0.367	1.28
10	0.504	1.53	0.391	1.39	0.401	1.42	0.366	1.27
20	0.512	1.56	0.392	1.38	0.404	1.43	0.365	1.27
40	0.527	1.61	0.383	1.34	0.411	1.46	0.363	1.26
80	0.547	1.67	0.375	1.31	0.426	1.51	0.361	1.25

Table 3.6 Comparison of decay times for a braided composite with $R = 40$ for different yarns volume fraction and transversely isotropic yarns.

	FE		$MT(\infty)$		$MT(\pi)$		Self-Consistent	
$V_f(\%)$	$t_{50\%}$	$t_{90\%}$	$t_{50\%}$	$t_{90\%}$	$t_{50\%}$	$t_{90\%}$	$t_{50\%}$	$t_{90\%}$
10	0.482	1.43	0.365	1.27	0.366	1.28	0.358	1.23
20	0.487	1.46	0.370	1.29	0.375	1.31	0.361	1.25
30	0.499	1.51	0.376	1.31	0.390	1.38	0.361	1.26
40	0.527	1.61	0.383	1.33	0.411	1.46	0.363	1.26
45	0.540	1.65	0.387	1.36	0.54	1.65	0.363	1.26

to the FE simulations. Table 3.6 presents the results for the same architecture but with a stiffness contrast $R = 40$ and increasing yarns volume fraction. Again, $MT(\pi)$ provides the most accurate results. These results were observed for all the components of the relaxation tensor.

3.4.2 Out-of-plane properties

The comparison between analytical predictions and numerical simulations can also be performed for the out-of-plane properties. The results for the woven and braided architectures are presented for transversely isotropic yarns in Figure 3.13 for $\check{C}^p_{33}$. For both architectures, Mori-Tanaka predictions are in good agreement with FE simulations, with a maximum discrepency of 20 % for the woven architecture at $V_f = 40\%$ and $R = 80$, and of 14.4 % for the braided architecture at $V_f = 45\%$ and $R = 80$. For the out-of-plane properties, Mori-Tanaka method underestimates the behavior of the composite. In this case, the properties are matrix-dominated since no yarn is directly present in this direction. Also, $MT(\infty)$ and $MT(\pi)$ yield almost identical results for this component of the relaxation tensor. Consequently, the influence of the aspect ratio is less important on the out-of-plane properties. The results are confirmed for the transient part, presented in Figure 3.14, where

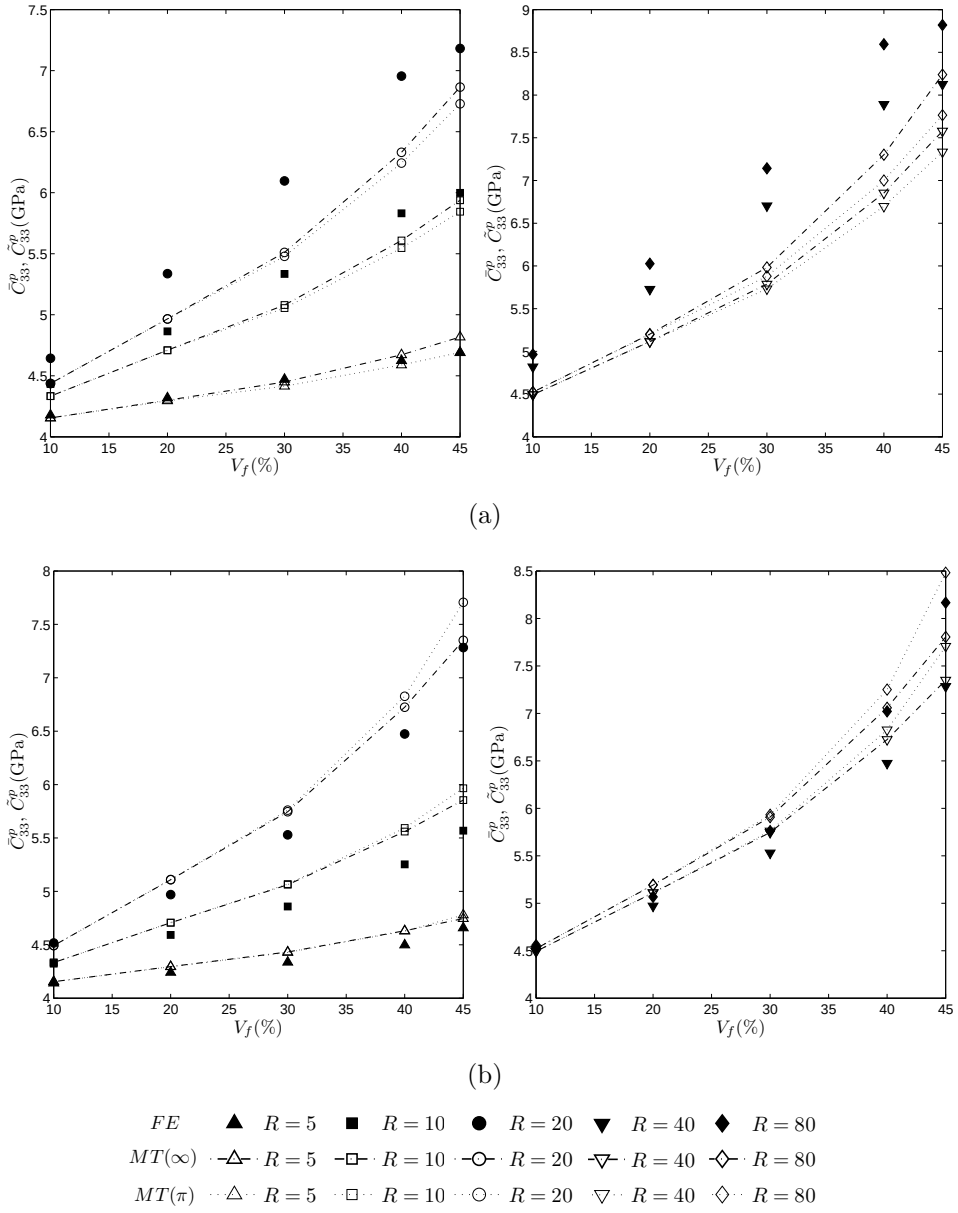

Figure 3.13 $\check{C}^p_{33}$ for different yarns volume fractions ($V_f(\%)$), stiffness contrasts R. The results are presented for (a) woven and (b) braided fabrics with transversely isotropic yarns. The Self-Consitent model yielded poor accuracy and its results are not presented.

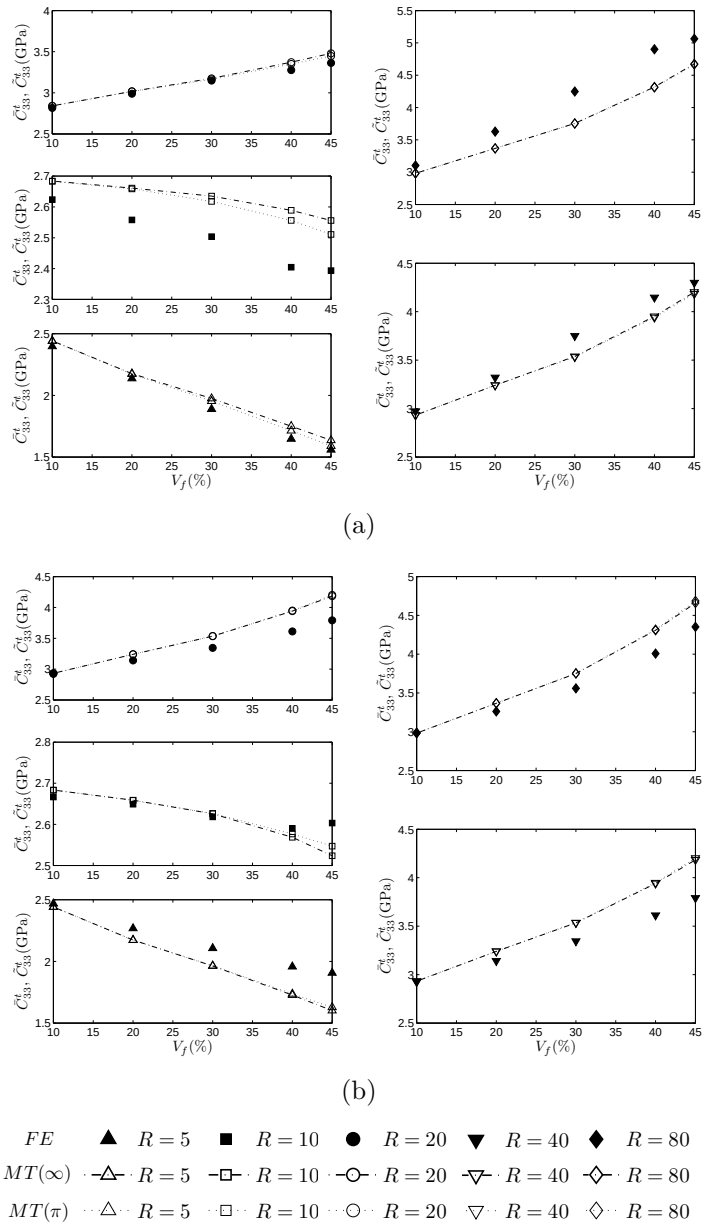

Figure 3.14 $\check{C}^t_{33}$ for different yarns volume fractions ($V_f(\%)$), stiffness contrasts R. The results are presented for (a) woven and (b) braided fabrics with transversely isotropic yarns. The predictions of the Self-Consistent scheme were removed because they were inaccurate.

the Mori-Tanaka method predicts accurately FE simulations. The Self-Consistent scheme results were not displayed because there was a high discrepancy with FE simulations.

3.5 Conclusion

The contributions of this study are:

1. An analytical framework for predicting the linearly viscoelastic behavior of textile composites.

2. A numerical model for predicting the linearly viscoelasitic behavior of the same composites.

3. An evaluation of the analytical framework accuracy.

An important finding of this study is that the analytical framework, combined with the Mori-Tanaka model, leads to relatively accurate predictions for both the permanent and transient parts for matrix dominated properties. For fiber dominated properties, the analytical models with an infinite aspect ratio overestimate the steady-state part while they underestimate the transient part. The authors believe that this is due to the very high aspect ratio assumed for the inclusions in order to account for yarns continuity. To the contrary, $MT(\pi)$ yields good approximations of the FE simulations. This phenomenon is amplified due to the increased waviness of the yarns as fiber volume fraction increases, but also by the increasing stiffness contrast. Therefore, the authors believe that the Mori-Tanaka model with an adjusted aspect ratio to take into account yarn curvature is reliable for predicting viscoelastic behavior in textile composites.

Aknowledgements

This research was made possible by a grant awarded to A. El Mourid from Fonds Quebecois de la Recherche sur la Nature et les Technologies. In addition, this work was funded by Pratt and Withney Canada, Rolls Royce Canada, Natural Science and Engineering Research Council of Canada (NSERC) and the Consortium for Research and Innovation in Aerospace in Quebec (CRIAQ).

CHAPTER 4

ARTICLE 2: Effect of temperature on the failure modes of a textile braided polymer matrix composite

A. El Mourid , Rajamohan Ganesan, Myriam Brochu and M. Lévesque. *Submitted to the Journal of the Mechanics and Physics of Solids on August 22, 2014*

Abstract

The temperature effect on the tensile behavior of a triaxially braided composite was investigated in two different loading directions. The damage evolution was monitored and the results were explained with the help of experimental, analytical and numerical methods. At high temperature, it was observed that the yarn and matrix are more compliant than at room temperature. This evolution in the constituent elastic properties was reponsible for stress redistribution within the composite explaining the differences in crack initiation and Ultimate Tensile Strength for both directions and testing temperatures.

keyword

mechanical behavior, elevated temperature, Finite Element Analysis, textile composites, analytical models, mechanical properties, failure analysis

4.1 Introduction

Textile composite can be tailored for specific applications by carefully choosing the fabric type (e.g., woven, braided, knitted, etc.) or microstructure parameters (e.g., volume fraction, yarns spacing, etc.) to obtain desired mechanical properties. Textile composites have already been successfully used in jet engine fan blade components and outer cores where service temperatures are moderate. Recently developed polyimide matrices suitable for Resin Transfer Molding (RTM) have rated operating temperatures of up to 350°C. This paves the way for textile composites use in higher temperature applications, especially in jet engines. Baseline properties, as well as predictive design models, must be available for service conditions to enable the successful deployment of polyimide-based textile composites in high temperature structural applications. For example, thermo-oxydative stability, viscoelastic response (creep/relaxation), fatigue response and damage evolution must all be understood

and predicted to develop optimized designs.

Damage evolution in textile composites has been studied by numerous authors at room temperature (Lomov *et al.*, 2008; Ivanov *et al.*, 2009) and is relatively well documented. During a tensile test, damage is typically initiated by transverse cracks in yarns oriented at an angle with respect to the loading direction (called transverse yarns). Then, as the load increases, the cracks size and density increase. This phenomenon is associated with a decrease in the composite's stiffness. The accumulation of damage creates local yarn/matrix debonding areas. Finally, fibre damage causes material failure.

The influence of elevated temperature (i.e., above 125°C) on composites behavior has also been studied by numerous authors. For example, Odegard and Kumosa (2000) reported decreases of 10% in the axial stiffness (i.e., E_{11}) between room temperature and 316°C for an unidirectional carbon/PMR15 composite submitted to σ_{11}. The deterioration in properties was more pronounced for E_{22} and G_{12}, with decreases of 27% and 80%, respectively, as well as for ultimate strength in the transverse (σ^u_{22}) and shear directions (σ^u_{12}). Kobayashi and Takeda (2002) studied the damage mechanisms in carbon/Bismalmeide (BMI) laminates, both at room temperature and 180°C. They observed that matrix cracks initiated in transverse plies. However, the damage initiated earlier at high temperature and crack density at failure was lower when compared to that measured at room temperature, probably due to matrix softening. Selezneva *et al.* (2011) studied qualitatively the influence of temperature on the failure of carbon/BMI off-axis woven textile composites, for temperatures ranging from 25°C to 205°C. They observed that the areas affected by necking and delamination were significanly larger at elevated temperatures than at room temperature.

Very few studies focused on the mechanical behavior of braided composites at high temperature. For example, Montesano *et al.* (2013) studied the fatigue damage evolution in triaxially braided carbon/polyimide composites, in the warp direction. They concluded that crack density was significantly lower at high temperature in the warp direction, and postulated that it was due to the increased ductility/softening of the matrix at elevated temperatures. Most of these studies (Montesano *et al.*, 2013; Kobayashi and Takeda, 2002; Selezneva *et al.*, 2011) focused on properties along a single direction and neglected the effect of anisotropy.

Analytical and numerical homogenization aim at predicting the effective properties of composites by considering the orientation, mechanical behavior and volume fraction of each constituent (Bornert *et al.*, 2001). Most analytical models rely on Eshelby's solution to the problem of an inclusion embedded into an infinite medium. The most widely used schemes are that of Mori-Tanaka (Benveniste, 1987) and self-consistent techniques (Hill, 1965). These techniques can also estimate the spatially averaged stress tensor in each phase (Benveniste, 1987) and could potentially be used to explain local damage initiation. The mechanical be-

havior of composites can also be predicted by simulating the mechanical response of unit cells describing the exact morphological features of the studied microstructure. This topic has received considerable attention, especially for textile composites (Lomov *et al.*, 2007; Verpoest and Lomov, 2005a; Wong *et al.*, 2006; El Mourid, 2011; Gommers *et al.*, 1998b). In particular, `Wisetex` software provides efficient tools for creating solid or meshed representations of the yarns in 2.5D textiles that can be directly transferred to `ANSYS`. The first step consists of generating a proper 3D volume representation of the textile composite. The second step aims at obtaining an optimized unit cell through symmetries and periodicity. Finally, periodic boundary conditions are imposed and the effective and local fields are computed. However, the numerical modeling textile composites presents challenges for high fibre volume fractions, especially for braided architectures (Lomov *et al.*, 2007). In this case, most volume representations present yarn interpenetrations that have to be taken care of manually before meshing the architecture. High yarns densities can also hinder the matrix phase meshing due to the lack of space between the yarns to create a proper matrix box.
The objetives of this study are to:

- Test up to failure and carefully monitor damage evolution in braided composite samples at different temperatures and along different material orientations.
- Analyze the influence of stress redistribution inside the yarns with analytical and numerical models to explain room temperature and elevated temperature failure sequences.

The experimental methododology is presented in Section 4.2. The experimental results are presented in Section 4.3. The modeling procedure and its results are presented in Section 4.4. The paper ends with a discussion and a summary of the findings.

4.2 Experimental investigation

4.2.1 Material characterization

The studied composite was a tri-axially braided preform infused by RTM with Maverick's MVK10 high temperature polyimide resin. The preforms were fabricated by tri-axially braiding multiple plies of Cytec T650-35 6K dry carbon fibres on a tubular mandrel at $0/\pm 60°$ ($\pm 3°$). The fabric plies were subsequently laid flat, consolidated and placed in a RTM test panel mould to the desired thickness. Fibre volume fraction was aimed to be at 57% ($\pm 3\%$). Preforms were moulded at a pressure of 1700-2100 kPa. The materials were manufactured by ITT Corporation, who withheld the details of the manufacturing process. All the composites were C-Scanned after manufacturing to check for major defects and passed the quality requirements. Test coupons were cut from two 342mm $\times$ 381mm $\times$ 3mm composite panels.

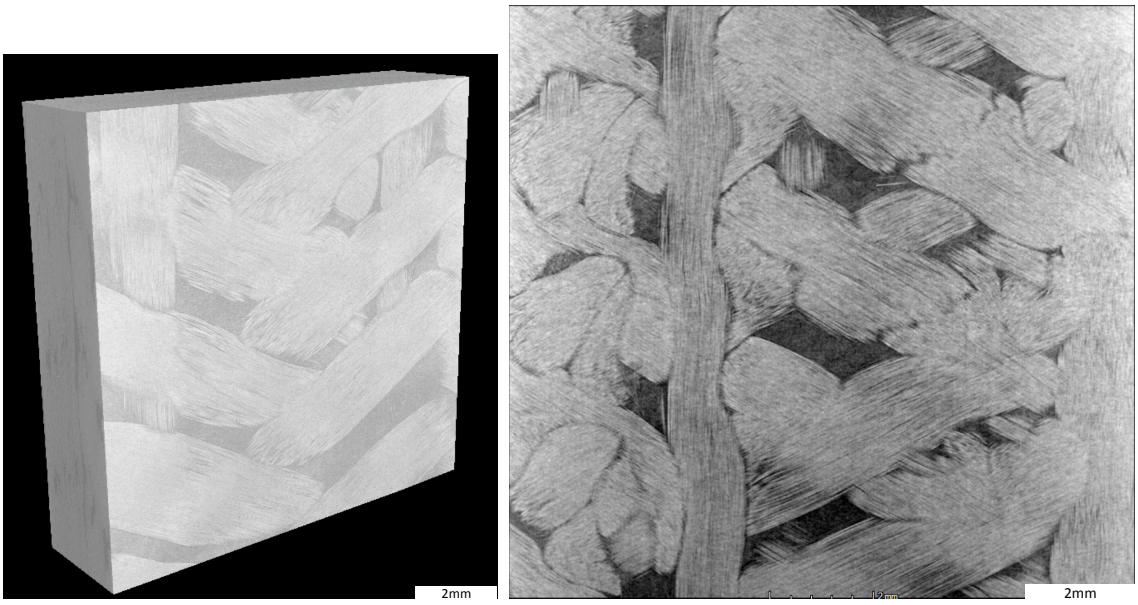

(a) a) Isometric view (b) b) Top view

Figure 4.1 Computed X-Ray Microtomography (μCT) observations of the triaxially braided composite.

Small samples were sent to Southampton University to perform Computed X-Ray Microtomography (μCT) observations. A Nikon XTH 225 L scanner with a Perkin Elmer PE1621 detector and a Molybdenum target, with an accelerating voltage of 55kV and a beam current of 157μA, were used to create the 3D representations. Figure 4.1 displays the results of the tomography and shows the microstructure of the yarns in the composite. These observations allowed for determining the yarns' width, height, separation distances and volume fractions. The fibre volume fraction was evaluated to be 56% based on acid digestion tests. The yarns packing factor (i.e., the fibre volume fraction in a given yarn) was evaluated with the help of image analysis. A 200$\times$ magnification image of a 0° yarn cross-section was transformed into a biphasic image through thresholding. Figure 4.2 shows the raw and thresholded images. The fibre packing factor was then evaluated to be 71%. Table 4.1 reports the results and Figure 4.3 provides an approximate three-dimensional representation of the fabric obtained with `WiseTex` software. In the sequel, Direction 1 is that aligned with the straight yarns while Direction 2 is perpendicular to it, as shown in Figure 4.3. Angles are also measured from Direction 1.

Table 4.1reveals that 80% of the yarns were oriented at $\pm 60°$, while only 20% were at 0°. This led to a composite that was stiffer in Direction 2 (i.e., perpendicular to the straight yarns).

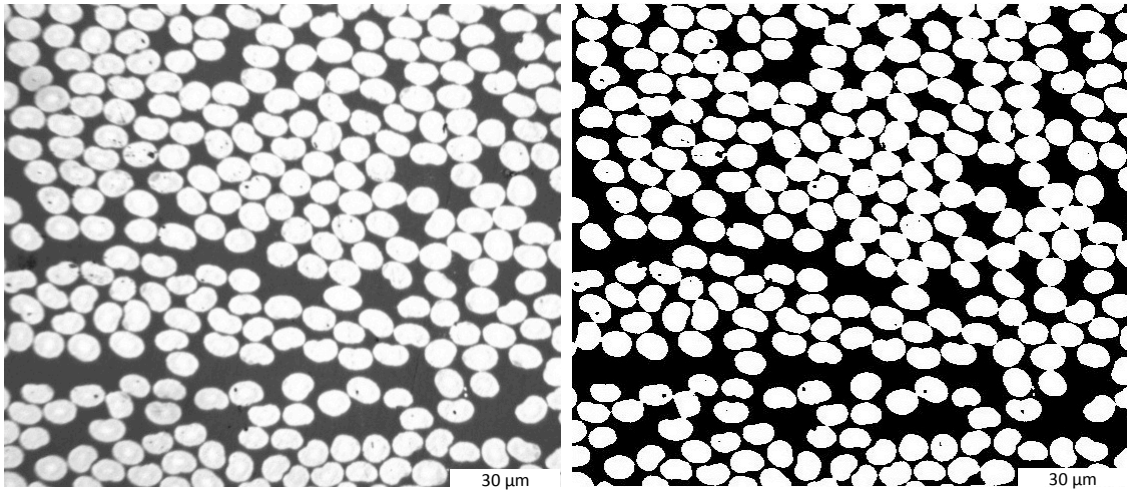

(a) (b)

Figure 4.2 a) Image of the fibre distribution inside a yarn b) Biphasic image used to evaluate the packing factor.

Table 4.1 Braided composite microstructure

Property	Dimension
Yarns width	2.2mm
Yarns height	0.212mm
Distance between 60° yarns	2.7mm
Distance between 0° yarns	3.4mm
Yarns fraction at 60°	40%
Yarn fraction at -60°	40%
Yarns fraction at 0°	20%
Fibre volume fraction	56%
Yarns packing factor	71%

MVK10 dry-glass transition temperature was provided by the manufacturer and was over 300°C. Samples were fully water saturated and the Wet Glass Transition Temperature (wet-T_g) was measured with a Dynamic Mechanical Analyzer (DMA) TA Q800 from TA Instruments and according to ASTM D-7028 standard. As is customary in aerospace applications, T_g was determined as the intersection of the two slopes associated with the storage modulus E' for the glassy and rubbery states. The testing temperature is confidential and was determined according to the aerospace standard of wet-$T_g - 28$°C, which was well above 200°C. .

4.2.2 Normalization procedure

For confidentiality reasons, every composite property was normalized by the equivalent matrix property at room temperature. In the following, E_m, σ_m^u and ε_m^u refer to the matrix Young's modulus, ultimate tensile strength and tensile strain at room temperature. Tensile tests on matrix samples up to failure were performed at room temperature and at wet-T_g − 28°C according to ASTM D638 standard and a controlled displacement rate of $5\text{mm} \cdot \text{min}^{-1}$.

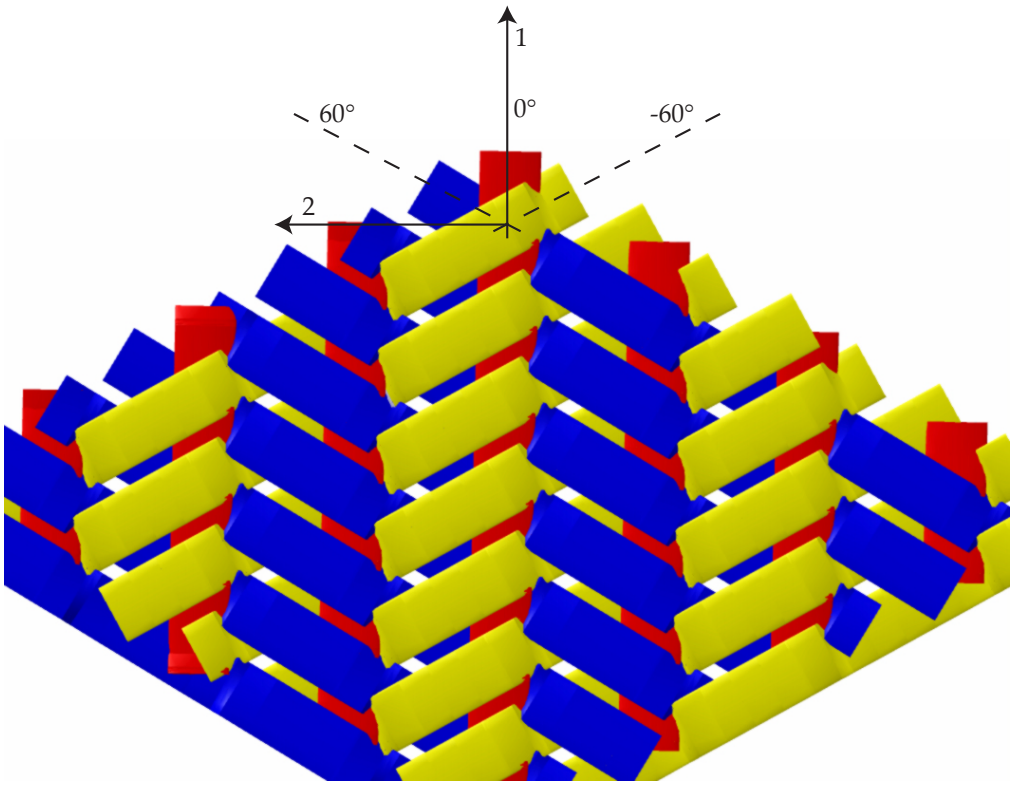

Figure 4.3 3 D model of the triaxially braided composite.

The loading set up consisted of a MTS Insight 50kN electromechanical load frame equipped with a forced convection Lab-Temp LBO-series box environmental chamber from Thermcraft Incorporated. The environmental chamber allows for testing at temperatures up to 425°C with a maximum heating rate of $10°C \cdot min^{-1}$. The sample temperature was measured with a thermocouple set in the gage section during tensile testing. The temperature controls were adjusted manually until the target temperature was reached in the sample gage section. Figure 4.4 shows that the matrix exhibits a brittle behaviour both at room and elevated temperatures. The Young's modulus, ultimate tensile strength and tensile strain decreased respectively by 25%, 53%, and 38% with the increase in temperature from room temperature to wet-$T_g - 28°C$. Finally, it is important to note that ε_m^u was lower than that of carbon fibers, at both temperatures, which influences the damage mechanisms in the composite presented later.

4.2.3 Tensile tests on composite samples

Composite samples were tested in accordance with ASTM D3039 standard with the test set up described above. The samples dimensions were of 165mm × 25.4mm. The specimens were loaded under displacement control at a rate of 2 mm/min. Specimens were initially tested with and without tabs. There was no significant change in the failure mechanisms and ultimate strength observed, and no gripping induced failure occurred. Samples without tabs were therefore used for the rest of the study. The ratio of specimen width to unit cell width was 2.24:1, in accordance with ASTM D6856 standard. The samples were maintained for at least 1 hour at test temperature prior to testing to ensure temperature uniformity. Three samples were tested for each condition, for a total of 12 samples :

- Three samples at room temperature in Direction 1
- Three samples at wet-$T_g - 28°C$ in Direction 1
- Three samples at room temperature in Direction 2
- Three samples at wet-$T_g - 28°C$ in Direction 2

4.2.4 Damage evolution through edge replication and microscopic observations

Damage evolution was monitored through the edge replication technique and microscopic observations. For each temperature and loading direction, 1 sample was polished manually with SiC papers of 120, 240, 400, 600 grit, in that sequence. Diamond suspensions of $6\mu m$, $3\mu m$ and $1\mu m$ were subsequently used to obtain a mirror polish. Finally, an alumina suspension of $0.05\mu m$ was used to provide a final polish and remove the last imperfections.

Vinylpolysiloxane was used to create the replicas due to its ease of use in comparison with replicating film and acetone. Room temperature tests were paused at various load levels for the replication compound application. The viscous polymer was applied on a solid surface and pressed against the edge of the specimen for 5 minutes, until it solidified completely, keeping an imprint of the specimen on its surface. High temperature tests were conducted by pausing the test at a given load level, decreasing the load to a very low value, by decreasing the temperature down to 60°C and applying the vinylpolysiloxane paste. The specimen was subsequently heated back, and testing resumed up to the next load level. The replicas were observed under a NIKON Eclipse ME600D microscope, at a 50X magnification. Damage evolution was therefore tracked with this procedure without unmounting the specimen from the test chamber. The average area of each replica was around 120mm^2. 10 observations over a surface of 2.5 mm^2 were performed to evaluate the average crack density on each replica. Figure 5.5a displays the edge of a Direction 1 specimen. On this edge, 0° yarns appear as long strands while ±60° appear as ellipses. Figure 5.5b displays the edge of a Direction 2 specimen. On this edge, 0° yarns appear as ellipses while ±60° yarns appear as curved strands. Figure 4.6 shows typical photographs of the replicas of polished surfaces for samples cut in Directions 1 and 2.

Cross-sections of failed specimens were also observed under the microscope to confirm that the same damage occurred inside the composite sample. The cross-sections were cut from samples and mounted in Bakelite, polished with the same procedure described above and observed on a Leitz Metallovert inverted microscope, at a 50X magnification.

4.3 Experimental results

4.3.1 Tensile tests on composites

Figure 4.7 shows the averaged stress-strain curves obtained for samples tested at room temperature and wet-T_g − 28°C, in Directions 1 and 2 (3 samples per condition). Tables 4.2 and 4.3 list the Young's modulus and Ultimate Tensile Strength (UTS) for each of the samples tested in Directions 1 and 2, respectively. Appendix B provides additional statistical information about all tested samples.

Direction 1 samples tested at room temperature exhibited a bilinear behaviour, with a softening (decrease in modulus) occurring when the load reached between 54% and 68% of UTS in that direction, as can be seen in Figure 4.8. At wet-T_g − 28°C, the stress-strain curve is almost linear, with no sign of softening. The Direction 1 samples tested at room temperature had an ultimate tensile strength 8.35 times that of σ_m^u at room temperature and 7.9 times that of σ_m^u when tested at wet-T_g − 28°C, which corresponds to a decrease of 6 %.

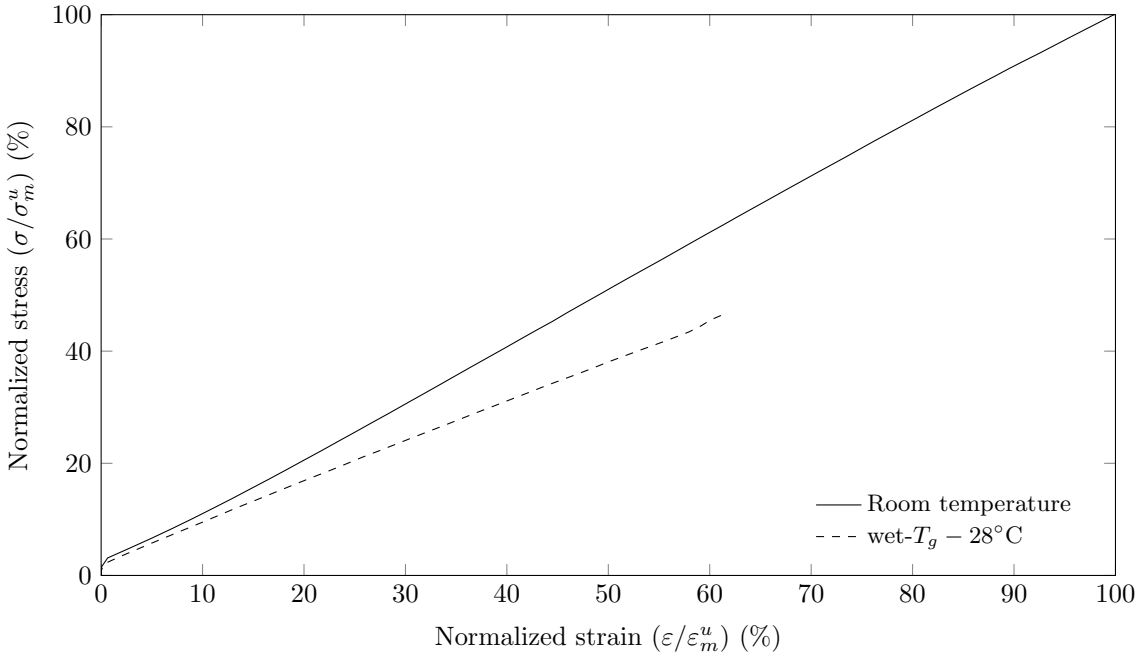

Figure 4.4 Tensile testing up to failure of matrix samples at room temperature and wet-$T_g - 28°C$.

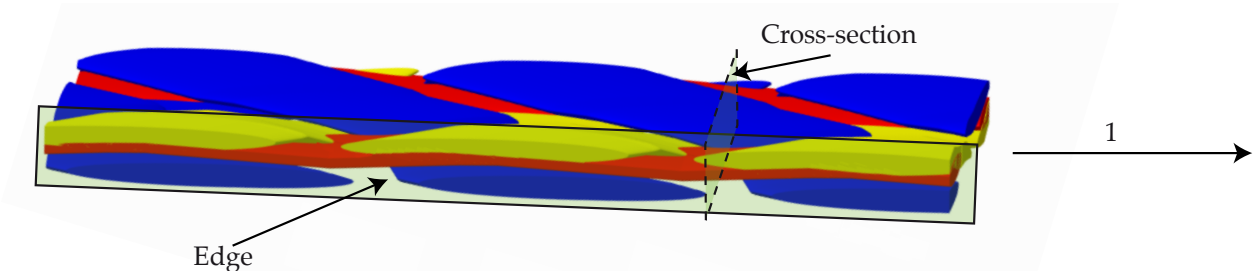

(a) Observation planes on Direction 1 samples

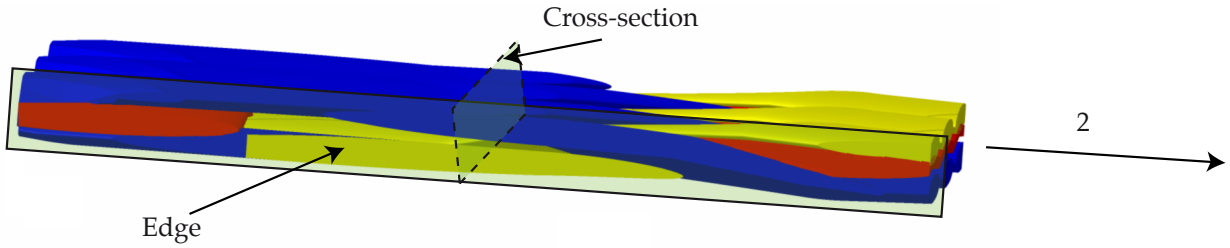

(b) Observation planes on Direction 2 samples

Figure 4.5 Observation planes on a) Direction 1 and b) Direction 2 samples.

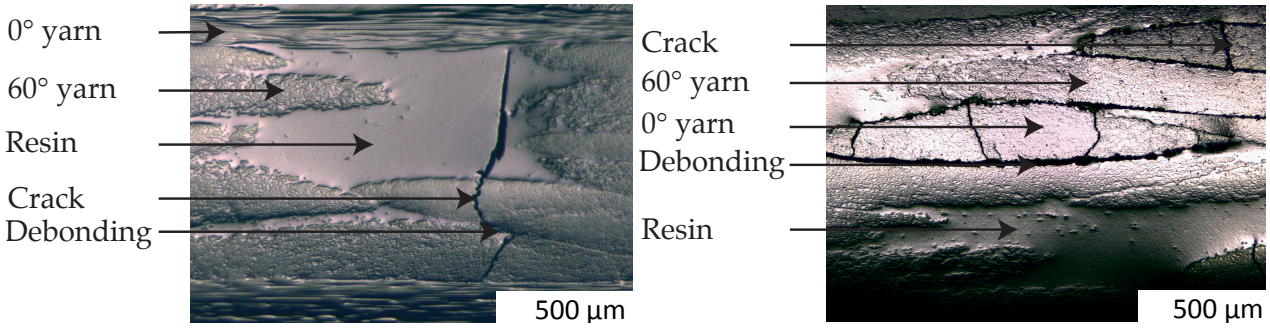

(a) (b)

Figure 4.6 Typical examples of the results of edge replication for samples cut along a) Direction 1 and b) Direction 2, at a 50X magnification.

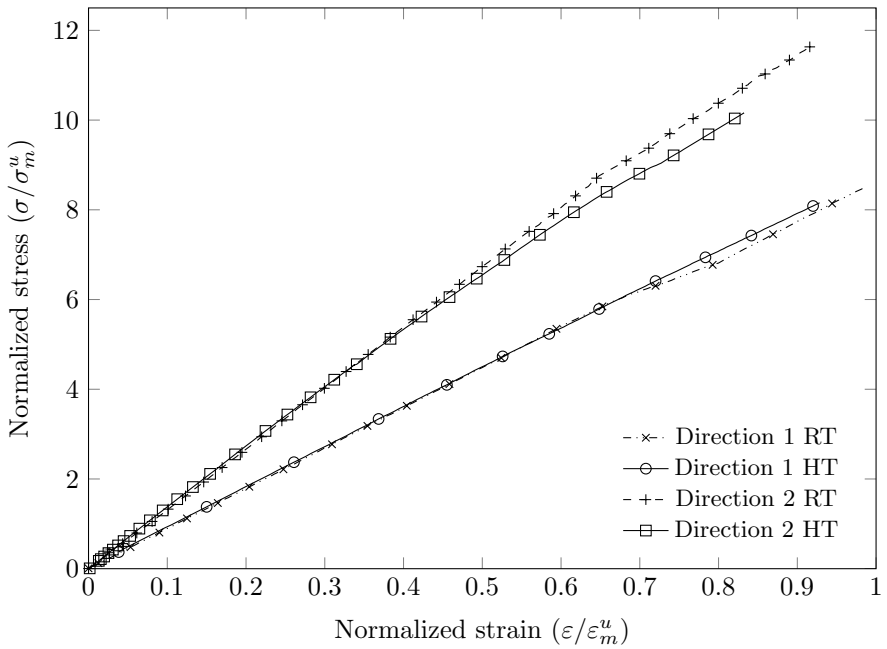

Figure 4.7 Tensile stress-strain curves of the composite material for both directions and testing temperatures (Room Temperature (RT) and wet-$T_g - 28°$C (HT))

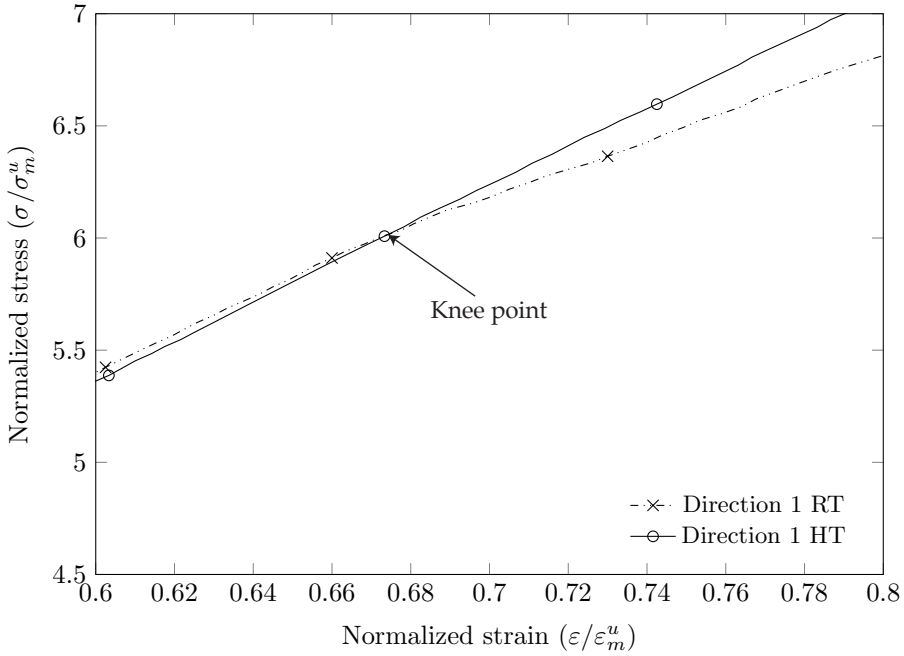

Figure 4.8 Zoom on the knee point for tensile stress-strain curves for Direction 1 samples tested at Room Temperature (RT) and wet-$T_g - 28°C$ (HT).

Table 4.2 Tensile properties of Direction 1 samples

Direction 1	Temperature	E_{11}/E_m	E_{11}/E_m at failure	σ_{11}^u/σ_m^u	$\varepsilon_{11}^u/\varepsilon_m^u$
Sample 1	Room	8.75	7.92	8.2	0.95
Sample 2	Room	8.82	7.74	8.3	1.01
Sample 3	Room	8.93	7.76	8.6	1.00
Average Direction 1	Room	**8.83**	**7.8**	**8.35**	**0.99**
Sample 4	wet-$T_g - 28°C$	8.48	8.37	7.7	0.88
Sample 5	wet-$T_g - 28°C$	8.40	8.21	8.1	0.92
Sample 6	wet-$T_g - 28°C$	8.27	8.30	7.9	0.91
Average Direction 1	wet-$T_g - 28°C$	**8.21**	**8.91**	**7.9**	**0.90**

Table 4.3 Tensile properties of Direction 2 samples

Direction 2	Temperature	E_{22}/E_m	E_{22}/E_m at failure	σ^u_{22}/σ^u_m	$\varepsilon^u_{22}/\varepsilon^u_m$
Sample 1	Room	13.7	10.77	11.5	0.91
Sample 2	Room	13.8	13.2	11.7	0.86
Sample 3	Room	13.9	10.74	11.3	0.88
Average Direction 2	Room	**13.8**	**11.8**	**11.5**	**0.88**
Sample 4	wet-$T_g - 28°$C	13.44	9.86	9.2	0.70
Sample 5	wet-$T_g - 28°$C	13.22	10.69	10.2	0.80
Sample 6	wet-$T_g - 28°$C	13.28	10.58	10.4	0.82
Average Direction 2	wet-$T_g - 28°$C	**13.30**	**10.40**	**9.9**	**0.78**

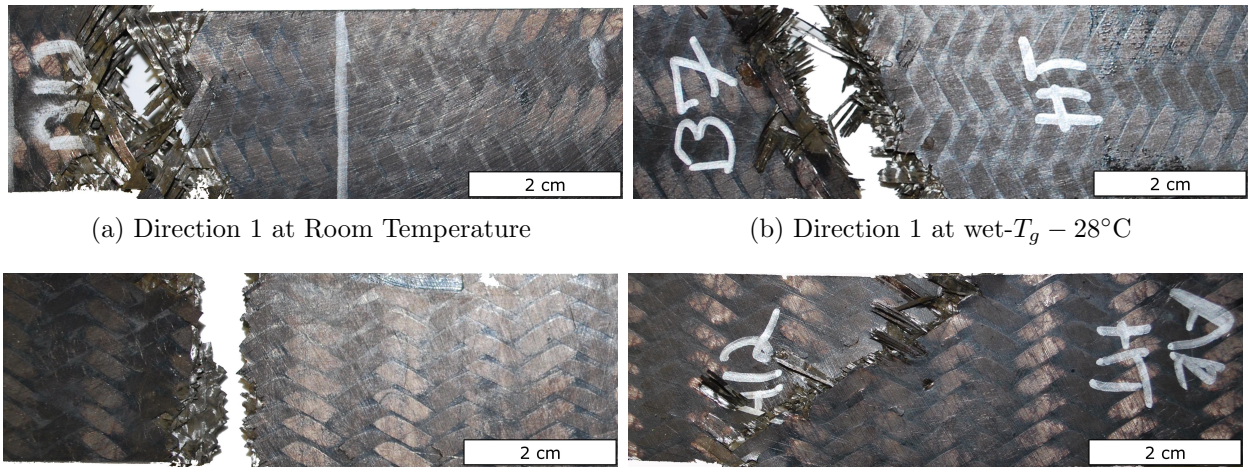

(a) Direction 1 at Room Temperature

(b) Direction 1 at wet-$T_g - 28°$C

(c) Direction 2 at Room Temperature

(d) Direction 2 at wet-$T_g - 28°$C

Figure 4.9 Examples of Directions 1 and 2 samples failures at room temperature and at wet-$T_g - 28°$C.

These results are consistent with those obtained by Montesano *et al.* (2013), who conducted tensile tests on the same material in Direction 1 at the same temperature. It should be noted that matrix samples exhibited a 45% decrease in UTS when tested under similar conditions. The relatively good properties retention of Direction 1 samples is most likely attributed to the fact that the 0° yarns were aligned with the loading direction. The samples failed for both temperatures along the ±60° yarns, in a straight line or V-pattern shape, as can be seen in Figure 4.9.

Direction 2 samples exhibited a significantly different behaviour. First, a gradual softening was observed at both temperatures. As expected, both UTS and stiffness were considerably higher for Direction 2 samples, when compared to those for Direction 1 samples, since 80% of the yarns lied within ±30° of that direction. Another interesting observation is that UTS

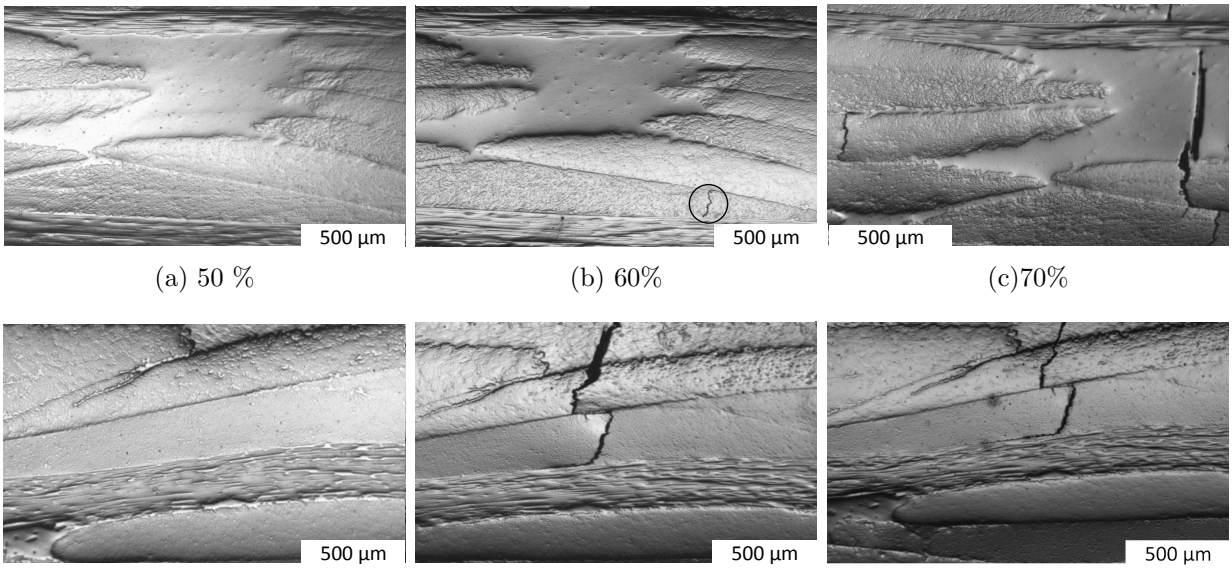

(a) 50 % (b) 60% (c)70%

(d)60% (e)70% (f)90%

Figure 4.10 Replicas under different stress levels expressed in % of UTS at the same location at the edge of a Direction 1 sample, tested at room temperature, at a 50X magnification.

at wet-$T_g - 28°$C was 15.6 % lower than that at room temperature, while slight changes (6%) were observed for Direction 1 samples under similar conditions. Room temperature failure occurred along the 0° yarns while that at high temperature occurred mostly along the ± 60° yarns, but also along the ± 60° yarns and 0° yarns for some samples (see Figure 4.9). These observations could be explained by the fact that the ± 60° yarns, which provide most of the load carrying capabilities in Direction 2, were loaded in matrix dominated shear/transverse modes.

Edge replication

Figure 4.10 shows the results of edge replication, at the same location and for different load levels, for a sample cut in Direction 1 tested at room temperature. The figure shows that transverse cracks appeared in the ±60° yarns for loads between 60% and 70% of the UTS, which corresponds to the knee point observed in Figure 4.7. The first crack is circled on the figure. Additional cracks appeared in the ±60° yarns and matrix cracking occurred in the composite as the load increased. This limited the ability of the ±60° yarns to carry the load and initiated failure along the ±60° yarns, as shown in Figure 4.9.

Interestingly, less damage was observed in the ±60° yarns for samples tested at wet-$T_g - 28°$C, as can be seen in Figure 4.11. Figure 4.12 shows failed Direction 1 samples cross-sections after tensile testing at room temperature and wet-T_g - 28°C. While several

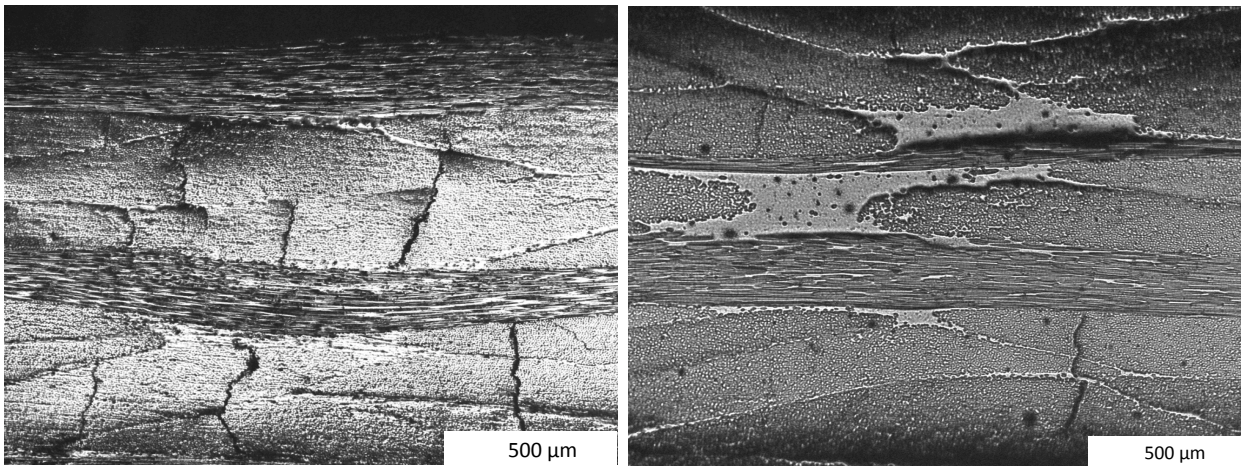

(a) 90 %, room temperature (b) 90%, wet-$T_g - 28°C$

Figure 4.11 Replicas for Direction 1 samples at 90 % of UTS, at room temperature and wet-$T_g - 28°C$.

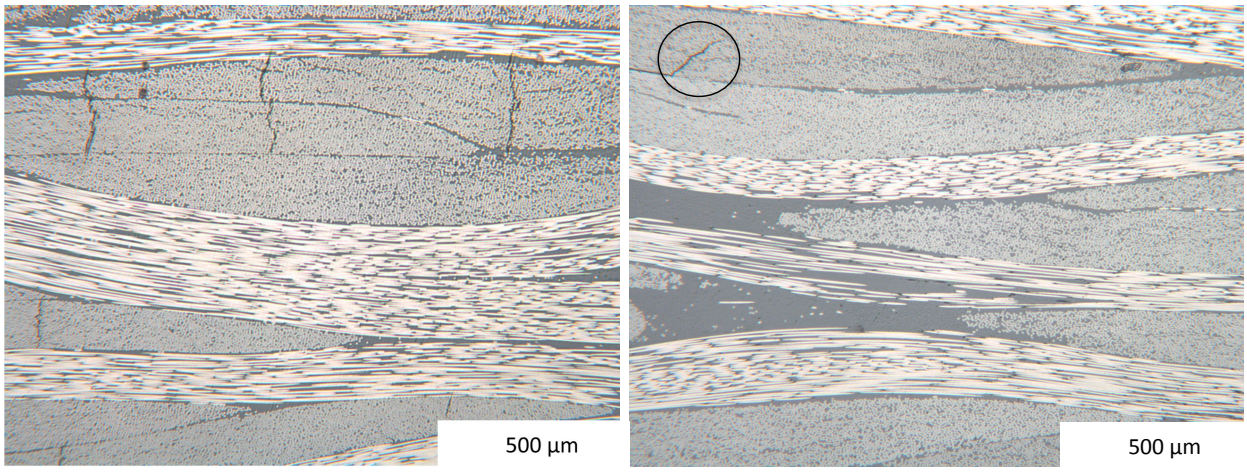

(a) Room temperature (b) wet-$T_g - 28°C$

Figure 4.12 Cross-sections of Direction 1 samples at room temperature and at high temperature, after failure, at a 50X magnification.

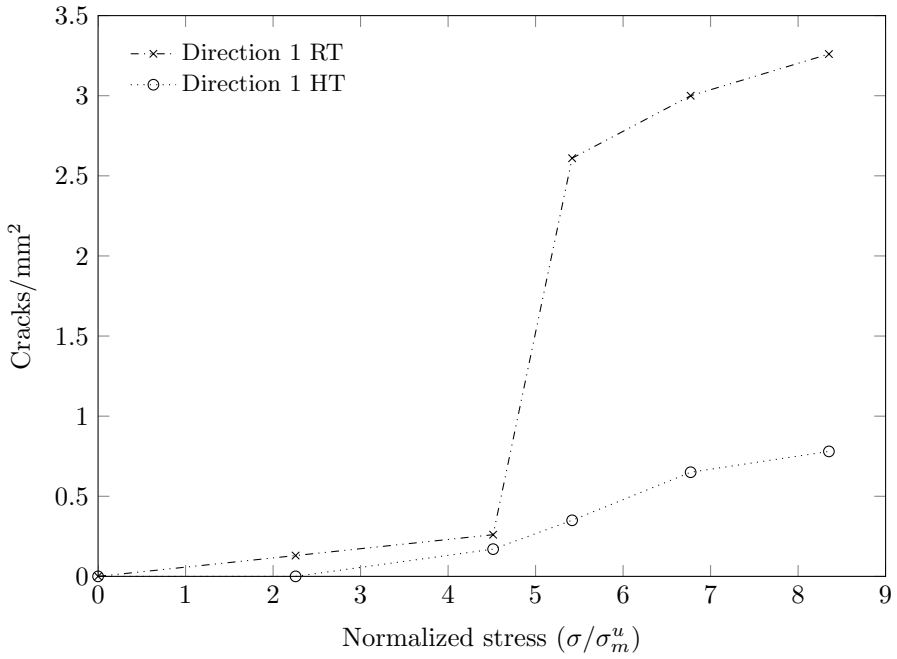

Figure 4.13 Crack density of a Direction 1 sample as a function of the applied tensile stress at Room Temperature (RT) and at wet-$T_g - 28°$C (HT).

cracks are observable on the sample tested at room temperature, only one can be seen on the sample tested at wet-$T_g - 28°$C (this crack is circled on the figure). This observation concurs with the fact that the stress-strain curve was linear until failure for Direction 1 samples tested at wet-$T_g - 28°$C. Figure 4.13 shows a quantitative analysis of the crack density for samples tested in Direction 1. Appendix A explains the crack counting methodology. The replicas revealed that the damage was confined to the $\pm 60°$ yarns without ever reaching the $0°$ yarns or evolving into yarn debondings. This corresponds to a low damage level for textile composite structures. Coupled with the low failure strain of the matrix, these observations suggest that a brittle matrix failure reaching its ultimate strain is responsible for the composite failure, before the occurrence of yarns debonding and progressive damage.

Significantly different results were obtained for samples tested in Direction 2. Figure 4.14 shows that transverse cracks appeared in the $0°$ yarns at 40% of UTS for specimens tested at room temperature. As the load increased, debonding of the $0°$ yarns occurred, which eventually caused the cracks to propagate to the adjacent $\pm 60°$ yarns, causing the final failure of the sample along the $0°$ yarns. Figure 4.15 plots the crack density evolution in the tested samples, for each type of crack. The damage evolution recorded with the help of replicas is a confirmation of the damage theory of textile composites presented in the

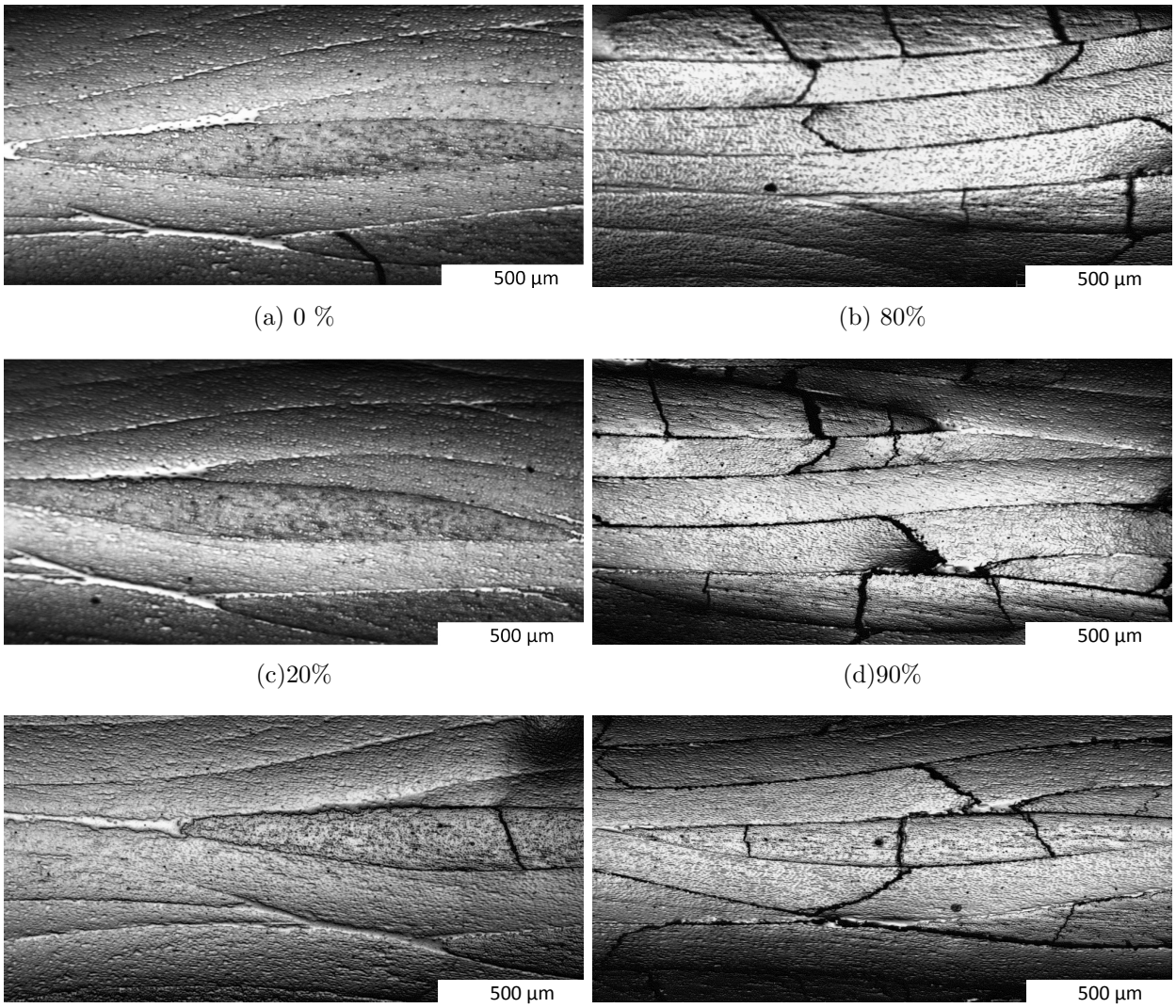

(a) 0 %

(b) 80%

(c)20%

(d)90%

(e)40%

(f)100%

Figure 4.14 Replicas under different stress levels at the same location on the edge of a Direction 2 sample, tested at room temperature, at a 50X maginification. The dark artefact visible on the 0% image is cloth dust, not a crack.

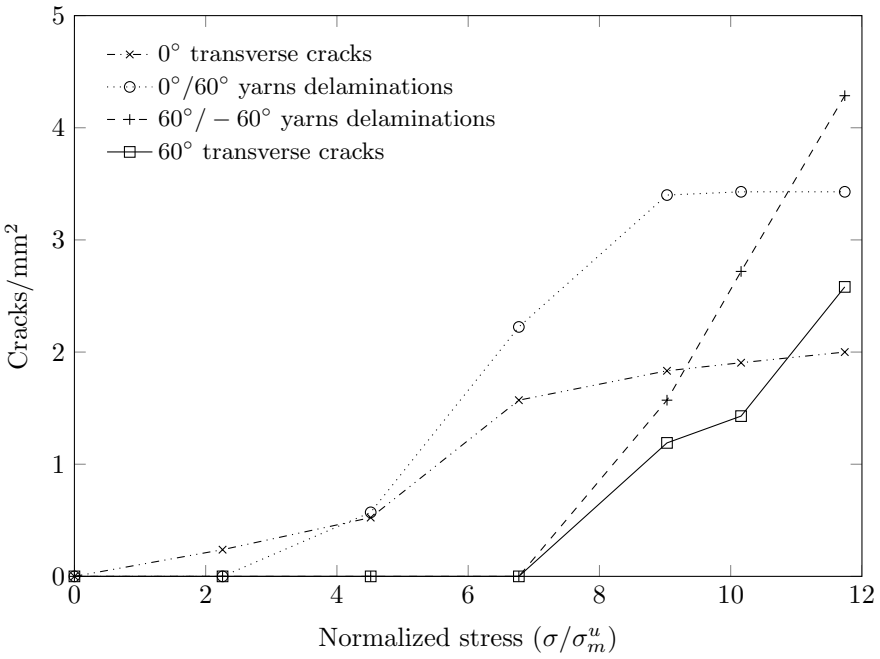

Figure 4.15 Crack density of a Direction 2 sample at room temperature.

literature (Ivanov *et al.*, 2009). The softening observed in that direction results from damage initiation in 0° yarns, followed by damage in the ± 60° yarns.

Similar results were observed for the samples cut in Direction 2 and tested at wet-$T_g - 28°$C. Figure 4.16 show the damage development at wet-$T_g - 28°$C recorded by edge replication. An initial transverse crack can be observed before loading. More transverse cracks appeared in the 0° yarns at around 25% of UTS at wet-$T_g - 28°$C, which is earlier than what was observed under similar conditions at room temperature. As the load increased, debonding surrounding the 0° yarns eventually caused the cracks to propagate to the adjacent ±60° yarns. A notable difference with the room temperature samples was the extensive debonding of the ±60° yarns under high loads (90% of UTS). Figure 4.17 also plots the crack density evolution in the tested samples, for each type of crack. The debonding of all the yarns created two possible failure paths, as seen in Figure 4.9. This could be an explanation for the lower UTS for the samples tested at wet-$T_g - 28°$C.

4.3.2 Summary

- Temperature had a moderate effect on elastic properties. Young's modulus decreased by 3.75% in Direction 1 and by 3.3% in Direction 2 between room temperature and wet-$T_g - 28°$C.

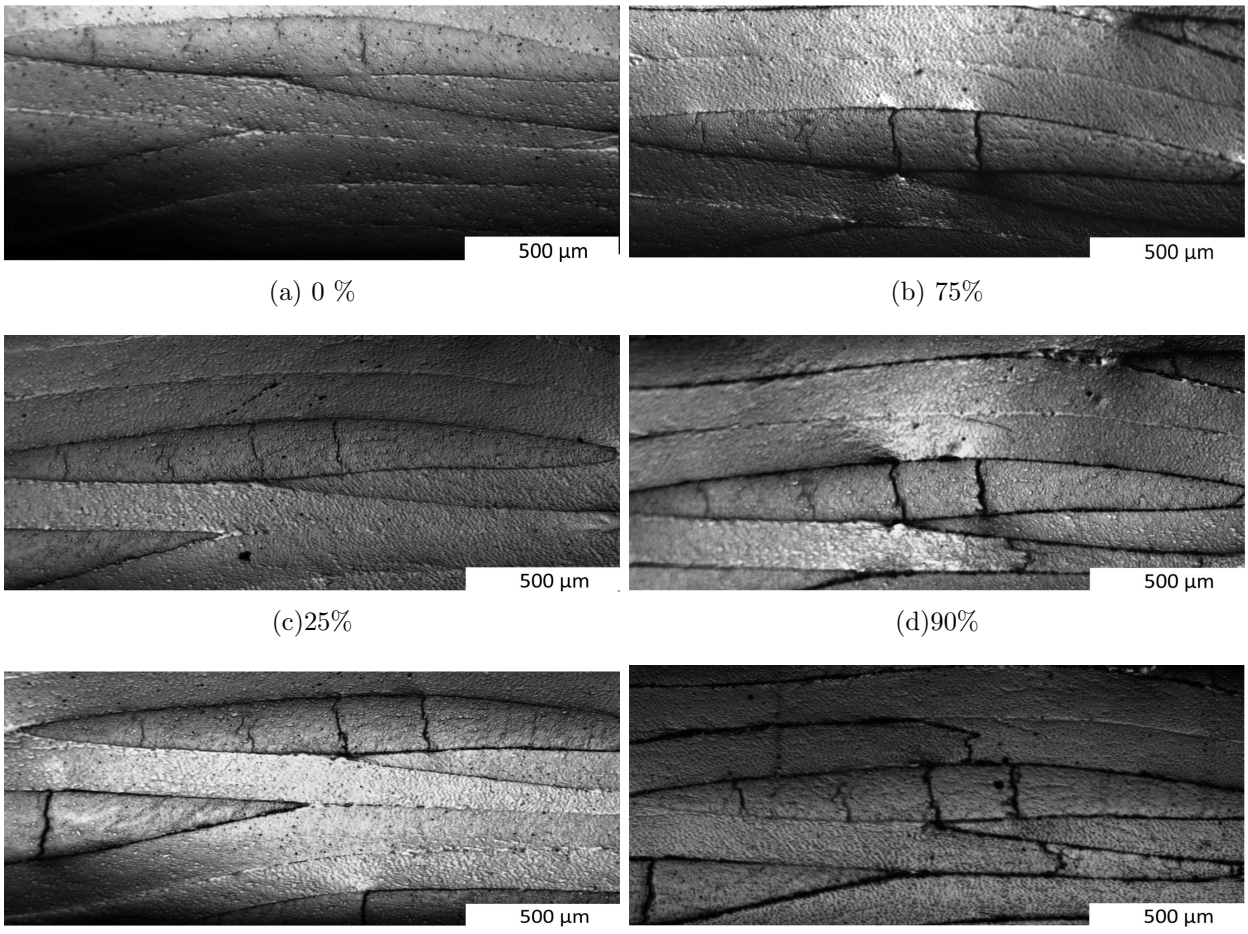

(a) 0 %

(b) 75%

(c)25%

(d)90%

(e)50%

(f)100%

Figure 4.16 Replicas under different stress levels at the same location on the edge of a Direction 2 sample, tested at wet-$T_g - 28°$C, at a 50X magnification.

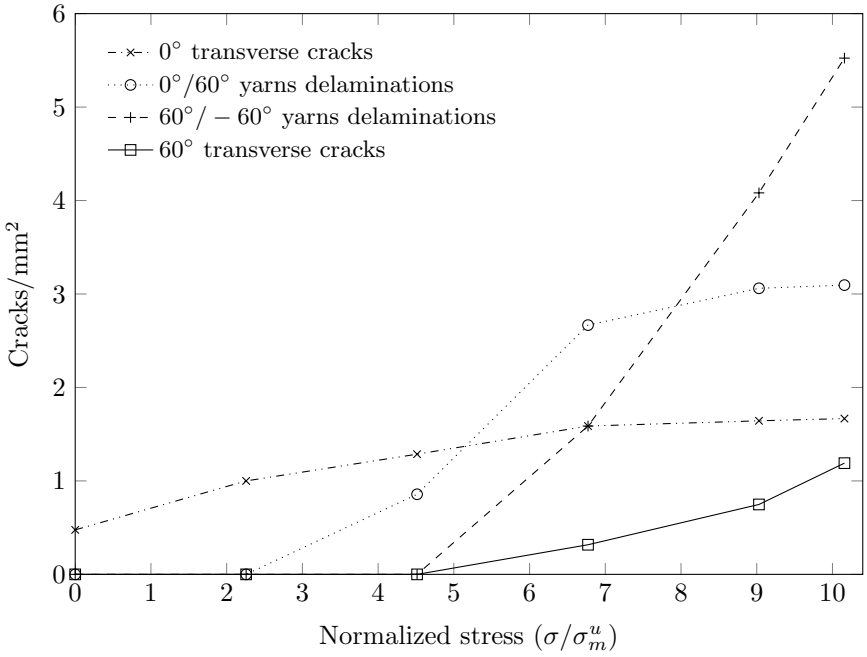

Figure 4.17 Crack density of a Direction 2 sample at wet-$T_g - 28°C$.

- Temperature had a meaningful impact on ultimate strength, depending on the yarns orientation. When compared to room temperature results, tensile testing at wet-$T_g - 28°C$ decreased by 5.7% and 16% the UTS of Direction 1 and Direction 2 samples, respectively.

- Temperature influenced the damage mechanisms for samples cut in Direction 1. The bilinear curve at room temperature is the consequence of damage in the $\pm$ 60° yarns, observed in edge replica. The decrease of the density of these cracks at wet-$T_g - 28°C$ concurs with the observed linear stress strain curve.

- Temperature influenced the damage mechanisms for samples cut in direction 2. Cracks appeared at an earlier load at elevated temperature for the $\pm$ 60° yarns. The failure was along the 60° yarns at wet-$T_g - 28°C$ by opposition to that at room temperature, which was along the 0° yarns..

In addition, several factors support the fact that Direction 1 samples' UTS could be directly related to the 0° yarns strength. At room temperature, crack saturation was reached long before specimen failure. Specimens tested at room temperature and at wet-$T_g - 28°C$ failed at almost the same load, even if samples tested at wet-$T_g - 28°C$ exhibited no transverse cracks.

Overall, it can be seen that different damage mechanisms initiation and development lead to

different macroscopic failure results, depending on the temperature and the loading conditions. Yarns properties evolution with temperature, leading to stress redistribution between the yarns in the composite architecture, could explain the differences in damage mechanisms and UTS results. This hypothesis is investigated further in the following section.

4.4 Analysis and modelling

4.4.1 Analytical homogenization models for ellipsoids-reinforced composites

The basics of analytical homogenization were extensively discussed in El Mourid *et al.* (2013) and are briefly recalled here. The effective stiffness tensor $\tilde{\mathbf{C}}$ of a two-phase composite was defined by Dunn *et al.* (1996) as:

$$\tilde{\mathbf{C}} = \mathbf{C}_0 + \rho_1(< \mathbf{C}_1 : \mathbf{A} > - \mathbf{C}_0 :< \mathbf{A} >) \tag{4.1}$$

where $\mathbf{A}$ is the so-called 4^{th} order strain localization tensor, ρ_1 the volume fraction of the reinforcing phase, $\mathbf{C}_1$ the stiffness of the reinforcing phase and $\mathbf{C}_0$ the matrix' stiffness. Symbol $\langle\cdot\rangle$ represents orientation averaging. The main difference between the various homogenization schemes lies in the evaluation of the strain localization tensor $\mathbf{A}$. The strain localization tensor $\mathbf{A}_{\text{MT}}$ for the Mori-Tanaka method (Benveniste, 1987) is given by:

$$\mathbf{A}_{\text{MT}} = \mathbf{T} : [\rho_0 \mathbf{I} + \rho_1 \mathbf{T}]^{-1} \tag{4.2a}$$

$$\mathbf{T} = \left[\mathbf{I} + \mathbf{E} : \mathbf{C}_0^{-1} : (\mathbf{C}_1 - \mathbf{C}_0)\right]^{-1} \tag{4.2b}$$

where $\mathbf{E}$ is Eshelby's tensor, ρ_0 the matrix' volume fraction and $\mathbf{I}$ the 4^{th} order identity tensor. The Mori-Tanaka method was extended by Gommers *et al.* (1998a) to evaluate the mechanical properties of textile composites. The approach consists of approximating the yarn geometry by a series of "divided" inclusions. An inclusion-based homogenization model is then used for computing the composite's effective properties by taking into account the inclusions' geometry and distribution of orientations.

The yarns studied in this work were assumed to have an elliptical cross-section. An ellipsoidal inclusion is defined by three characteristic dimensions a_1, a_2 and a_3, with a_1 being the characteristic length while a_2 and a_3 being the ellipse's half-axes. Ratios $\frac{a_1}{a_2}$, $\frac{a_2}{a_3}$ and $\frac{a_1}{a_3}$ were used to compute Eshelby's tensor (Mura, 1982). Huysman *et al.* (1998) proposed taking into

account the yarns curvature by evaluating the aspect ratio according to:

$$a_1 = \lambda \frac{k}{a_2} \tag{4.3}$$

where k is the yarn's local curvature radius and λ is a calibration factor. In their paper, Huysman *et al.* (1998) set $\lambda = \pi$. The stiffness tensor was evaluated by replacing every yarn by a discrete set of inclusions for which a_1 was evaluated with the local curvature. The specific yarns arrangement was then described by a discrete set of orientations. Each inclusion was oriented according to specific values of $\{\phi, \theta\}$. The third angle β was not required since there is almost no rotation of the yarns around their principal axis. The orientations of the textile architecture were stored in a probability function, called the Orientations Distribution Function (ODF), which can be discrete or continuous. For example, if the yarns are divided into 20 ellipsoidal inclusions, the homogenization equation is carried out over 20 different inclusions, each with its own set of angles $\{\phi, \theta\}$ and aspect ratio $\{a_1, a_2, a_3\}$. The homogenized response was then evaluated with the following equations:

$$\mathbf{D} = (\mathbf{C}_1 - \mathbf{C}_0) : \mathbf{A} \tag{4.4a}$$

$$\tilde{C}_{ijkl} = C_{0_{ijkl}} + \sum_{z=1}^{N} \frac{\rho_1}{n} \alpha_{im}(\theta_z, \phi_z)\, \alpha_{jn}(\theta_z, \phi_z)\, \alpha_{ko}(\theta_z, \phi_z)\, \alpha_{lp}(\theta_z, \phi_z)\, D_{mnop} \tag{4.4b}$$

where α_{im} has as its column the orthornomal basis vectors defined by the Euler angles $\{\theta, \phi, \beta\}$. Equations (4.4) are therefore discrete representations of Equation (4.1). The yarns Orientations Distribution Function (ODF) was computed from `Wisetex`, as for the numerical models. The yarns effective properties were evaluated according to the methodology of Chamis (1989) as:

$$E_{y_{11}} = k_f E_{f_{11}} + (1 - k_f) E_m \tag{4.5a}$$

$$E_{y_{22}} = \frac{E_m}{1 - \sqrt{k_f}\left(1 - \frac{E_m}{E_{f_{22}}}\right)} \tag{4.5b}$$

$$G_{y_{12}} = G_{y_{13}} = \frac{G_m}{1 - \sqrt{k_f}\left(1 - \frac{G_m}{G_{f_{12}}}\right)} \tag{4.5c}$$

$$G_{y_{23}} = \frac{G_m}{1 - \sqrt{k_f}\left(1 - \frac{G_m}{G_{f_{23}}}\right)} \tag{4.5d}$$

Table 4.4 Yarns properties

	$E_{y_{11}}/E_m$	$E_{y_{22}}/E_m$	$\nu_{y_{12}}$	$G_{y_{23}}/G_m$	$G_{y_{12}}/G_m$
Room temperature	47.6	2.7	0.32	2.9	5.3
wet-$T_g - 28°C$	47.5	2.4	0.30	2.5	4.2

$$\nu_{y_{12}} = k_f v_{f_{12}} + (1 - k_f)\, v_m \tag{4.5e}$$

$$\nu_{y_{23}} = \frac{E_{y_{22}}}{2G_{y_{23}}} - 1 \tag{4.5f}$$

where subscript y refers to the yarns and k_f is the packing factor. This model assumes that the yarns are transversely isotropic, as the carbon fibres. Yarns properties evaluated with Equation (4.5) are presented in Table 4.4. For comparison purposes, the rule of mixture was computed using the same methodology, with the only difference being the strain localization tensor $\mathbf{A} = \mathbf{I}$.

4.4.2 Numerical models for predicting the response of the composites

Lomov *et al.* (2007) discussed the difficulties and methodolodgies to mesh high fibre volumes textile architectures with constant cross-sections because of yarn interpenetration problems. The authors concluded that the ultimate geometrical model handling volume interpenetrations had yet to be developed. Preliminary attempts made with `Wisetex` software failed at generating consistent Representative Volume Elements (RVE) of the studied composite. The first problem lied with the high fibre volume fraction, which resulted in interpenetrations between adjacent yarns. These interpenetrations could be manually corrected for some of the yarns, but not for all. The second problem lied in the packing factor. The yarns had an average packing factor of 0.71. Since the composite fibre volume fraction was 0.56, the yarns volume fraction was close to 0.79. Obtaining a continuous matrix box for such a high volume fraction with yarns of constant cross-section was impossible. Many authors (Verpoest and Lomov, 2005a; Lomov *et al.*, 2005) argue that it is possible to artificially increase the packing factor, as long as the fibre volume fraction is kept constant, to create enough space between the yarns to be able to mesh the matrix box. However, this methodology can lead to artificially increased stiffness. Due to these limitations, the classical approach to create a RVE was abandoned and a new strategy was devised.

In the classical approach, the volumes of the yarns and the matrix box are created before being meshed. It is possible to invert these two steps, by first meshing the volume element

(a) (b) (c)

Figure 4.18 a) Representation of a yarn b) Yarn with its defining cross-sections c) Cross-sections with their local coordinate systems

with a uniform mesh, and then by identifying the elements inside the volumes. This approach eluded the problem of yarns interpenetrations since the elements inside the interpenetration zones are associated with one of the yarns. It also solved the meshing problem for the matrix box. The necessary steps to create the RVE became :

- Create a prismatic box including the volumes of the yarns and of the matrix.
- Mesh the RVE box with mapped 20-node brick elements. The bricks decrease the number of required elements and converge faster than tetrahedral elements.
- Identify the elements that belonged to the 60°, -60° and 0° yarns.
- Change the element coordinate system and the material properties of the selected elements in order to take into account fiber weaviness.
- Apply periodic boundary conditions.
- Solve the FE problem.

The challenge in this methodology was to identify the elements belonging to each yarn. The yarns are in fact series of volumes generated from `Wisetex`, with attached local coordinate systems, as can be seen in Figure 4.18. The following procedure was developed for identifying the elements in the yarns:

- Each yarn segment was defined by a keypoint at the centre of the originating ellipse, a local coordinate system and the characteristic ellipse length l_{seg}.
- For every yarn segment, each element for which the local x-coordinate of the centroid respects : $0 \leq x \leq l_{seg}$ was selected.

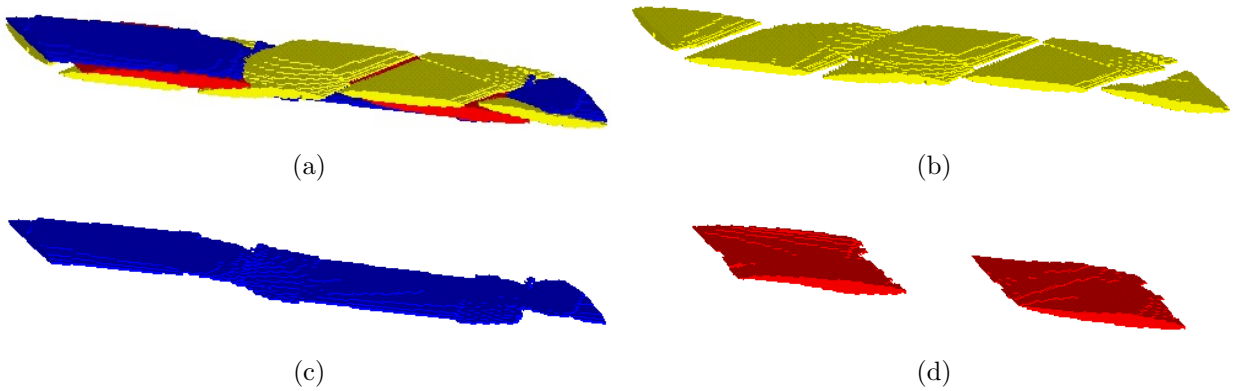

(a) (b)

(c) (d)

Figure 4.19 a) RVE meshed with brick elements b)-60° yarns in the RVE. c)60° yarns in the RVE. d)0° yarns in the RVE.

- Each element from that group for which the local y- and z-coordinates of the centroid satisfied the ellipse equation :

$$\left(\frac{y}{a}\right)^2 + \left(\frac{z}{b}\right)^2 \leq 1 \tag{4.6}$$

  where a and b are the lengths of the principal axes, were selected.

- The material properties of these elements were set to those of the yarns

- The local element coordinate system (used also for materials directions) was aligned with that of the generating ellipse.

There were 30, 18 and 12 yarn segments for the -60°, 60° and 0° yarns, respectively. The -60° yarns were given priority because they had the most cross-sections. Because of the interpenetrations, the volume fractions of the 60° and 0° yarns were initially slightly lower than the desired targets. To correct that problem, their cross-sections' dimensions were incrementally increased, until reaching the desired yarn volume fraction. Figures 4.19b, 4.19c and 4.19d display the results for -60°, 60° and 0° yarns, respectively.
The periodic boundary conditions were programmed with the help of `ANSYS` Parametric Design Language (APDL). Six independent periodic unitary displacements, presented in Table 4.5, were consecutively applied to simulate tensile tests. Finite element solution of this problem provided stresses $\boldsymbol{\sigma}(\boldsymbol{x})$ in all elements. The effective stress tensor $\boldsymbol{\Sigma}$ was obtained according to:

$$\boldsymbol{\Sigma} = \frac{1}{V}\sum_{n=1}^{N} \boldsymbol{\sigma}_n V_n \tag{4.7}$$

Table 4.5 Unitary displacements applied to obtain the stiffness tensor and the corresponding components of the stiffness tensor.

Unitary displacement	Applied strain	Components of the stiffness tensor
1	$[0.01; 0; 0; 0; 0; 0]^T$	$\bar{C}_{11}; \bar{C}_{21}; \bar{C}_{31}; \bar{C}_{41}; \bar{C}_{51}; \bar{C}_{61}$
2	$[0; 0.01; 0; 0; 0; 0]^T$	$\bar{C}_{12}; \bar{C}_{22}; \bar{C}_{32}; \bar{C}_{42}; \bar{C}_{52}; \bar{C}_{62}$
3	$[0; 0; 0.01; 0; 0; 0]^T$	$\bar{C}_{13}; \bar{C}_{23}; \bar{C}_{33}; \bar{C}_{43}; \bar{C}_{53}; \bar{C}_{63}$
4	$[0; 0; 0; 0.02; 0; 0]^T$	$\bar{C}_{14}; \bar{C}_{24}; \bar{C}_{34}; \bar{C}_{44}; \bar{C}_{54}; \bar{C}_{64}$
5	$[0; 0; 0; 0; 0.02; 0]^T$	$\bar{C}_{15}; \bar{C}_{25}; \bar{C}_{35}; \bar{C}_{45}; \bar{C}_{55}; \bar{C}_{65}$
6	$[0; 0; 0; 0; 0; 0.02]^T$	$\bar{C}_{16}; \bar{C}_{26}; \bar{C}_{36}; \bar{C}_{46}; \bar{C}_{56}; \bar{C}_{66}$

where V is the volume of the RVE, N is the total number of elements, $\boldsymbol{\sigma}_n$ and V_n are respectively the stress tensor at the center of an element n and the volume of this element. The effective strain tensor was deduced from the applied displacement and the effective tensor $\bar{\mathbf{C}}$ was computed. Convergence of the FE meshes was evaluated by studying the evolution of Young's moduli E_{11} and E_{22} as a function of the number of elements. Figure 4.20 is an example of the evolution of E_{11} and E_{22} as a function of the number of elements for the composite with room temperature properties. It can be seen that the meshes were sufficiently refined for both properties to converge.

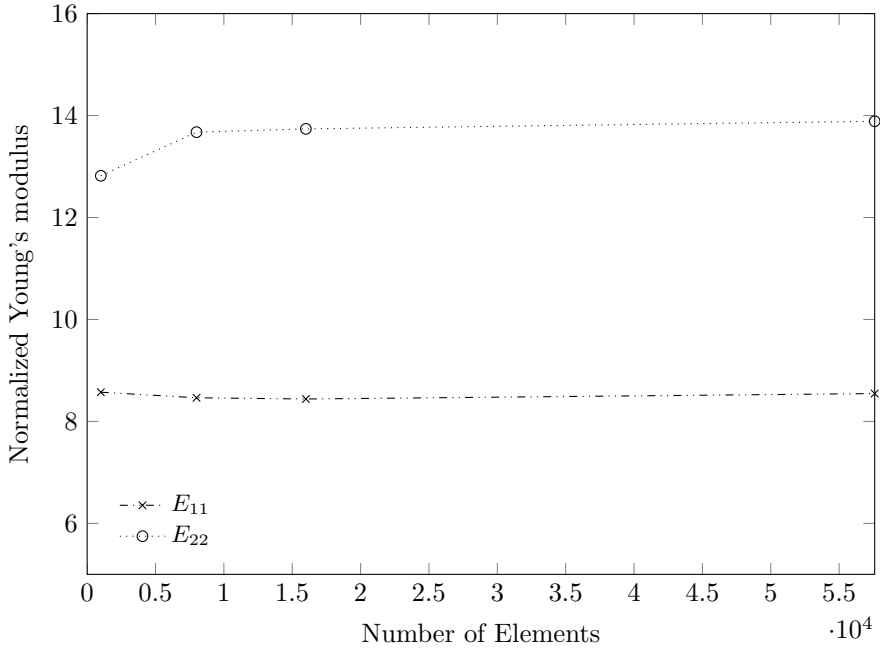

Figure 4.20 Convergence study for E_{11} and E_{22}.

Table 4.6 Comparison between analytical homogenization and experimental results at room temperature

	Experimental	Finite Elements (Error %)	Mori-Tanaka (Error %)	Rule of mixtures (Error %)
E_{11}/E_m	8.53	8.56 (0 %)	9.04 (6 %)	10.02 (17.5 %)
E_{22}/E_m	13.76	13.92 (1.3 %)	14.32 (4 %)	16.05 (16.7 %)

Table 4.7 Comparison between analytical homogenization and experimental results at wet-$T_g - 28°$C

	Experimental	Finite Elements (Error %)	Mori-Tanaka (Error %)	Rule of mixtures (Error %)
E_{11}/E_m	8.21	7.70 (6 %)	8.51 (3.5 %)	9.55 (16.4 %)
E_{22}/E_m	13.30	12.99 (2.5 %)	13.78 (3.6 %)	15.55 (16.8 %)

4.4.3 Validation of the theoretical predictions for the composite's effective properties

Tables 4.6 and 4.7 present the comparison between experimental results and analytical homogenization at room temperature and at wet-$T_g - 28°$C. The results show that the proposed methodology is clearly superior to the rule of mixture for predicting elastic properties, both at room and high temperature. Finite element homogenization results are the closest to the experimental data.

4.4.4 Local stress distribution analysis

One hypothesis explaining the differences between room temperature and high temperature damage mechanisms lies in the potential load redistribution at different temperatures. For a specific stress level, the stress distribution in each yarn section can be computed from the FE simulations or the analytical models. The stress tensor in the FE models can be provided at any desired location and coordinate system according to the following steps:

- The displacements were iteratively modified until an effective stress of 100MPa was reached in Directions 1 and 2, alternatively.
- The local fields were computed.
- A path passing through the center of each elliptical cross section was plotted.
- The local stress tensor, oriented along the local axes, were extracted along the path at each discrete ellipse center.

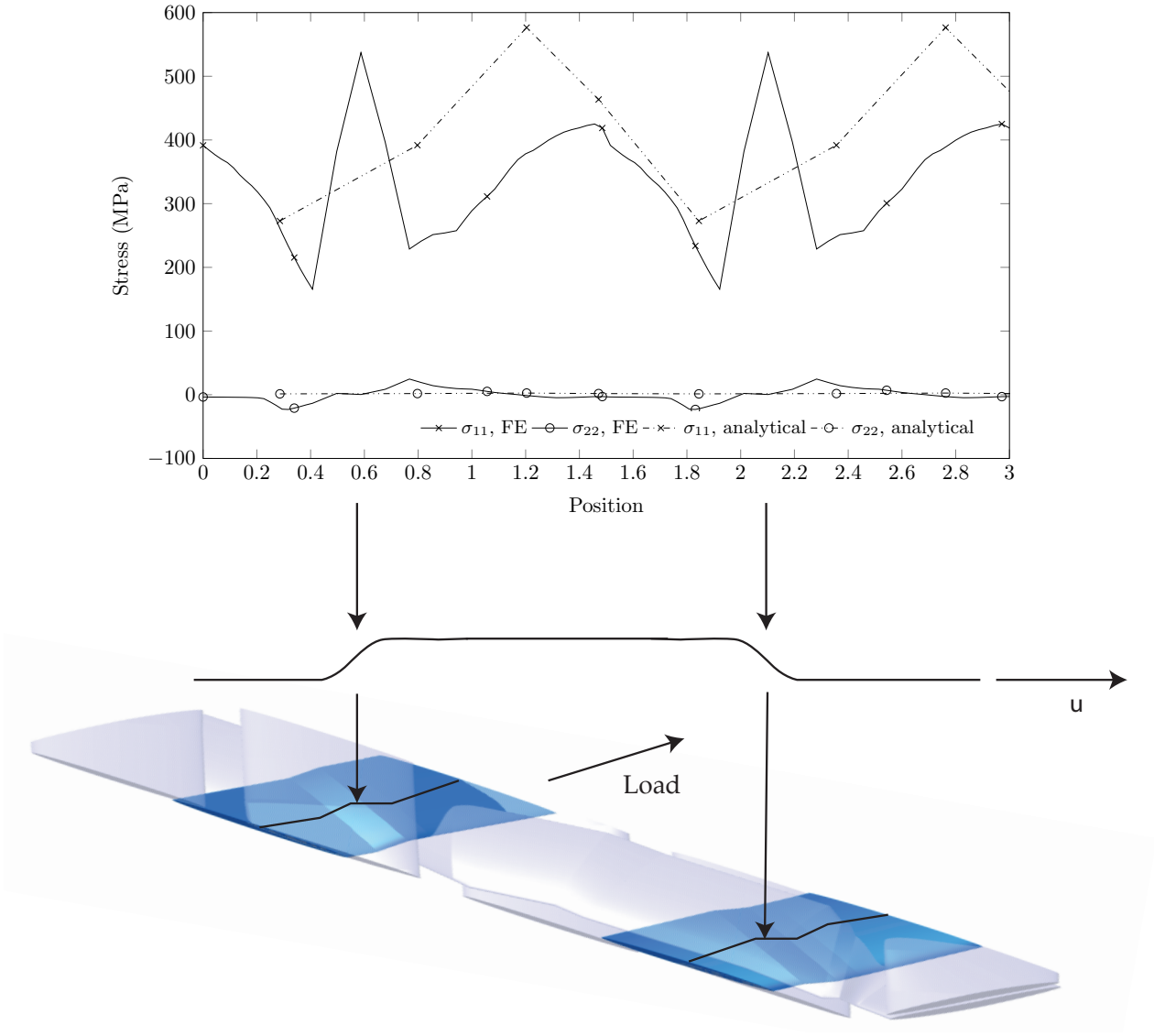

Figure 4.21 Stress distibution in the 0° yarns at room temperature for a specimen loaded in Direction 1 , obtained by finite element analysis and the Mori-Tanaka method.

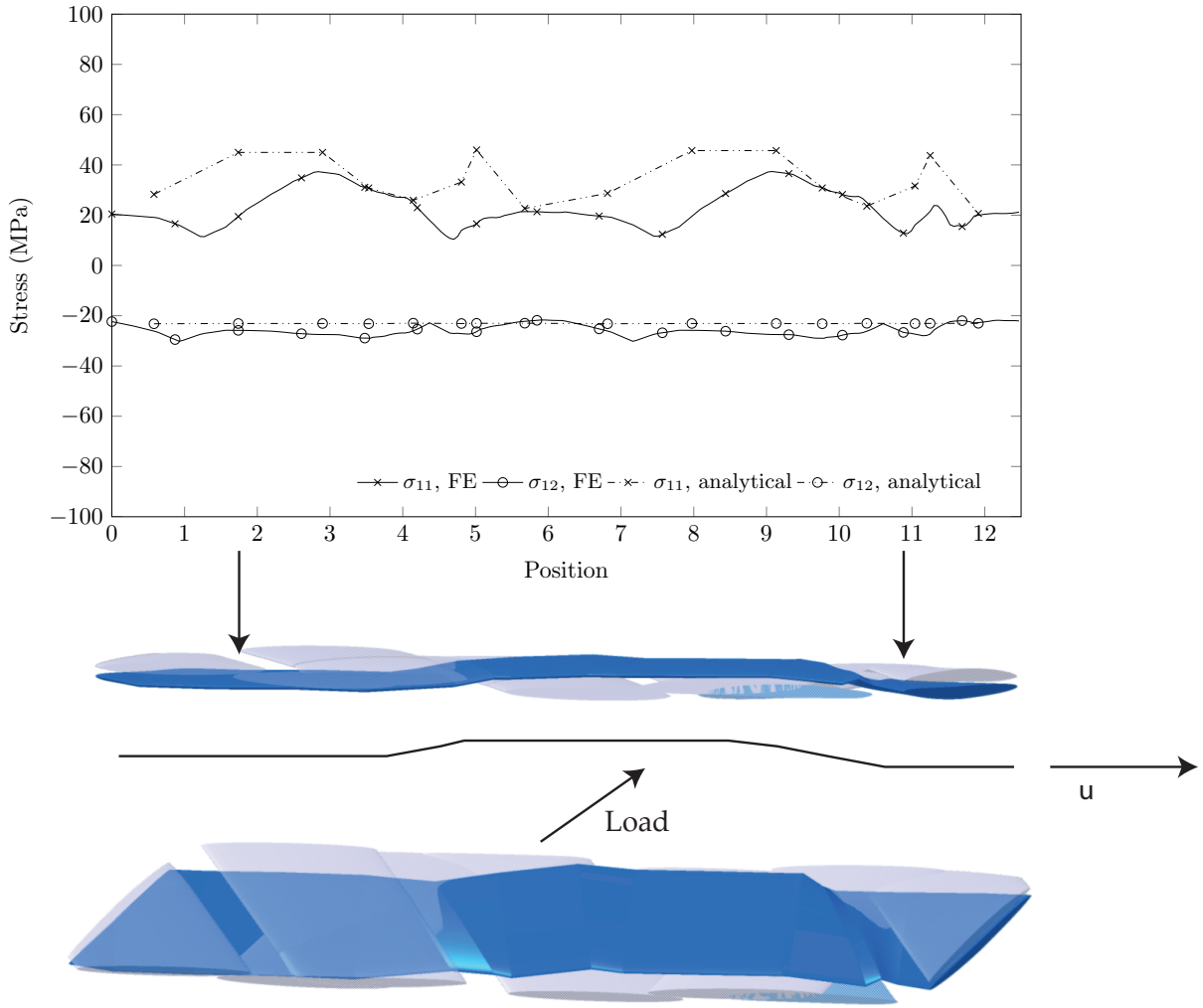

(a)60° yarn

Figure 4.22 Stress distibution in the 60° yarns at room temperature for a specimen loaded in Direction 1 , obtained by Finite Element (FE) analysis and the Mori-Tanaka method.

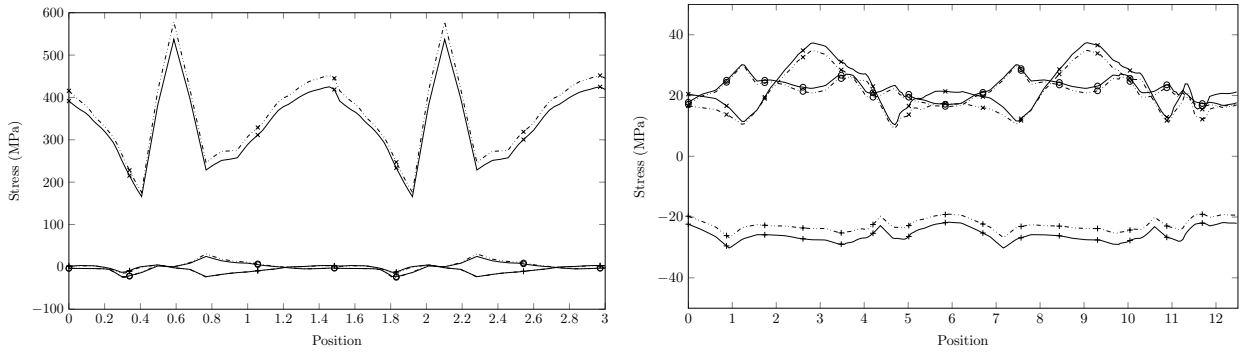

(a) 0° yarn (b) 60° yarn

σ_{11}, FE σ_{22}, FE σ_{12}, FE σ_{11}, HT σ_{22}, HT σ_{12}, HT

Figure 4.23 Stress distibution in the yarns computed from the FE model at different temperatures for a specimen loaded in Direction 1, obtained by FE analysis.

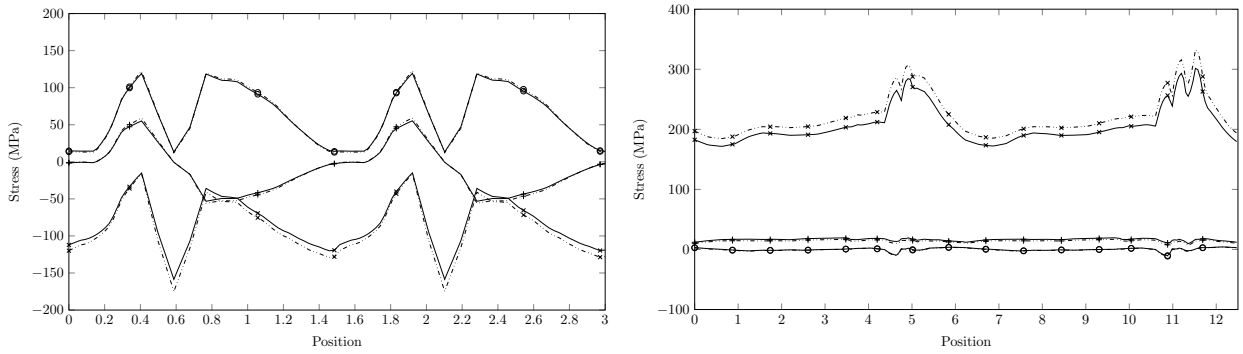

(a) 0° yarn (b) 60° yarn

σ_{11}, FE σ_{22}, FE σ_{12}, FE σ_{11}, HT σ_{22}, HT σ_{12}, HT

Figure 4.24 Stress distibution in the yarns computed from the FE model at different temperatures for a specimen loaded in Direction 2.

A similar methodology was adopted for the analytical part. The stress concentration tensor for each inclusion was computed to obtain the stress level applied to each yarn section, following the equation (Benveniste, 1987):

$$\boldsymbol{\sigma}_i = \mathbf{B}_{\mathrm{MT}} : \boldsymbol{\Sigma}_{applied} \tag{4.8a}$$

$$\mathbf{B}_{\mathrm{MT}} = \mathbf{W} : [\rho_0 \mathbf{I} + \rho_1 \mathbf{W}]^{-1} \tag{4.8b}$$

$$\mathbf{W} = \mathbf{C}_1 : \mathbf{T} : \mathbf{C}_0^{-1} \tag{4.8c}$$

where $\boldsymbol{\sigma}_i$ is the local spatially averaged stress in the inclusion i, $\boldsymbol{\Sigma}_{applied}$ is the macroscopic stress applied to the composite rotated to the local coordinate system of the yarn segment, and $\mathbf{B}_{\mathrm{MT}}$ is the stress localization tensor. Each inclusion had its own stress localization tensor, depending on its orientation and aspect ratios.
Figures 4.21 and 4.22 show the stress distribution inside the 0° and 60° yarns for an overall axial stress of 100 MPa in Direction 1. Most of the stress is borne by the 0° yarns which are are much more loaded than the 60° yarns. The 0° yarns are almost exclusively loaded in uniaxial tension, while the 60° yarn have an in-plane loading of uniaxial, transverse and shear stresses. Finally, the correlation between the analytical and the numerical stress distributions is acceptable, even if some of the stress peaks are not observed in the analytical simulation. This is most likely attributed to the fact the the analytical model does not take into account the specific surroundings of the inclusion.

Figure 4.23 shows the difference in the FE computed local stresses inside the 0° and 60° yarns loaded in Direction 1 at room temperature and at wet-T_g - 28°C. The average uniaxial stress in the 0° yarns increased by 5.7 % at wet-T_g - 28°C (for the same loading), which confirms the stress redistribution hypothesis. This increase in the stress corresponds to the 5.6 % drop in UTS in Direction 1 at wet-$T_g - 28$°C. Conversely, the loading level decrease for the 60° yarns, with the average σ_{11}, σ_{22} and σ_{12} stresses decreasing by 10.5%, 4.2% and 12.6% respectively. This observation partially explains the decrease of the crack density observed in the 60° yarns loaded in Direction 1 that can be seen in Figure 4.11.

Figure 4.24 shows the difference in the FE predicted local stresses inside the 0° and 60° yarns at room temperature and at wet-T_g - 28°C, for samples loaded in Direction 2. In this case, most of the stress is carried by the 60° yarns, which are mainly loaded in uniaxial stress, with a secondary load of shear stress. At wet-T_g - 28°C, the uniaxial stress increases by an average of 11 %, while the shear stress remains at the same level. This increase in the uniaxial

load explains the earlier cracking observed in Figure 4.17 with the 16% UTS deterioration for Direction 2 samples. In conclusion, the redistribution of stresses between the yarns explains most of the observed differences between room temperature and wet-T_g - 28°C.

4.5 Concluding remarks

The temperature effect on the tensile behavior of a triaxially braided composite was investigated in two different loading directions. The damage evolution was monitored and the results were explained with the help of analytical and numerical tools. It was observed that the yarn and matrix are stiffer at room temperature than at wet-T_g - 28°C, especially for the transverse and shear properties. These changes have negligible effects on the elastic properties of the composite in both directions. However, it created local stress redistributions at the yarn level, which in turn affected the composite's ultimate tensile strength of the composite. This evolution in the constituent elastic properties is reponsible for the changes in the stress profile at wet-T_g - 28°C in the yarns. The concentration of stress in specific yarns decreases the UTS of the composite and changes the damage profile during loading. The study also revealed the potential of quick and efficient analytical homogenization models to explain failure paths in textile composites.

4.6 Aknowledgements

The authors wish to aknowledge the financial support of the National Engineering Research Council (NSERC) of Canada, the Consortium for Research and Innovation in Aerospace in Quebec (CRIAQ), Rolls Royce Canada and Pratt and Whitney Canada. The first author also aknowledges additional funding in the form of a scholarship by NSERC. The authors acknowledge Drs Anna Scott and Mark Mavrogordato at the μ-VIS centre at the University of Southampton for provision of tomographic imaging facilities, supported by EPSRC grant EP-H01506X.

CHAPTER 5

ARTICLE 3: Anisotropic oxidation due to aging in a triaxially braided composite and its influence on tensile failure

A. El Mourid , Rajamohan Ganesan, Myriam Brochu, Thibaut Crochon and M. Lévesque.
Submitted to Composites Part B: Engineering on September 9th, 2014

Abstract

The service life of Polymer Matrix Composite Materials can be severely affected by long exposures to elevated temperatures. This study investigated the high temperature durability of a carbon/MVK10 triaxially braided textile composite. The goal was to monitor, analyze and quantify the evolution of physical and chemical aging processes to verify if Federal Aviation Administration (FAA) regulations for maximum service temperature ensure the safe use of such materials. Tensile tests were performed at the maximum service temperature on aged samples in two material directions to evaluate the progression of stiffness and Ultimate Tensile Strength (UTS) degradation. Aging induced damage was observed with the help of microscopic observations on the edges and cross-sections of tensile samples prior to loading. It was found that aging had a significant effect on UTS. It was also observed that the rate of deterioration was different for samples cut along different material directions, pointing towards anisotropic degradation mechanisms promoted by the braiding architecture. The investigated material had performances similar to existing high temperature composites, albeit at a lower temperature. It would therefore seem that FAA rules for setting the operating temperature are suitable for this material when aging effects are taken into consideration at the design stages.

keyword

Fabrics/textiles, High-temperature properties, Mechanical testing, Environmental degradation

5.1 Introduction

The durability of materials is of paramount importance for structural applications exposed to harsh environmental conditions, such as those encountered in a gas turbine

jet engine. Polymer Matrix Composite Materials (PMCM) are increasingly used in such applications where they are exposed to temperatures above 200°C, and to an oxidative environment, over long periods of time. Textile composites have already been successfully used in jet engine fan blade components and outer cores, and these advances could lead to higher temperature applications, once durability concerns are properly addressed.

Long exposures to elevated temperatures and to an oxidative environment can degrade the composite's matrix system due to aging (Leveque *et al.*, 2005), even without loading. This phenomenon, significantly decreasing the composite's strength, can be attributed to two separate mechanisms. First, physical aging is a material's volume relaxation due to rapid cooling below the glass transition temperature T_g. If the process is sufficiently fast, the material is momentarily out of its thermodynamic equilibrium and volume relaxation tends to bring it back to equilibrium. Physical aging affects both stiffness and density (Martin, 2008). Second, chemical aging is an irreversible degradation mechanism that mainly affects the matrix as well as fibre/matrix interfaces. It increases brittleness, creates surface cracks and decreases strength (Martin, 2008).

For many years, PMR-15 was the preferred matrix for high temperature structural applications, before one of its core components was found to be carcinogenic. Although new matrices were developed over the years, PMR-15 remains the standard against which the performances of new matrices are compared to. The effect of aging on PMR-15 was studied by several authors, for different material architectures and temperatures. For example, Nelson (1984) studied the decrease in short beam shear (SBS) strength at room temperature for celion/PMR-15 composites, for different aging times and temperatures. His results revealed that the composite strength remained constant for up to 5000 h of aging and abruptly decreased after that threshold. Degradation occurred in a thin surface layer whose thickness increased with aging time. Aging was also studied by Leveque *et al.* (2005) for carbon/epoxy $[\pm 45°]_{4s}$ unidirectional laminates. The authors assumed that fibre aging could be neglected for temperatures below 250°C. The authors performed tensile and creep tests and reported a decrease in tensile strength due to aging. The strength deterioration was explained by an increase in the matrix' brittleness, which was a consequence of the formation of a thermo-oxidative layer on the specimens' surfaces. Stress concentrations caused by the thermo-oxidative process, combined with the stress fields caused by the mismatch between Coefficients of Thermal Expansion (CTEs) of the matrix and fibres, could be the reason for the formation of surface cracks. Similar observations were made by Lowe *et al.* (2002) who studied the influence of aging on carbon/BMI composites (T_g of 302°C) properties over an aging period of 7 months at 204°C and 250°C. They observed an initial increase in the composites' fracture toughness, followed by a significant decrease as aging time increased.

They attributed the initial increase in toughness to a post-cure that increased cross-linking within the polymer. Once this process was completed, thermal oxidation became prominent and consequently decreased the composites' toughness.

The influence of the fibres' presence on the thermal oxidation process was studied by several authors (Pochiraju and Tandon, 2009; Tandon *et al.*, 2006; Schoeppner *et al.*, 2007; Tandon *et al.*, 2008). These authors experimentally measured the oxidizing layer thickness for isothermal aging with the help of dark-field microscopy and provided models to estimate the layer growth on unidirectional carbon/PMR15 laminates. Tandon *et al.* (2008) specifically investigated the anisotropic oxidative process in unidirectional polymer matrix composites. They observed that the oxidation layer thickness growth rate was higher along the fiber length than in the transverse direction. This oxidation resulted in fibre/matrix debonding and in the apparition of matrix cracks. It was concluded that the presence of fibres could increase the oxidized layer growth rate, which points to a possible anisotropic Ultimate Tensile Strength (UTS) degradation.

Maverick's MVK-10 polyimide matrix has been developed as a replacement for PMR-15. Moreover, gas turbine jet engines niche applications require braided textile composites exposed to relatively high temperatures (above 200°C). The Material Qualification and Equivalency for Polymer Matrix Composite Material Systems document, developed by the Federal Aviation Administration (FAA, 2001) specifies the maximum service temperature at which PMCM can be used as 28°C below the fully water saturated glass transition temperature (wet-$T_g - 28°C$). Since very little is known about this particular matrix, as well as thermo-oxidative damage development in braided composites, it would be of considerable interest to verify if FAA regulations ensure the safe use of such materials.
The objectives of this study were therefore:

- To monitor, analyze and quantify the evolution of physical and chemical aging processes at service temperature, defined as wet-T_g - 28°C.
- To test up to failure and monitor damage evolution, in composite coupons cut along two different material directions and exposed to a range of aging times.

The experimental methodology is presented in Section 2. The experimental results are presented in Section 3. The paper ends with a discussion and a summary of the findings.

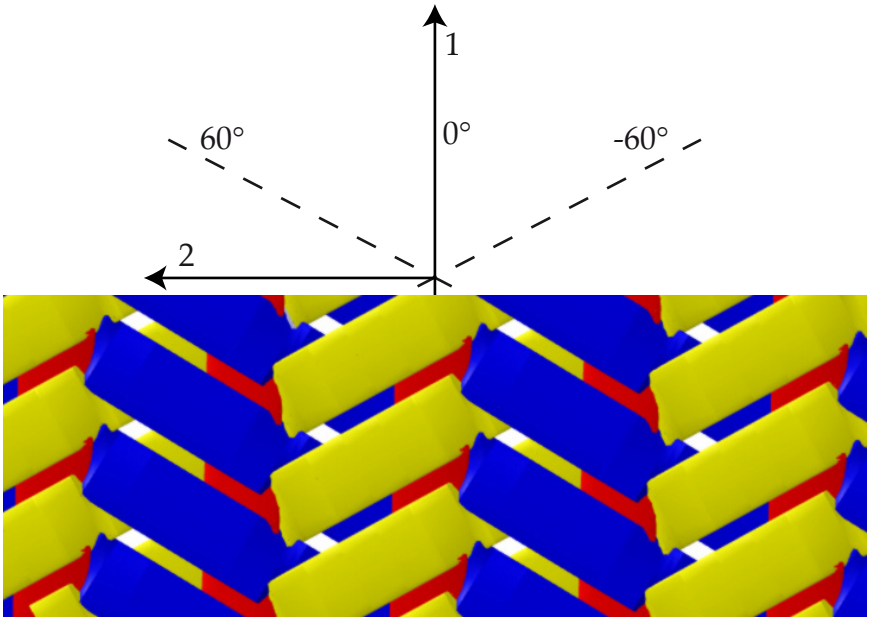

Figure 5.1 Representation of the triaxially braided architecture

5.2 Experimental methodology

5.2.1 Materials

The studied composite was a tri-axially braided preform infused by Resin Transfer Moulding (RTM) with Maverick's MVK10 high temperature polyimide resin. The preforms were fabricated by tri-axially braiding multiple plies of Cytec T650-35 6K dry carbon fibres on a tubular mandrel at $0/\pm 60°$ ($\pm 3°$). Two panels of 342.9mm $\times$ 381mm $\times$ 3mm were manufactured. The fibre volume fraction was evaluated to be 56% from acid digestion tests. Figure 5.1 displays the architecture of the braided composite. The red yarns are the 0° yarns aligned along Direction 1, while the yellow and blue yarns are the $\pm 60°$ yarns. Two MVK10 matrix panels of 315.5mm $\times$ 381mm $\times$ 5.2mm were manufactured by resin transfer molding and cured slightly above their T_g.

5.2.2 Raw samples preparation

Several samples were cut from the matrix and composite panels to evaluate the physical and chemical aging processes. Straight samples of 165mm $\times$ 25.4mm $\times$ 3mm, shown in Figure 5.2a, were water jet cut from the composite panels in 2 directions: Direction 1 samples were cut along the 0° yarns, while Direction 2 samples were cut at 90° from Direction 1.

Table 5.1 Summary of the samples used to evaluate the physical and chemical aging processes.

Material	Quantity	Test	Dimensions	Figure
Composite	24	Tensile	165 mm × 25.4 mm × 3mm	5.2a
Matrix	12	Tensile	320 mm × 19.04 mm × 6.35mm	5.2b
Composite	8	Cross-section	12.5mm × 25mm × 3mm	5.2c
Composite	2	Mass	25mm × 10mm × 3mm	5.3a
Matrix	3	Mass	25mm × 10mm × 5.2mm	5.3b
Matrix	3	T_g	60mm × 12.7mm × 3.2mm	5.3c

Micro-tomographic observations (El Mourid *et al.*, 2014) revealed that 80% of the yarns were aligned at ±60° from the 0° yarns, which caused the composite to be stiffer and tougher when tensile tested along Direction 2. The ratio of specimen width to unit cell width was 2.24:1, in accordance with ASTM D6856 standard. 15 samples cut in Direction 1 were aged at wet-T_g - 28°C for periods of 1, 4, 9, 12 and 17 months and tensile tested. Only 9 samples cut in Direction 2 were aged at wet-T_g - 28° for 1, 4, and 9 months, due to the limited quantity of material available, and were subsequently tested. Tensile test matrix coupons whose dimensions are in accordance with ASTM D638 were also water jet cut and are shown in Figure 5.2b. Three neat resin and two composite samples of size 25mm × 10mm × 3mm, cut from the panels with a diamond wafering saw and used for the mass loss and volume change determination during aging, can be seen in Figure 5.3a. Small samples of size 12.5mm × 25mm × 3mm were cut from the aged composite samples with a diamond wafering saw, for every aging time and before testing, to monitor aging damage progression before loading. Figure 5.3c shows these samples. Table 5.1 lists all the samples manufactured and tested in this work.

5.2.3 Glass transition temperature

MVK10 dry-glass transition temperature was provided by the manufacturer and was above 300°C. The wet-T_g was determined using a Dynamic Mechanical Analyzer (DMA) TA Q800 from TA Instruments and according to ASTM D-7028 standard by Crochon *et al.* (2014). The samples (Figure 5.3c) cut with a diamond wafering saw from neat resin panels were fully saturated with water in an environmental chamber before being cyclicly loaded at a frequency of 1Hz. The wet-T_g was defined as the intersection of the two slopes associated with the storage modulus E' for the glassy and rubbery states. The testing temperature was determined according to FAA regulations as wet-$T_g - 28$°C, which was well above 200°C.

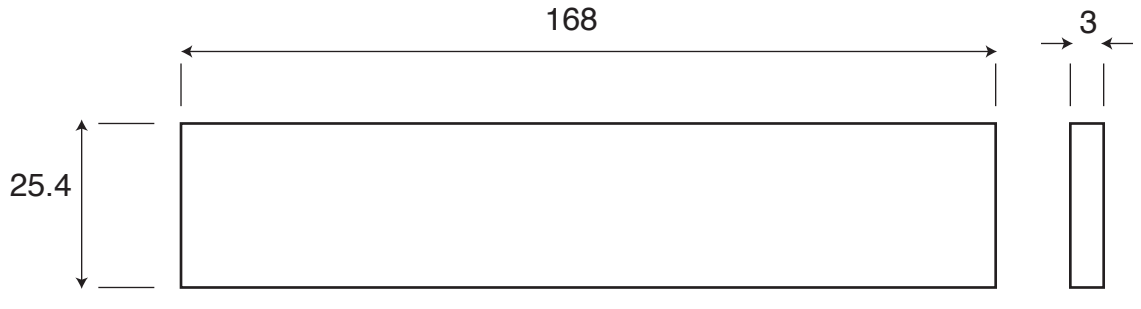

(a) Tensile testing composite sample

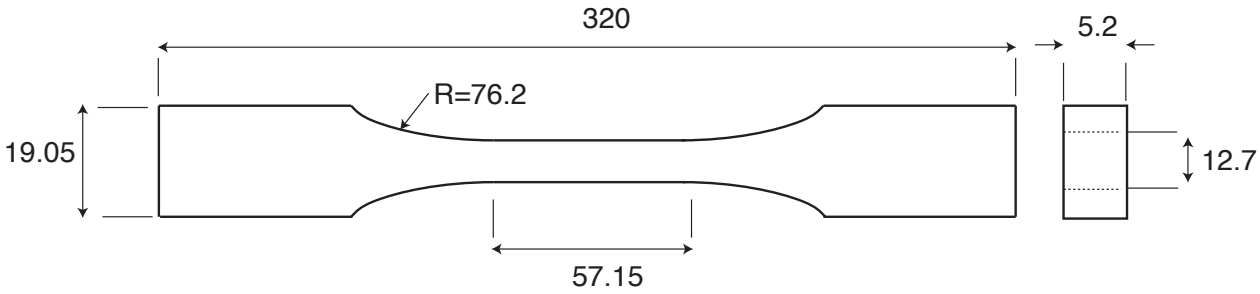

(b) Matrix testing sample

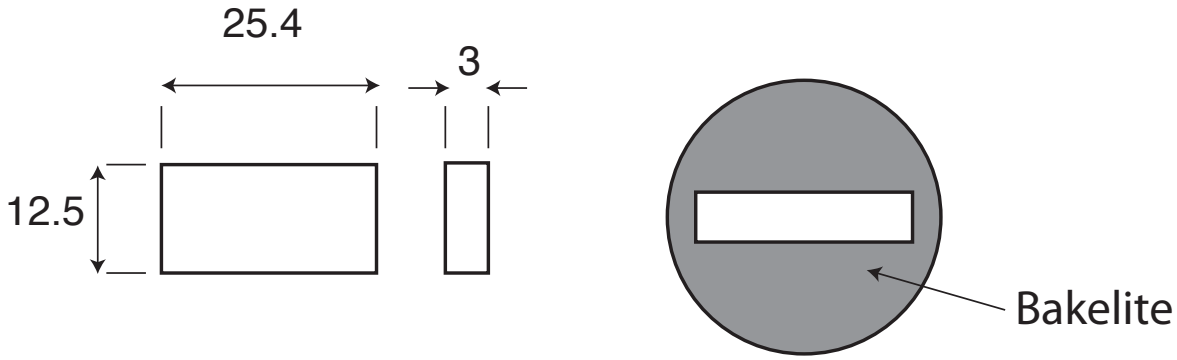

(c) Composite samples for microscopic observations

Figure 5.2 Dimensions in mm for all samples used to determine the aging parameters.

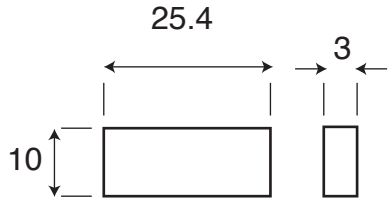

(a) Composite samples for volume and mass measurement as a function of aging

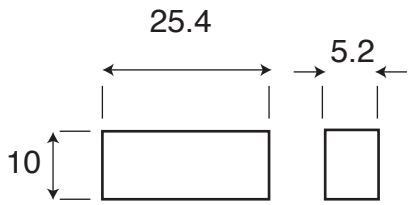

(b) Matrix samples for volume and mass measurement as a function of aging

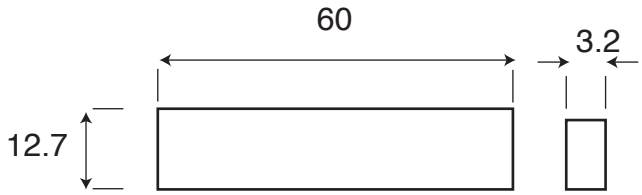

(c) Matrix sample for T_g determination

Figure 5.3 Dimensions in mm for all samples used to determine the aging parameters.

Table 5.2 Number of aged composite samples cut along Directions 1 and 2.

Number of samples	1 month	4 months	9 months	12 months	17 Months
Direction 1	3	3	3	3	3
Direction 2	3	3	3	0	0
Matrix	3	3	3	0	3

5.2.4 Aging procedure

Composite and matrix samples (Figures 5.2a and 5.2b) were aged after being cut to observe the oxidation process on the samples edges. Table 5.2 shows the number of samples aged for each duration. The cut samples were aged at wet-T_g - 28°C in a Thermo Scientific Precision 625 High Performance oven, which complies with industry standards such as ASTM E145 type IIA and UL746B. Four thermocouples with a data acquisition system were used to monitor temperature during the aging process in accordance with ASTM D3045 for heat aging of plastics. The oven's temperature uniformity was within 1% of the difference between room and aging temperature. All the samples were aged simultaneously and the aging temperature dropped by 4°C for very short periods when the oven was opened to take the samples out. The samples cross-sections dimensions were measured before and after aging but their masses were not recorded.

5.2.5 Tensile testing setup and procedures

The aged samples were tensile tested at service temperature up to failure in accordance with ASTM D3039 standard. The samples were loaded in an MTS Insight 50kN electromechanical load frame equipped with MTS advantage wedge action grips. The samples were heated inside a forced convection Lab-Temp LBO-series box environmental chamber from Thermcraft Incorporated. The environmental chamber allowed for testing at temperatures up to 425°C with a maximum heating rate of $10°C \cdot min^{-1}$.

The temperature was measured with thermocouples away from the specimen, on the specimen's surface as well as on the load cell (to monitor and prevent any overheating). The temperature was manually set on the environmental chamber's controller so as to reach the testing temperature on the specimen's gage length. Strains were measured with Vishay high temperature WK-06-500BH-350 strain gages. The strain gages were bonded with Vishay M-Bond 610 Adhesive and 330-FJT high temperatures wires were used to collect data for the composite samples. A high temperature uncooled Epsilon 3555 extensometer was used to measure strains for the matrix samples

5.2.6 Identification of aging mechanisms

Physical and chemical aging usually lead to volume contraction and mass reduction. Three neat resin and two composite samples (Figures 5.3a and 5.3b) were aged inside the oven. Their masses were regularly measured with a Sartorius CPA124S scale with ±0.1mg error. Volume contraction was periodically evaluated with a Mutitoyo caliper by measuring the samples' widths and thicknesses.
Damage evolution was characterized through tensile specimens edges and cross-sections microscopic observations. The tensile composite samples were polished manually with SiC papers of 120, 240, 400, 600 grit, in that sequence. Diamond suspensions of $6\mu m$, $3\mu m$ and $1\mu m$, in that order, were subsequently used to obtain a mirror polish and an alumina suspension of $0.05\mu m$ was used to provide a final polish and remove the last imperfections. In the sequel, 'edge cracks' refer to cracks initiating on the left or right edge while 'surface cracks' refer to those initiating on the top or bottom, as schematically illustrated in Figure 5.4. Figure 5.5a depicts the edge of an unaged Direction 1 specimen. On this edge, 0° yarns appear as long strands while ±60° yarns appear as ellipses. Figure 5.5b displays the edge of an unaged Direction 2 specimen. On this edge, 0° yarns appear as ellipses while ±60° yarns appear as curved strands. The cross-section samples (Figure 5.2c) were mounted in Bakelite coating, polished according to the procedure described for the edge observations and

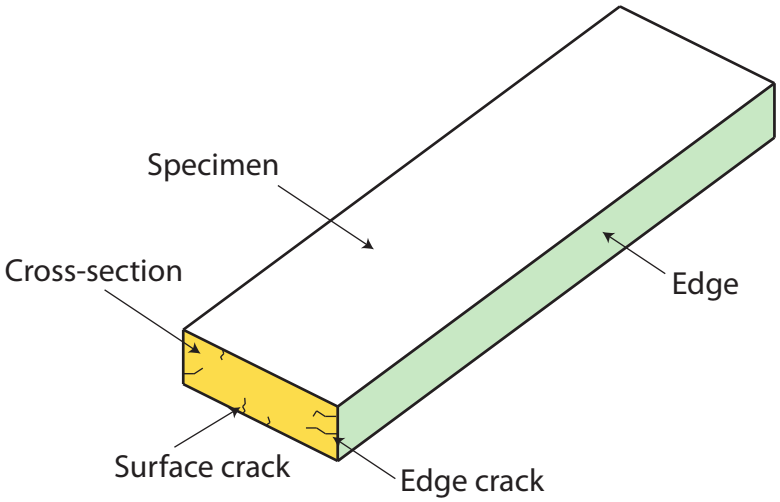

Figure 5.4 Localization of surface and edge cracks on a cross-section of a sample

observed under a Leitz Metallovert inverted microscope, at a 50X magnification.

A long distance microscope system was used to monitor initial cracks and damage evolution on the specimens during tensile testing. The system consisted of a model K2 Distamax long distance microscope system equipped with a PCO camera to record the images. The microscope was mounted on a Manfrotto MT057C3-G tripod and controlled by a 3 stepping motors drive SGSP stage and a shot-304GS 4-axis stage controller. The 3 stepping motors were used to control the microscope's position and focus. The maximum resolution was limited by the distance between the lens and the specimen, which was dictated by the presence of the environmental chamber, and was 17cm. At this distance, the resolution was 1.9μm/pixel and corresponded to a magnification of 20X. The microscope was also used to determine the original crack density in the specimen due to chemical aging, before loading at the testing temperature. Figure 5.6 shows pictures of Direction 1 and 2 sample edges observed by the long distance microscope system. In this figure, and the first subfigure in each group of figures, the 0° yarns are circled by solid lines while the matrix rich zones are circled by dashed lines. The ±60° yarns are not circled.

5.3 Experimental results

The results for tensile tests on unaged specimens were reported in a previous paper (El Mourid *et al.*, 2014) and are recalled in Table 5.3. Note that the properties were normalized by those of the matrix at room temperature for confidentiality reasons. E_m, σ_m^u and ε_m^u refer to the matrix Young's modulus, ultimate tensile strength and tensile strain at room

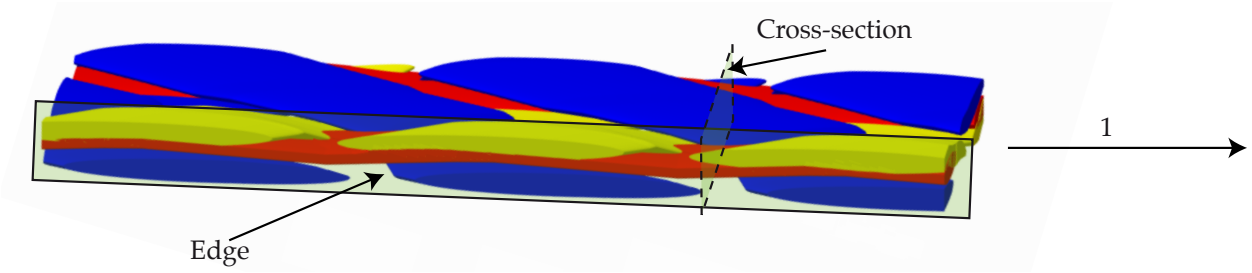

(a) Observation planes on Direction 1 samples

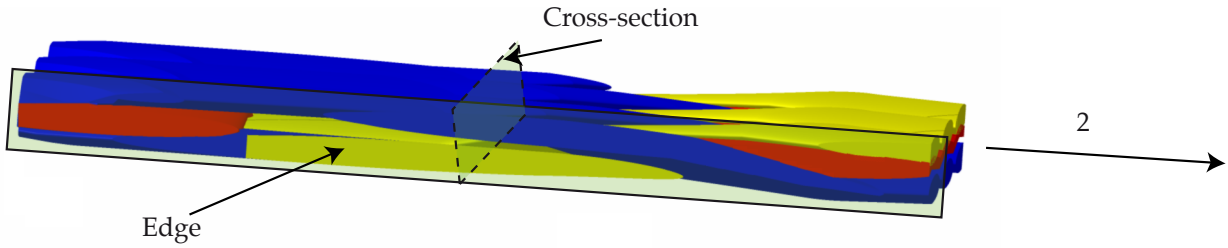

(b) Observation planes on Direction 2 samples

Figure 5.5 Observation planes on a) Direction 1 and b) Direction 2 samples.

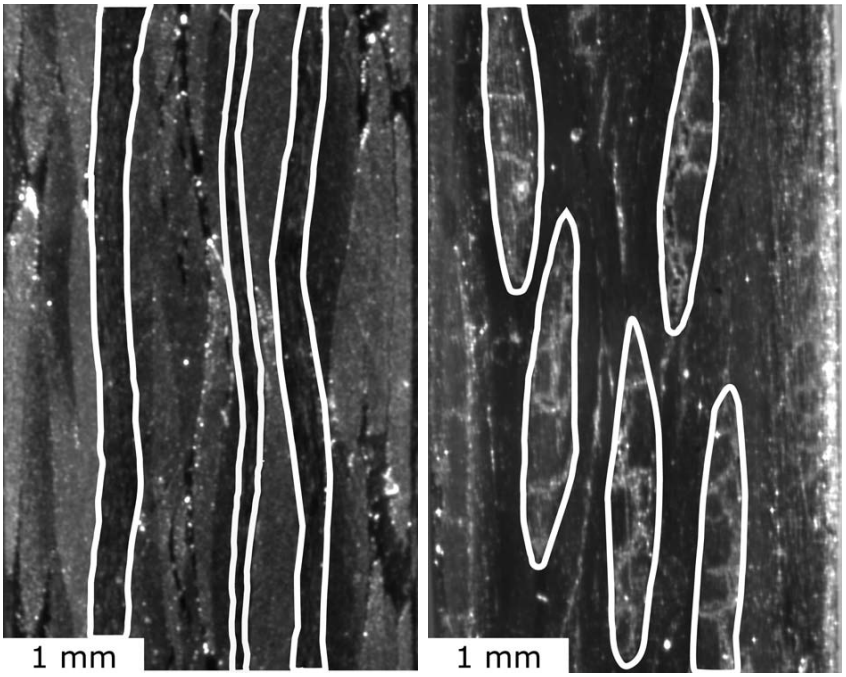

(a) Direction1 (b) Direction 2

Figure 5.6 Edges of 2 samples aged for 4 months observed by the long distance microscope. The 0° yarns are circled by a solid white line.

Table 5.3 Tensile properties of the matrix and composite at room temperature (RT) and at wet-T_g - 28°C (El Mourid *et al.*, 2014).

	E/E_m	$\sigma u/\sigma_m^u$	$\varepsilon^u/\varepsilon_m^u$
Matrix (RT)	1	1	1
Matrix (wet-T_g - 28°C)	0.75	0.47	0.62
Direction 1(RT)	8.83	9.1	0.99
Direction 1(wet-T_g - 28°C)	8.21	8.88	0.90
Direction 2 (RT)	13.8	11.8	0.88
Direction 2 (wet-T_g - 28°C)	13.3	10.4	0.78

temperature. E, σ^u and ε^u refer respetively to the material's Young's modulus, UTS and tensile strain.

5.3.1 Physical aging

Figure 5.7 reports the mass diminution and volume contraction for matrix and composite samples as a function of the aging time at wet-T_g - 28°C. The figure shows that matrix samples suffered almost identical volume and mass reductions due to aging. Considering that MVK-10 has a density ranging from 1.05 to 1.10 g/mL, the observed volume loss is mostly due to the mass loss induced by chemical aging. The composite's mass loss was higher than the matrix' mass loss, pointing to the catalytic effect of the fibres on the chemical aging process. No significant volume change was observed in the composite. Figure 5.8 shows the retention of E_{11} and E_{22} with respect to the initial value for the composite, as well as E for the neat resin, as a function of the aging time. Appendix B provides additional statistical information about all tested samples. It can be seen that the composite's properties remained constant over time, with a slight decrease after 9 months of aging. From this data, it can be concluded that physical aging did not have a meaningful impact on the composite's stiffness and density at wet-T_g - 28°C.

5.3.2 Chemical aging

Tensile tests on aged composite specimens

Tensile tests were performed on unaged Direction 1 and 2 samples, at room temperature and at wet-T_g - 28°C. The results for unaged samples are summarized in Table 5.3. Figure 5.9 shows the UTS retention for aged specimens tested at wet-T_g - 28°C (the data was normalized by the UTS for unaged specimens tested at the same temperature). The figure shows that all samples exhibited a continuous degradation rate starting at 4 months of aging. It is also

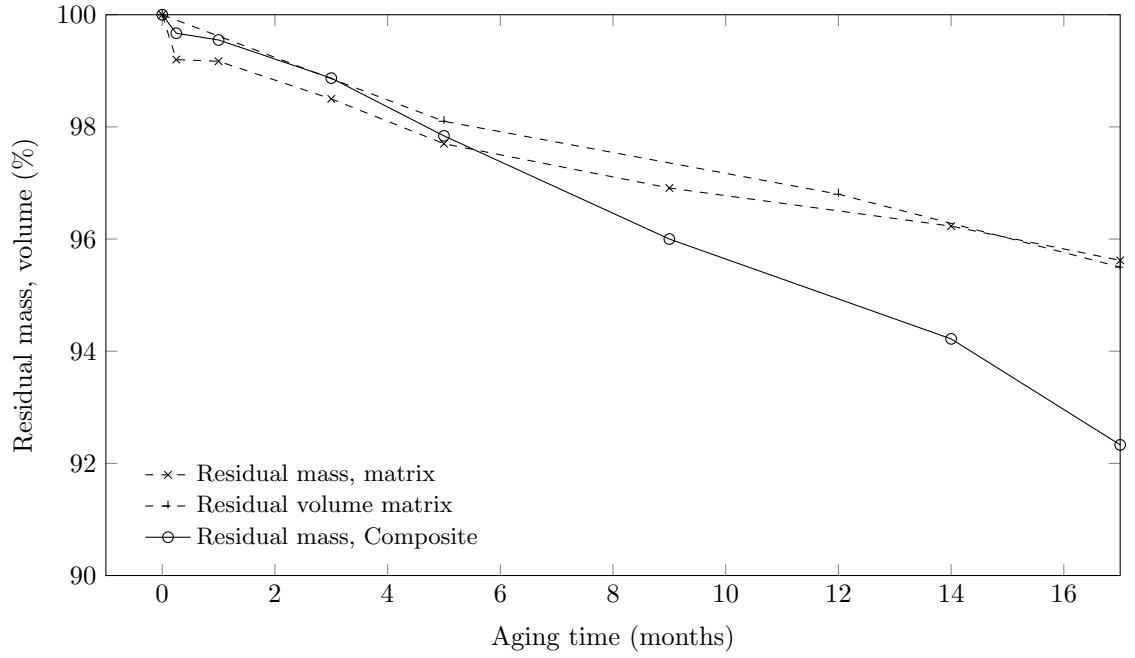

Figure 5.7 Residual mass and volume of matrix and composite samples as a function of aging time at wet-T_g - 28°C.

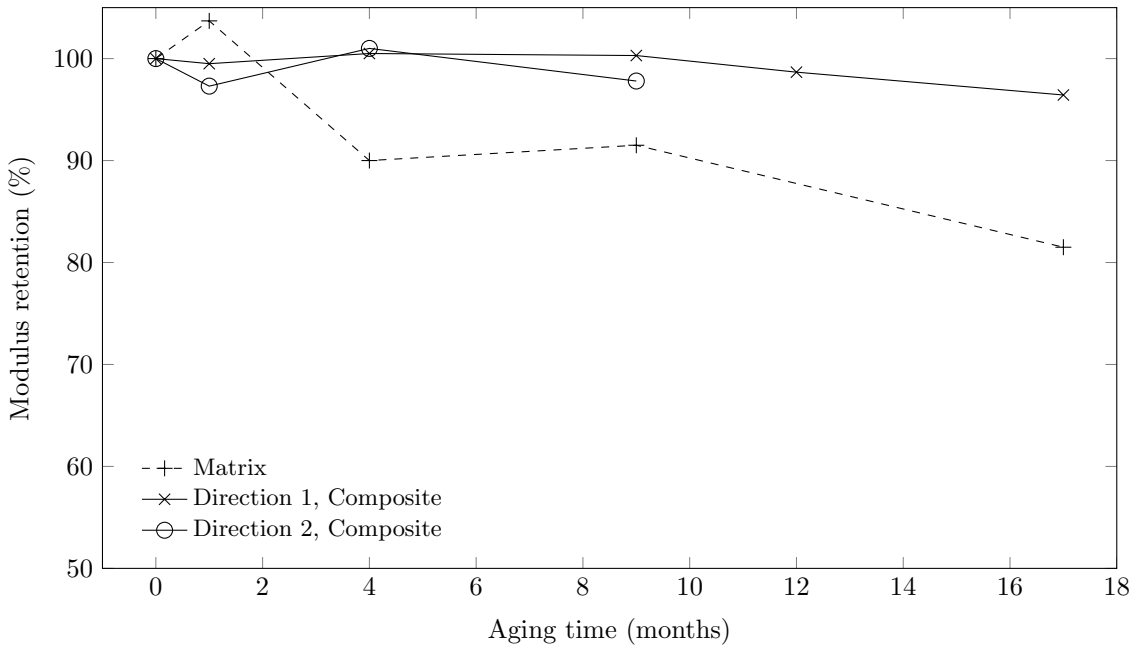

Figure 5.8 Young's modulus evolution for the composite and the matrix as a function of aging time at wet-T_g - 28°C.

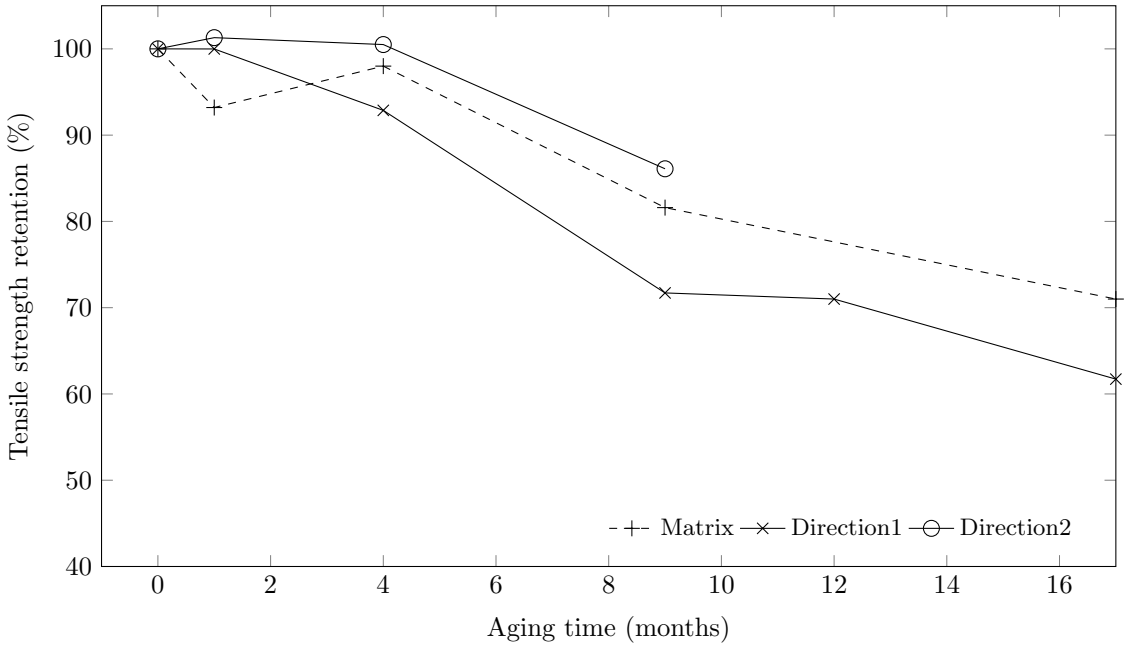

Figure 5.9 Strength retention of composite and matrix samples as a function of aging time at wet-T_g - 28°C.

interesting to note that, in overall, Direction 2 samples were less affected than the matrix and that Direction 1 samples suffered a more important strength degration than the matrix. Figures 5.10 and 5.11 show failed Direction 1 and 2 samples. It can be seen that as aging time increases, samples surfaces became darker and mat, and that the yarns were more visible. Direction 1 samples failed along the ±60° yarns, independently of aging times. Direction 2 samples failed along the ±60° yarns for up to 4 months of aging, while 9 months of aging led to failures along the 0° yarns.

Microscopic observations

Figure 5.12 shows Direction 1 samples' edges for different aging times (prior to loading). The figure shows that 0° yarns appear as long straight strands while the ±60° yarns appear as curved ellipsoids. Small transverse intra-yarn matrix cracks appeared progressively on the ±60° yarns after 1 month of aging. Cracks propagated in the ±60° yarns and triggered superficial debonding and longitudinal cracks after 4 months of aging. Extensive damage, consisting of a network of cracks and yarn debonding over the whole specimen's thickness, can be observed after 12 months of aging.

The stress-strain curves (not reported here) revealed that both Direction 1 and 2 samples exhibited a brittle behavior for every aging time at wet-T_g - 28°C. Besides the initial damage

(a) 1 month

(b) 4 months

(c) 9 months

(d) 12 months

(e) 17 months

Figure 5.10 Failed Direction 1 samples after a) 1, b) 4, c) 9, d) 12 and e) 17 months of aging at wet-T_g - 28°C.

(a) 1 month

(b) 4 months

(c) 9 months

Figure 5.11 Failed Direction 2 samples after a) 1, b) 4 and c) 9 months of aging at wet-T_g - 28°C.

induced by aging, very little additionnal damage was observed on the edges during the tensile tests, suggesting that the crack saturation was already reached in that area. Figure 5.13 shows the edge of a Direction 1 sample aged for 12 months under different load levels. It can be seen that the crack density remained constant up to 98% of UTS. At 98% of UTS, one of the debonding zone on the right of the specimen started spreading rapidly and caused failure. Figure 5.14 shows the edge of a Direction 2 sample aged for 4 months under different load levels. It can be seen that the crack density at the surface remained constant up to 94% of UTS. At 94% of UTS, one of the longitudinal cracks on a 0° yarn ran deeper into the material and yarn debondings increased until failure.

Figure 5.15 shows the edges of Direction 2 samples for different aging times. Transverse cracks initiated first in the 0° yarns and their density was higher than in the other yarns. Edge observation of samples aged for 9 months reveals that the crack network was more important than for 4 months and expanded to the ±60° yarns that were adjacent to 0° yarns, which explains the decrease in UTS.

Figure 5.16 shows Direction 1 samples' cross-sections after 12 months of aging. It can be seen that the cracks are concentrated on the top and the bottom layers of the composite. However, the centre of the specimen was undamaged. These observations further confirm that chemical aging was the main reason behind the drop in UTS since damage was concentrated on the surfaces that were in contact with air, where the thermo-oxidative process could occur. Figure 5.17 displays Direction 2 composite samples cross-sections after 4 months and 9 months of aging. After 4 months, the 0° yarns on the edge are already cracked internally. However, the top and the bottom surface are still undamaged. These observations confirm the catalytic effect of the presence of the fibres at the surface. After 9 months, the intrayarn damage has spread to the ±60° yarns and transverse cracks initiated from all the surfaces (top, bottom and edges).

5.4 Discussion

The damage mechanisms caused by aging without any loading were similar in nature to those observed during the tensile testing of unaged specimens (El Mourid *et al.*, 2014). Figure 5.18 shows the difference in edges crack density between unaged specimens after loading at room temperature and wet-T_g - 28°C, and an aged Direction 1 specimen without any loading for different aging times. It can be seen that the crack density caused by aging is much higher than the crack density caused by the loading of unaged specimens, especially after 1 month of aging. For that reason, crack saturation on the edges of samples aged for more

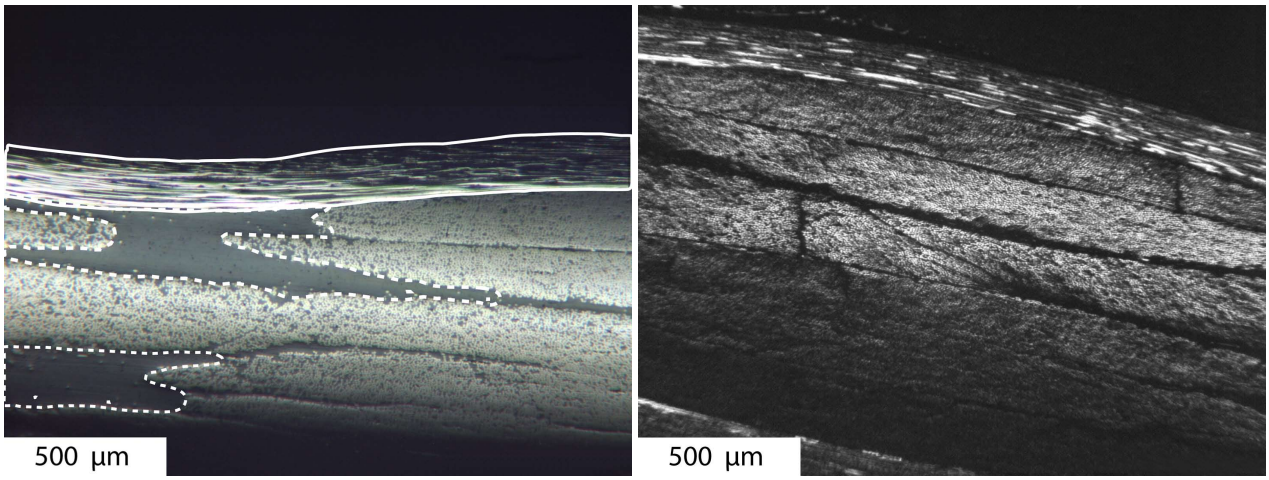

(a) Unaged

(b) 1 month

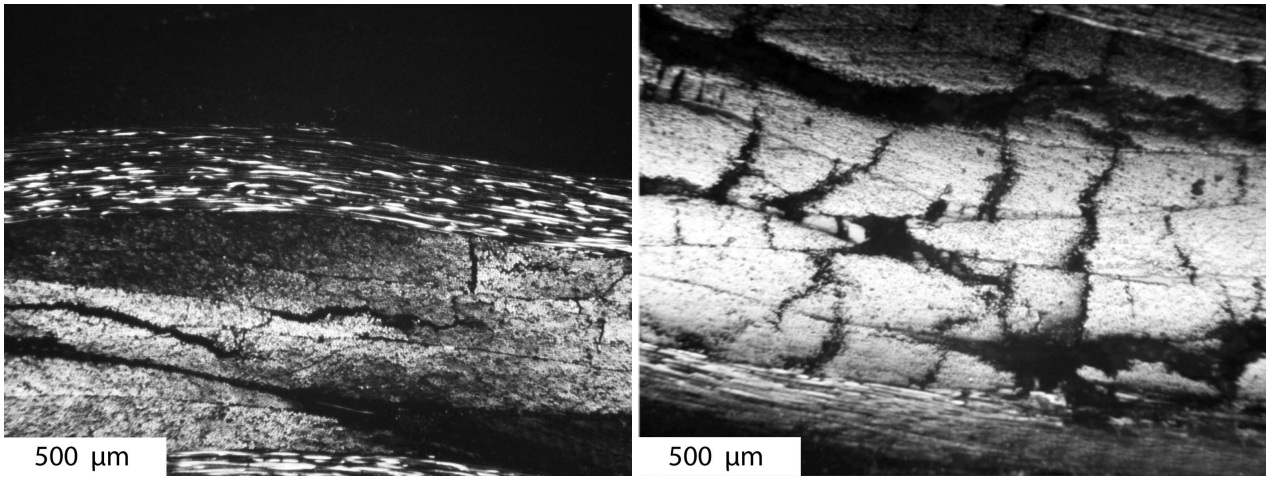

(c) 4 months

(d) 12 months

Figure 5.12 Observation of Direction 1 specimens edges for different aging times at wet-T_g - 28°C. The 0° yarns are circled by a solid line while the matrix riche zones are circled by a dashed line. The ±60° are not circled.

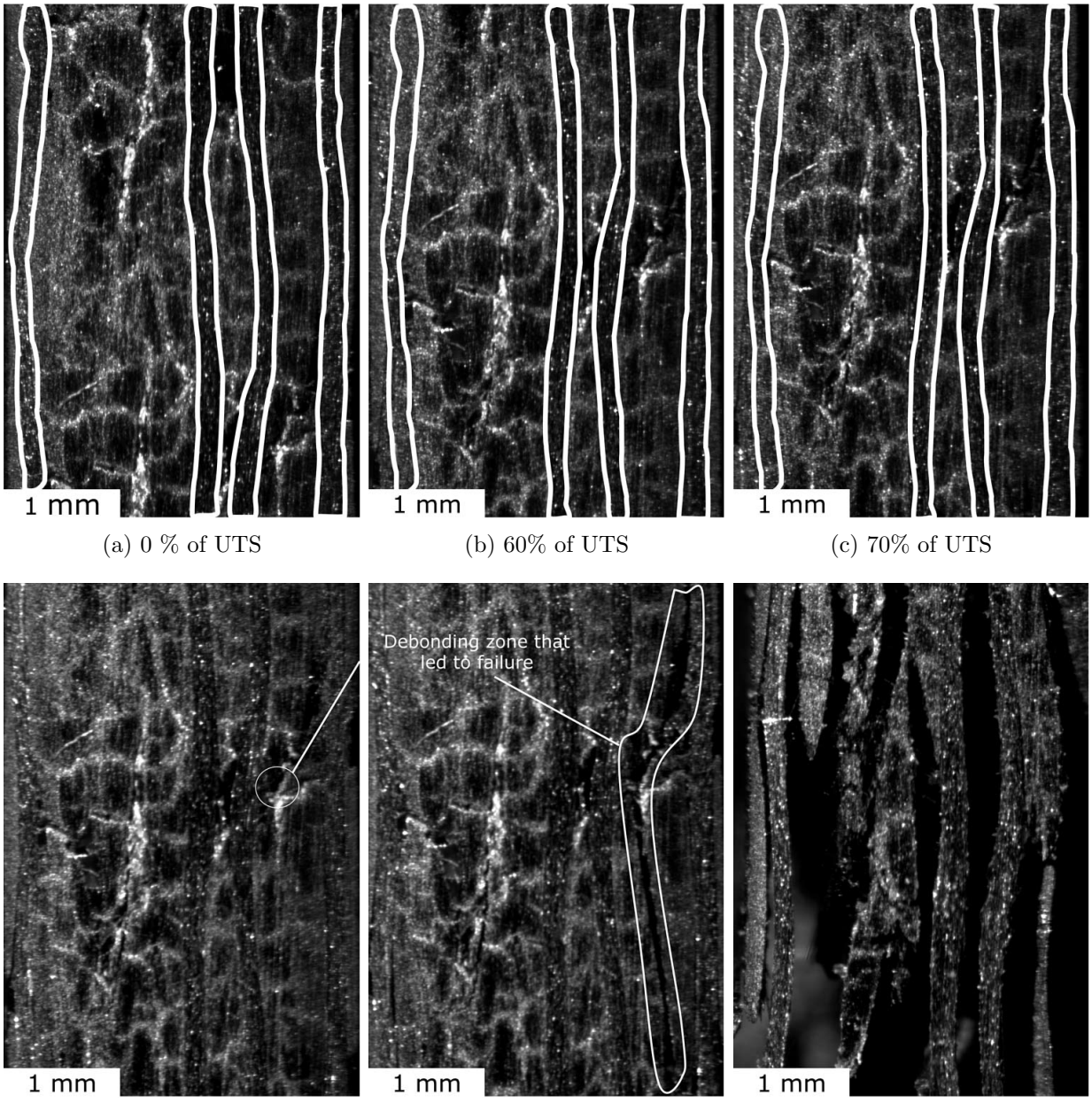

(a) 0 % of UTS (b) 60% of UTS (c) 70% of UTS

(d) 98% of UTS (e) 99% of UTS (f) 100% of UTS

Figure 5.13 Direction 1 sample aged for 1 year observed by the long distance microscope under different load levels at Wet-T_g - 28°C: a) 0%, b) 60%, c) 70%, d) 98%, e) 99% and f) 100% of UTS.

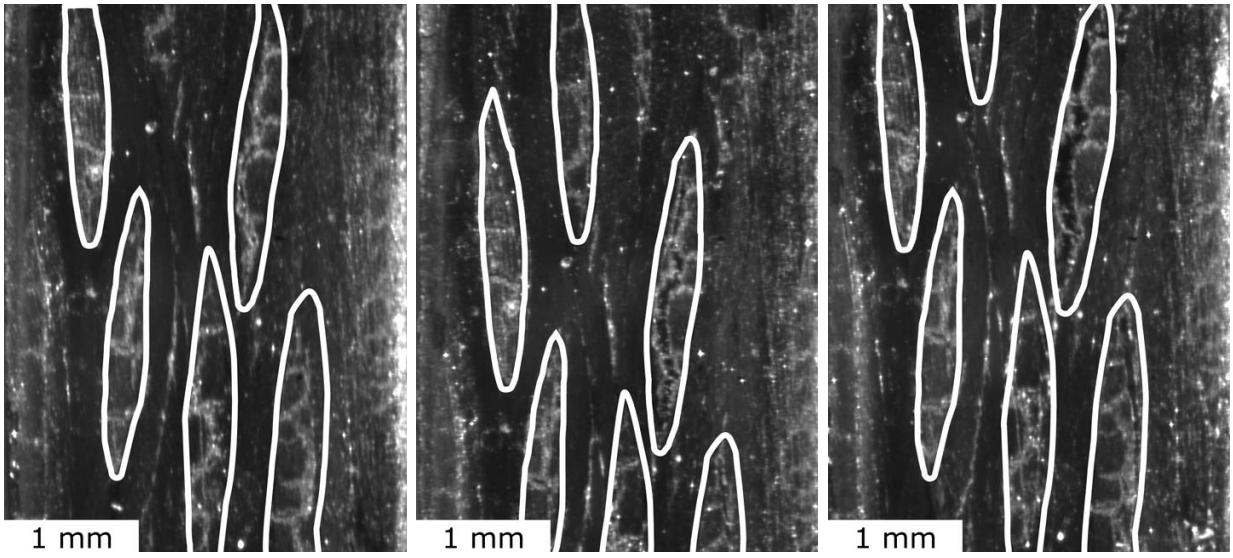

(a) 45 % of UTS (b) 80% of UTS (c) 94% of UTS

Figure 5.14 Direction 2 sample aged for 4 months observed by the long distance microscope under different load levels at Wet-T_g - 28°C: a) 45%, b) 80%, c) 94% of UTS.

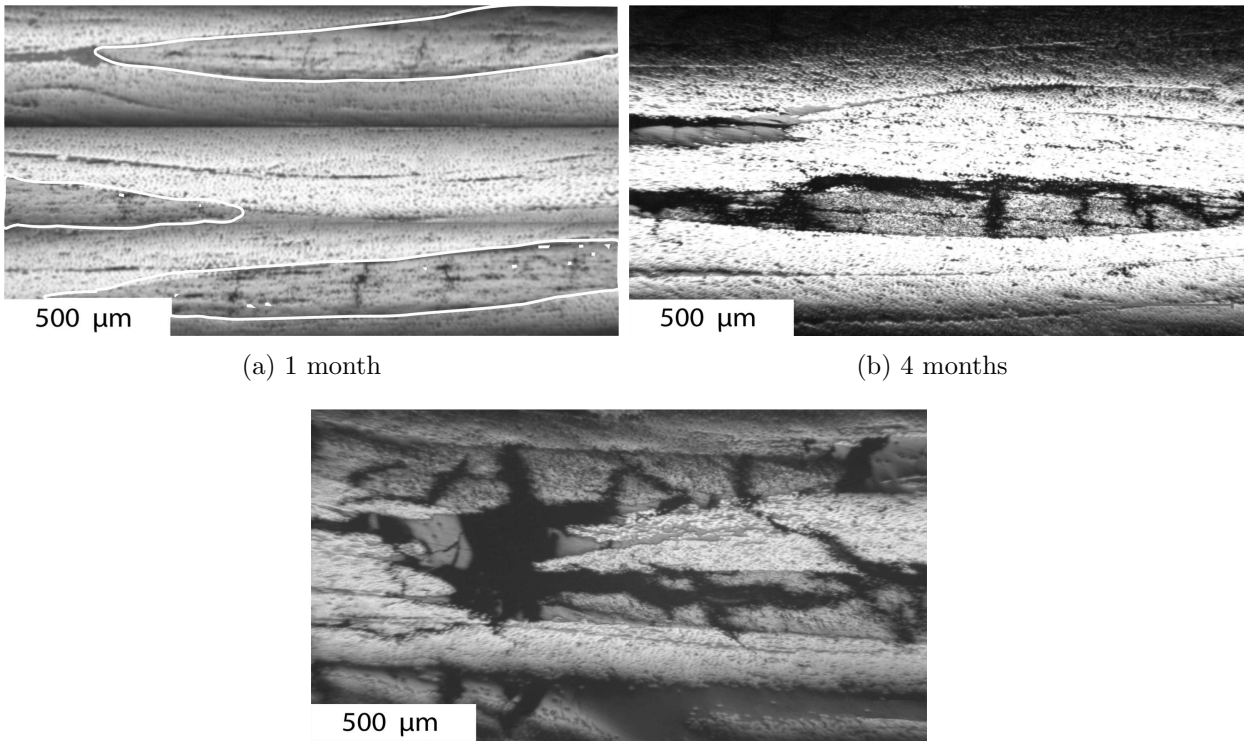

(a) 1 month (b) 4 months

(c) 9 months

Figure 5.15 Observation of Direction 2 specimens edges for different aging times at wet-T_g - 28°C.

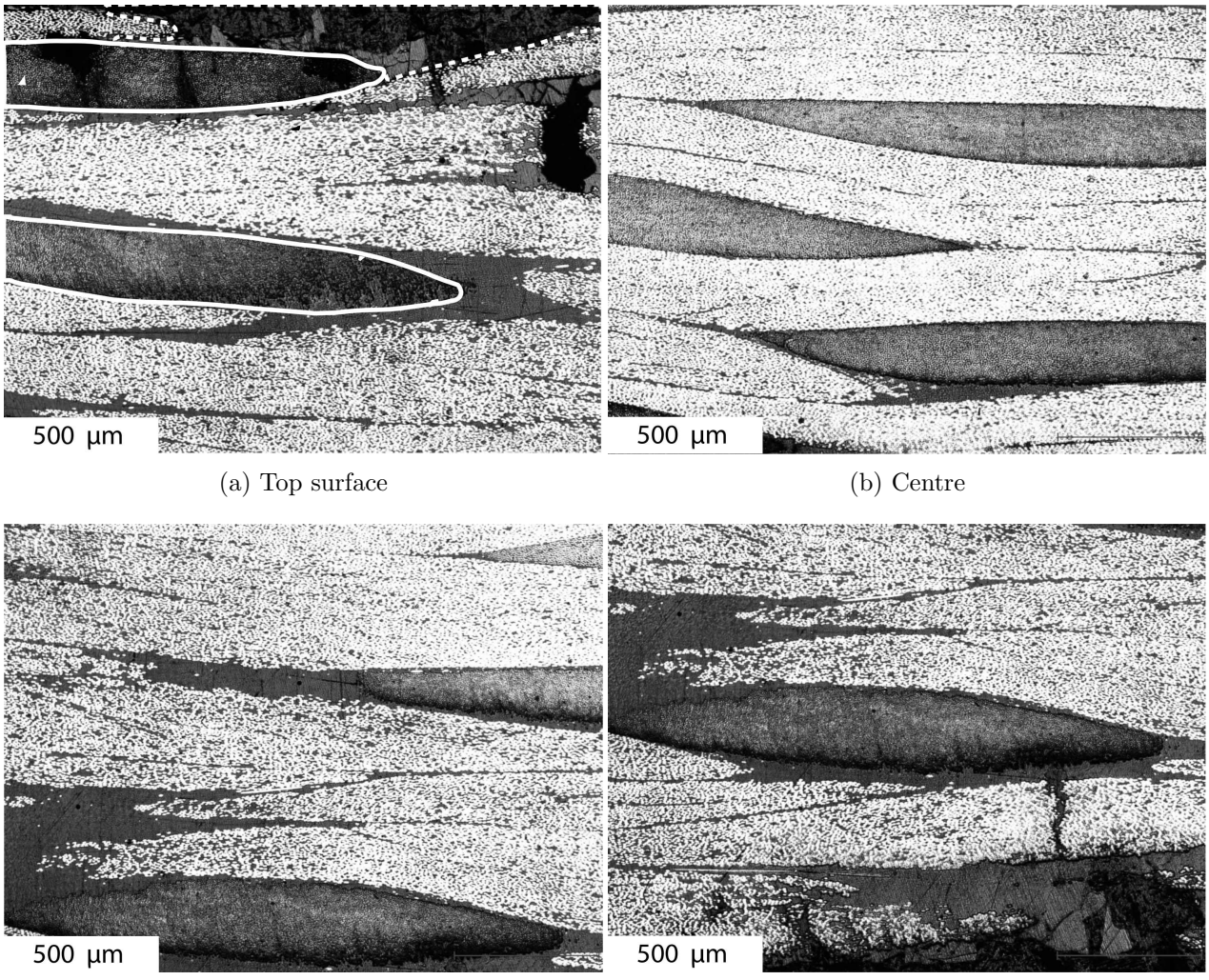

(a) Top surface

(b) Centre

(c) Centre

(d) Bottom surface

Figure 5.16 Cross-sections of Direction 1 specimen aged for 12 months at wet-T_g - 28°C. Images were taken near the a) top, at the b) and c) centre and at the d) bottom on the specimen. Damage was confined to the plies close to the specimen surface.

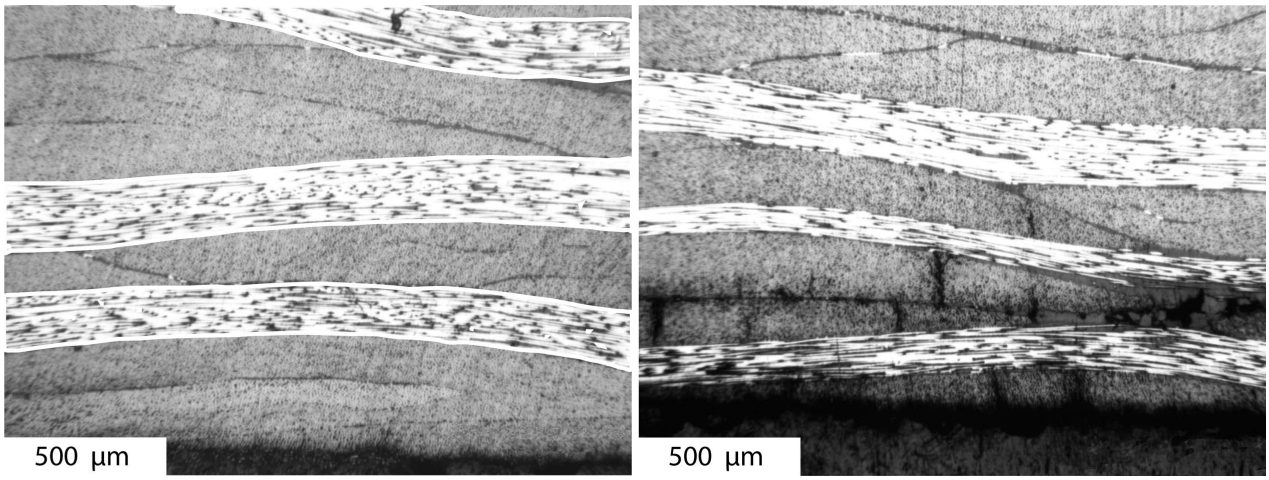

(a) Bottom, 4 months

(b) Bottom, 9 months

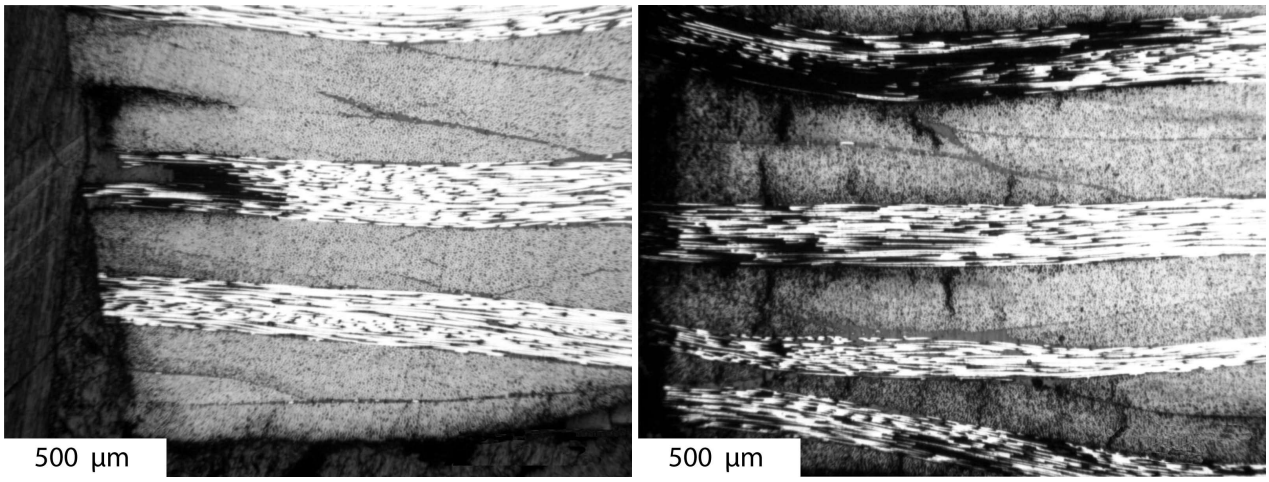

(c) Edge, 4 months

(d) Edge, 9 months

Figure 5.17 Cross-sections of Direction 2 specimen aged for 4 and 9 months at wet-T_g - 28°C. Images were taken at the a) bottom, 4 months, b) bottom, 9 months, near the c)edge, 4 months and the d) edge, 9 months of the cross-sections. Damage was confined to the plies close to the specimen surface.

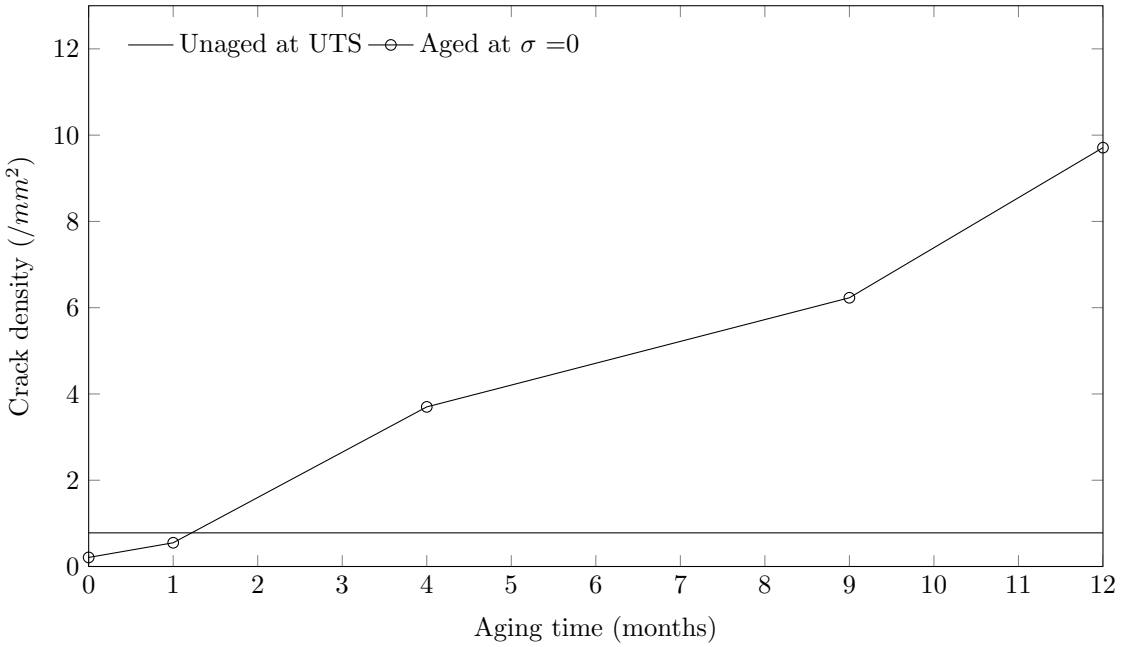

Figure 5.18 Comparison of the crack density on the edges of unaged specimens after reaching UTS at wet-T_g - 28°C, and aged Direction 1 specimens at different aging times without any loading.

than 1 month was already achieved before the beginning of the tensile test. The width and the density of the cracks due to aging are much more significant than tensile damage, which ultimately impacted the composite's UTS. It must be noted that almost all damage was concentrated in the ±60° yarns, pointing to a preferential path for the chemical aging process.

Figure 5.19 plots the maximum depth at which aging cracks were observed for Direction 1 and 2 samples as a function of aging time. It can be seen that edge cracks grow faster than surface cracks for composite samples, confirming once again the catalytic effect of fibres on the chemical aging process. Also, the fastest growth was observed on the Direction 2 samples' edges, along the 0° yarns. This progression was faster than the crack growth along the ±60° yarns for Direction 1 samples. This shows that the crack growth rate is related to the orientation of the yarns, and that transverse yarns act as 'highways' for crack propagation. The crack growth due to aging is a linear process for the observed aging times, showing that the chemical degradation has not reached a saturation point even after 17 months.

The UTS degradation was twice faster in Direction 1, when compared to Direction 2. This behavior can be explained by the position of the yarns in the textile in these 2 directions. In Direction 1 samples, the ±60° yarns are the most affected by the thermo-oxidative

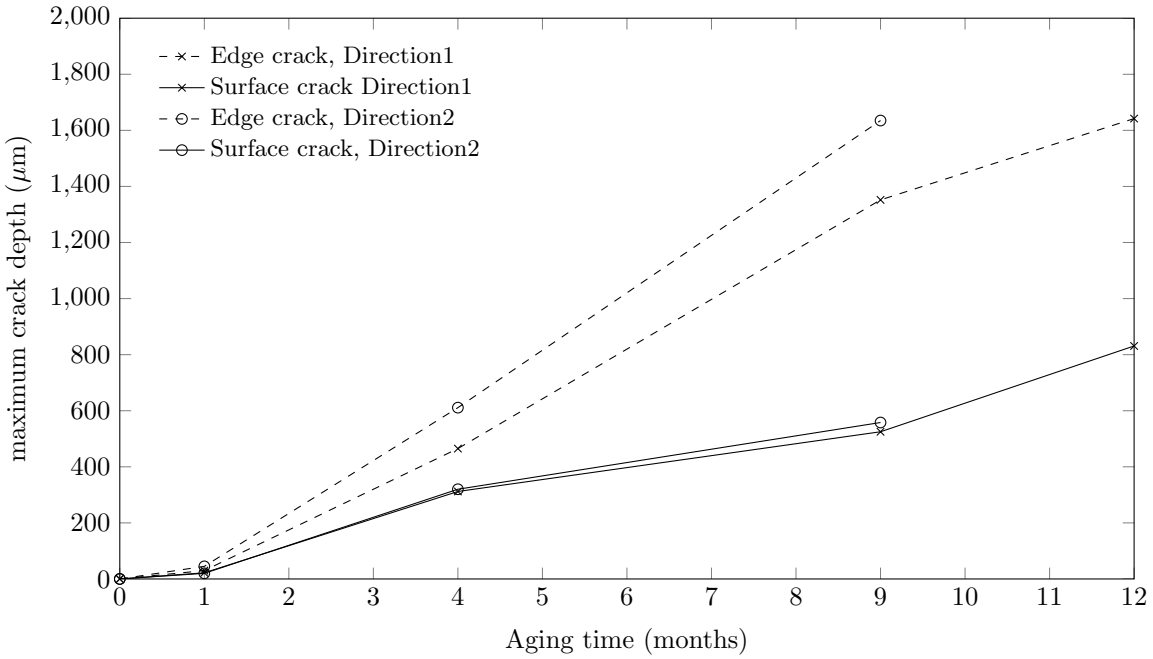

Figure 5.19 Maximum crack depth obtained from cross-section observation of aged samples in both directions

degradation. Since they represent 80 % of the yarns in the composite architecture, they provide a wide surface for the thermo-oxidative process to occur. For Direction 2 samples, the degradation is concentrated on the 0° yarns, which represent 20% of the yarns in the architecture. The onset and the rate of degradation are therefore lower. It is important to note the geometry influence on the UTS degradation. Since the edge cracks had a predominant influence in the decrease of UTS, the dimensions of the tested samples would influence the magnitude of this property degradation.

Finally, it is of interest to compare the durability of MVK10 composite systems relatively to the existing high temperature matrix systems in order to assess if the MVK10 matrix is a suitable replacement for the carcinogenic PMR-15 that had an operating temperature of 288°C (according to the wet-T_g - 28°C rule). Table 5.4 shows the strength retention of the material studied in this paper, a celion/PMR-15 uni-directional composite aged at 232°C (Nelson, 1984) and a carbon fabric/PMR15 aged at 204°C and 288°C studied by Bowles *et al.* (1995). Recall that the unidirectional composite was tested in short beam shear (SBS) tests, the fabric was tested under compression, while the braided composite studied in this paper was tested in tension, which means that direct comparisons cannot be made and these results should be interpreted with caution. Every material exhibited a significant degradation

Table 5.4 Strength retention for several aging times for 2 composite materials

Test	Aging time (months)	1	4	9	12	17
SBS	Celion/PMR15 (232°C)	100%	100%	96%	93%	75%
Compression	Carbon fabric/PMR15 (204°C)	100%	97 %	88%	83%	63%
Compression	Carbon fabric/PMR15 (288°C)	95%	75 %	NA	NA	NA
Tensile	Carbon/MVK10(Dir. 1)	100%	93 %	72%	71%	62%
Tensile	Carbon/MVK10(Dir. 2)	101%	101 %	86%	NA	NA

of strength over aging time, albeit different in rate. Strength degradation initiated after between 1 to 4 months of aging. This lag can be attributed to the time required by the thermo-oxidative process to create surface cracks in the composite, as those seen in Figure 5.17. The carbon fabric/PMR 15 strength decrease at 232°C was more important than that of the Celion/PMR15 composite. This confirms further that the architecture plays a significant role in the chemical aging process, with the transverse yarns accelerating the degradation of the surfaces. This comparison shows nevertheless that at wet-T_g - 28°C, the MVK10 composite behaves similarly to the other carbon/PMR 15 systems, but at a lower temperature.

5.5 Concluding remarks

The aging effect on the tensile strength and the failure mechanisms of a carbon/MVK10 triaxially braided composite was studied for two material directions. The damage evolution was monitored with the help of edge and cross-section microscopical observations. At wet-T_g - 28°C, the effect of physical aging on the composite's stiffness and density was negligible while the effect of chemical aging was gradually detrimental to the UTS. The main results are :

- The UTS decreased by 30 % in Direction 1 and by 20 % in Direction 2 after 9 months of aging.
- Cracks initiated after 1 month of aging, preferentially on the edge surfaces of the specimen and grew inward as aging time increased.
- The yarns that are transverse to the sample cutting direction act as catalyst to the aging process, creating anisotropy in the reduction of mechanical properties.
- The MVK-10 based composite studied in this work has shown similar relative performance to other high temperature matrices.

Thermal oxidation was the main agent behind UTS degradation in the triaxially braided composite, causing the initiation of transverse cracks on transverse yarns at the surface of the specimen. The crack density and depth increased during aging, further weakening the material. The thermal oxidation followed a preferential path, focusing on the yarns that were transverse to the specimen's edge. The FAA requirement for a maximum service temperature of wet-T_g - 28°C is suitable to prevent physical aging. However, it does not prevent UTS degradation caused by chemical aging when fibres are in contact with the oxidizing environment. Nevertheless, the MVK10 matrix tested in this work exhibited relative properties retention similar to that of PMR15, which might make this matrix a suitable replacement.

5.6 Acknowledgements

The authors wish to acknowledge the financial support of the National Sciences and Engineering Research Council (NSERC) of Canada, the Consortium for Research and Innovation in Aerospace in Quebec (CRIAQ), Rolls Royce Canada and Pratt and Whitney Canada. The first author also acknowledges additional financial support in the form of a scholarship by NSERC.

CHAPTER 6

GENERAL DISCUSSION

The aim of this thesis was to investigate the influence of temperature, viscoelasticity and aging on the mechanical properties of a carbon/MVK-10 braided composite. The results of this study are given in the three papers presented above. This section provides an extended discussion on the various aspect treated in the thesis.

6.1 Modeling aspects

A compromise was reached between the computation time, the model's complexity and the structure's geometric fidelity to create the RVE of the triaxially braided composite. Several assumptions, such as the constant yarns cross-sections and the constant packing factor inside a yarn are not realistic. The exact representation of the textile composite was therefore not achieved. However, the modeled RVE showed good agreement with the experimental results for the elastic properties' estimation, both at room temperature and at wet-T_g - 28°C, which suggests that deviations from the exact geometry might not have a significant effect on the overall properties. The study showed the potential of analytical and numerical homogenization techniques to evaluate textile composites' elastic properties and internal stresses.

6.2 Elastic properties of the braided composite

6.2.1 Viscoelasticity and temperature effects

The different performed tests showed the varying influence of viscoelasticity, temperature and aging on material properties. Viscoelastic behavior was expected in the material during the initial phase of the work. For that reason, the analytical and numerical homogenization models were extended to predict textile composites' viscoelastic behavior and their accuracy was evaluated. In the experimental phase of the study, creep tests were performed on three samples cut along direction 1 at wet-T_g - 28°C. Figure 6.1 displays the creep results for three load levels. The increase in strain during the test was lower than 3%. Viscoelasticity was therefore neglected for in-plane properties. Since Direction 2 is stiffer than Direction 1, viscoelasticity would be even lower in that direction. Overall, the textile composite retained its elastic properties at wet-T_g - 28°C, and displayed almost no viscoelastic behavior at this

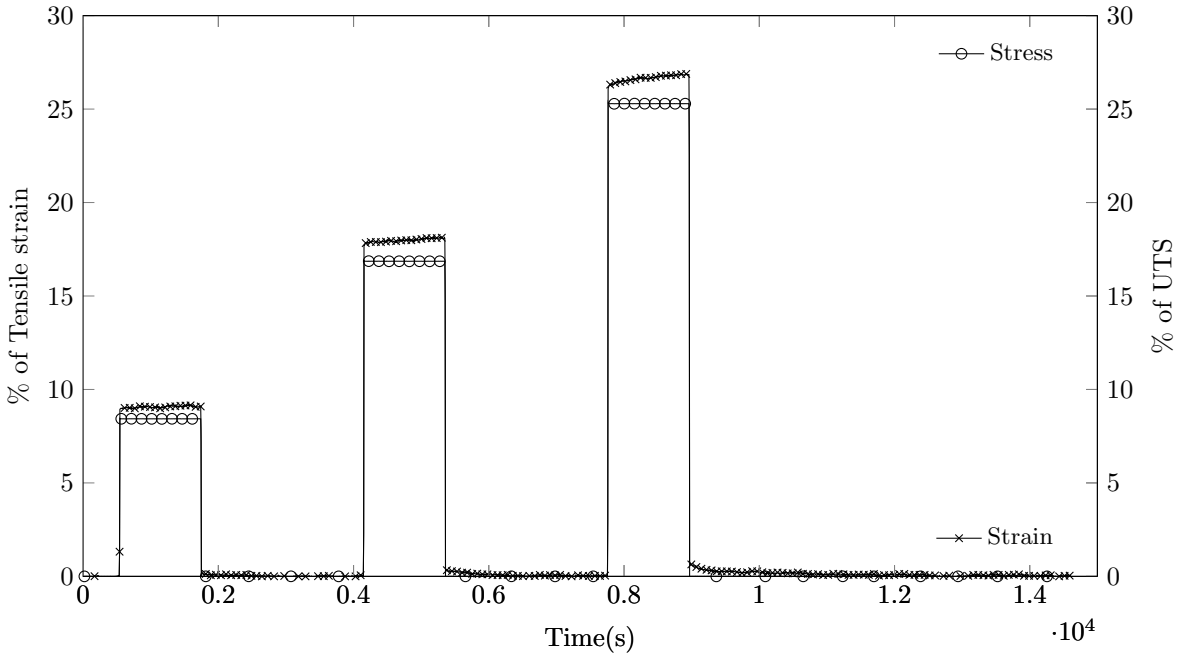

Figure 6.1 Creep testing in direction 1 at wet-T_g - 28°C.

temperature. Young's modulus decreased by 3.75% in Direction 1 and by 3.3% in Direction 2 between room temperature and wet-$T_g - 28$°C for the unaged samples. The yarns' presence in 3 directions ($0°/\pm 60°$), the high fibre volume fraction (56%), and the carbon fibres' high modulus limited the composite's viscoelastic behavior.

6.2.2 Physical aging

Additionally, physical aging was negligible at the testing temperature. Young's modulus was unchanged in Direction 1 and decreased by 2.2% in Direction 2 after 9 months of aging at wet-$T_g - 28$°C. It should be noted that the selected temperature had profound impacts on the observed properties of the carbon/MVK triaxially braided composite. At wet-T_g - 28°C , the test temperature is far enough from dry-T_g to limit the influence of viscoelasticity and physical aging, and delay chemical aging's influence. The limited quantity of available material determined the most appropriate testing temperature for tensile test samples. Higher test temperatures would increase these phenomena's influence on the material's mechanical behavior.

6.3 Ultimate Tensile Strength of the braided composite

6.3.1 Temperature effects

By opposition to the elastic properties, the material's UTS was quite affected by temperature and aging. The UTS decrease ranged from 5.7% in Direction 1 to 16% in Direction 2 at wet-T_g - 28°C, when compared to unaged samples tested at room temperature. These decreases are moderate when compared with the neat resin's 53% UTS reduction under the same conditions. Once again, the braided carbon fibre architecture shielded the composite from an important UTS reduction. The analytical and numerical analyses revealed that temperature changed the yarns' elastic properties and led to a redistribution of the internal stresses between the yarns. These variations correlated well with the experimentally observed changes in the failure modes and damage thresholds.

The MVK10's failure strain was lower than the carbon fibres' failure strain. In fact, all the composite samples tested during this project failed before reaching the carbon fibres' failure strain and displayed a brittle behavior. As such, the potential strength of the composite samples would be significantly higher with a different resin system, with a more diffuse damage evolution. The resin's low failure strain was most visible on Direction 1 samples' tensile tests, which only exhibited few matrix cracks and transverse cracks on the ±60° yarns before failure. These cracks usually represent the first step in textile composite damage, and should have been followed by yarn debondings and crack growth towards the uniaxial 0° yarns. This low failure strain could be a limiting factor for structural applications.

6.3.2 Chemical aging

The UTS decreased by 30 % in Direction 1 and by 20 % in Direction 2 after 9 months of aging at wet-T_g - 28°C (and 40 % in Direction 1 after 17 months of aging). Chemical aging had a stronger impact on the UTS reduction as aging time increased. The thermo-oxidative process severely affected the material's surfaces, creating crack networks that reduced the material's strength. This time, the braided architecture exacerbated the chemical aging effects, especially for samples cut in Direction 1. For these samples, the ±60° yarns which represents 80% of the yarns in the composite, acted as highways for the thermo-oxidative process, promoting crack growth that resulted in UTS reduction. Since the different yarns are interlaced in the textile composite, these cracks could easily reach the 0° yarns.

Additionally, the selected specimens' geometry had an influence on the results since the materials' oxidation was more severe on the surfaces where the fibres were in contact with air. The presence of significant cracks even at the specimens' edge is of concern, especially in fatigue testing where damage propagation due to cycling occurs. Finally, the samples aging

time should be put in perspective. In real flight conditions, the maximum service temperature is only reached during take-off, for 20 minutes or less. At an average of 4 flights per day, 1 year of aging would represent approximately 18 years of service. However, the components in an aircraft engine are subjected to simultaneous thermal and loading cycling. The aging and fatigue coupling could have disastrous effects on the material's mechanical properties.

CONCLUSION AND RECOMMENDATIONS

In this thesis, the influence of viscoelasticity, temperature and aging on the mechanical behavior of a textile composite was investigated using experimental, analytical and numerical tools.

The first step was to develop analytical and numerical frameworks to predict viscoelastic behavior in textile composites. Simulations were performed for both braided and woven textile architectures, at different stiffness contrasts and yarns volume fractions. The analytical framework accuracy was verified with the help of numerical simulations. An important finding of this study was that the analytical framework, combined with the Mori-Tanaka model, leads to relatively accurate predictions for both the permanent and transient parts. The textile composite that was studied in this project did not display viscoelastic behavior, due to the high yarn volume fraction. However, the framework remains relevant for higher temperature applications or lower yarn volume fractions in textile composites.

The second step was to investigate the temperature effect on the tensile behavior of the carbon/MVK10 triaxially braided composite material studied in this project. To achieve this goal, a series of room and high temperature tensile tests on both matrix and composite samples were performed. The tests on composite samples were performed along two different material directions and a dedicated replication technique was developed in order to track crack densities as a function of loading, for both test temperatures. Then, both analytical and numerical homogenization models were used to quantify the stress distribution at the yarns level as a function of the applied temperature. The study revealed that the impact of the temperature on the failure mechanisms of the textile composite was dependent on the loading direction. The textile architecture can play an important role in mitigating or increasing the temperature effects. It was observed that the yarns and matrix were more compliant than at room temperature at wet-T_g - 28°C, especially for the transverse and shear properties. These changes had negligible effects on the composite's elastic properties in both directions. However, they created local stress redistributions at the yarns level, which in turn affected the composite's Ultimate Tensile Strength. This evolution in the constituent elastic properties was reponsible for the changes in the stress profile at wet-T_g - 28°C in the yarns.

The final step consisted in the study of the aging effect on the tensile strength and the failure mechanisms of a carbon/MVK10 triaxially braided composite for two material directions. The damage evolution was monitored with the help of edge and cross-section microscopical observations. At wet-T_g - 28°C, the effect of physical aging on the composite's stiffness and

density was negligible while the effect of chemical aging was gradually detrimental to the UTS. It was found that the UTS decreased by 30 % in Direction 1 and by 20 % in Direction 2 after 9 months of aging. Cracks initiated after 1 month of aging, preferentially on the edge surfaces of the specimen and grew inward as aging time increased. The yarns that are transverse to the sample cutting direction acted as catalyst to the aging process, creating anisotropy in the reduction of mechanical properties. Thermal oxidation was the cause for UTS degradation, causing the initiation of transverse cracks on transverse yarns at the specimen's surface. The crack density and depth increased during aging, further weakening the material. The FAA requirement for a maximum service temperature of wet-T_g - 28°C is suitable to prevent physical aging. However, it does not prevent UTS degradation caused by chemical aging when fibres are in contact with the oxidizing environment. Nevertheless, the MVK10 matrix tested in this work exhibited relative properties retention similar to that of PMR15, which might make this matrix a suitable replacement.

The study showed that the matrix properties' changes at elevated temperatures do not necessarily affect the triaxially braided composite. For example, viscoelasticity and physical aging of the matrix did not affect the composite's properties, thanks to the carbon braided architecture. The UTS decrease due to the temperature was moderate and dependent on the loading direction. Chemical aging was gradually detrimental to the UTS and more pronounced in specific directions, due to the catalytic effect of the fibres on the thermo-oxidative process.

Recommendations for future work

- **Numerical simulation of the behavior of textile composites.** The research on the development of integrated and automated FE modellers for textile composites is still ongoing. The creation of textile architectures from idealized yarns geometries is the dominant procedure today. However, high fibre volume fractions, variable yarn cross-sections, yarn interpenetrations and localized geometries are many of the problems faced by this approach. For now, manual input is still required to overcome these problems. An alternative approach consists in the creation of RVEs from tomography imaging. This technique enables the creation of the exact geometry of the studied textile composite material, including defects. It would provide substantial benefits, especially as the field focuses on damage mechanisms and moves away from bulk properties estimations. However, the high price and computational costs of tomography and the manual input required to create the numerical geometries are still impediments to a more widespread use of this technique. However, automation efforts from the

tomographic representation to the numerical geometry would be beneficial.

- **Modeling failure of textile composites at high temperature.** Considerable efforts are deployed towards modeling failure in composite materials, including textile architectures. The extension of these efforts to take into account temperature effects still requires substantial experimental work. A reproduction of the present thesis with a cheaper material and into higher scale would provide a good basis to take into account temperature effects into damage modeling. The first step would be to produce UD composites, laminates as well as textile composite with different architectures from the same fibres and matrix. The UD and laminates would provide the necessary input on materials and yarns properties to model the damage in textile composites at elevated temperature. Additional loading conditions would provide a better insight into the mechanical behavior of the material. This layered approach, i.e studying the same material with different architectures (UD, laminate, woven, braided) would also be a good way to better understand and separate material properties, architecture effects and the temperature influence.

- **Out of plane viscoelastic behavior.** High fibre volumes, carbon fibres, and the presence of yarns in different orientations limit the influence of viscoelastic behavior for in-plane properties of textile composites. However, the lack of yarn orientations in the thickness direction of 2D textile composites, combined with the high anisotropy of carbon fibres, creates the potential of viscoelastic behavior in the thickness direction. An investigation of this behavior could be of interest for composites' bolted assemblies, or parts subjected to multiaxial loading.

- **Modeling chemical aging influence on UTS**. This study established that the UTS was negatively affected by the thermal-oxidation process. Modeling the kinetics of oxidation process requires additional investigation and modeling of the oxygen diffusivity in the resin and the composites. This step is necessary before modeling the effect of chemical degradation on the failure of textile composites.

REFERENCES

ABADIE, M., VOYTEKUNAS, V. and RUSANOV, A. (2006). State of the art organic matrices for high performance composites: A review. *Iranian Polymer Journal*, 15, 65–77.

ANDREWS, R. D. and TOBOLSKY, A. V. (1951). Elastoviscous properties of polyisobutylene. IV. Relaxation time spectrum and calculation of bulk viscosity. *Journal of Polymer Science*, 7, 221 – 242.

BENVENISTE, Y. (1987). A new approach to the application of Mori-Tanaka's theory in composite materials. *Mechanics of Materials*, 6, 147 – 157.

BERTIN, M., TOUCHARD, F. and LAFARIE-FRENOT, M.-C. (2010). Experimental study of the stacking sequence effect on polymer/composite multi-layers submitted to thermomechanical cyclic loadings. *International Journal of Hydrogen Energy*, 35, 11397 – 11404. Hyceltec 2009 Conference.

BEURTHEY, S. and ZAOUI, A. (2000). Structural morphology and relaxation spectra of viscoelastic heterogeneous materials. *European Journal of Mechanics - A/Solids*, 19, 1 – 16.

BEYLER, C. L. and HIRSCHLER, M. M. (2001). *SFPE Handbook of Fire Protection Engineering*, NFPA, Quincy, MA, chapitre Thermal Decomposition of Polymers. Troisième édition.

BIOT, M. A. (1954). Stress-strain relations in anisotropic viscoelasticity and relaxation phenomena. *Journal of Applied physics*, 25, 1385 – 1391.

BORNERT, M., BRETHEAU, T. and GILORMINI, P. (2001). *Homogeneisation en mecanique des materiaux 2 - Comportements non lineaires et problemes ouverts*. Hermes Science Publications, Paris.

BOWLES, K., ROBERTS, G. and KAMVOURIS, J. (1995). Long-term isothermal aging effects on carbon fabric-reinforced pmr-15 composites : compression strength. Rapport technique, NASA.

BRADSHAW, R. D. and BRINSON, L. C. (1997). Physical Aging in Polymers and Polymer Composites: An Analysis and Method for Time-Aging Time Superposition. *Polymer Engineering and Science*, 37, 31 – 44.

BRENNER, R., MASSON, R., CASTELNAU, O. and ZAOUI, A. (2002). A quasi-elastic affine formulation for the homogenized behavior of nonlinear viscoelastic polycristals and composites. *European Journal of Mechanics - A/Solids*, 21, 943 – 960.

BRENNER, R. and SUQUET, P. (2013). Overall response of viscoelastic composites and polycrystals: exact asymptotic relations and approximate estimates. *International Journal of Solids and Structures*, 50, 1824 – 1838.

BRINSON, L. C. and GATES, T. S. (1994). Viscoelasticity and aging of polymer matrix composites. *International Journal of Solids and Structures*, 32, 827 – 846.

BRINSON, L. C. and GATES, T. S. (2000). Effects of physical aging on long term creep of polymers and polymer matrix composites. *Comprehensive composite materials*, 2, 333 – 368.

BUDIANSKY, B. (1965). On the elastic moduli of some heterogeneous materials. *Journal of the Mechanics and Physics of Solids*, 13, 223 – 227.

C. SAUCIER, J. L. and PAILLIER, R. (2003). The tensile behavior of carbon fibers at high temperatures up to 2400 °C. *Carbon*, 715 – 725.

CHAMIS, C. (1989). Mechanics of composite materials: Past, present and future. *Journal of Composite Technology and Research*, 11, 3 – 14.

CHOU, T. W. and ISHIKAWA, T. (1983). One-dimensional micromechanical analysis of woven fabric composites. *AIAA Journal*, 21, 1714–1721.

CROCHON, T., KAMAL, M., BARNOS, M., LÉVESQUE, M. and LI, C. (2014). Thermal stability and evolution of the mechanical properties of an aerospace polyimide at high thermal stability and evolution of the mechanical properties of an aerospace polyimide at high temperature. *Submitted to Polymer Degradation and Stability*.

DUNN, M. L., LEDBETTER, H., HEYLIGER, P. R. and CHOI, C. S. (1996). Elastic constants of textured short-fibers composites. *J. Mech. Phys. Solids*, 44, 1509 – 1541.

EL MOURID, A. (2011). Modeling of the mechanical behavior of a braided composite at high temperature. Rapport technique, École Polytechnique de Montréal.

EL MOURID, A., BROCHU, M., GANESAN, R. and LÉVESQUE, M. (2014). Tensile failure analysis of a textile braided composite submitted to high temperature. *Journal*.

ESHELBY, J. D. (1957). The determination of the elastic field of an ellipsoidal inclusion, and related problems. *Proceedings of The Royal Society A*, 241, 376 – 396.

FAA (2001). Material qualification and equivalency for polymer matrix composite material systems. Rapport technique, Federal Aviation Administration.

FERRARI, M. (1990). Asymmetry and the high concentration limit of the mori-tanaka effective medium theory. *Mechanics of Materias*, 11, 251 – 256.

FERRY, J. D. (1980). *Viscoelastic Properties of Polymers, 3rd edn.* John Wiley and Sons, New York.

GAVAZZI, A. and LAGOUDAS, D. (1990). On the numerical evaluation of Eshelby's tensor and its application to elastoplastic fibrous composites. *Computational Mechanics*, 7, 13 – 19.

GOMMERS, B., I.VERPOEST and HOUTTE, P. (1998a). The mori-tanaka method applied to textile composite materials. *Acta Materialia*, 46, 2223 – 2235.

GOMMERS, B., VERPOEST, I. and HOUTTE, P. V. (1998b). Analysis of knitted fabric reinforced composites: Part i. fibre orientation distribution. *Composites Part A*, 29, 1579 – 1588.

HASHIN, Z. (1966). Viscoelastic fibre reinforced materials. *AIAA Journal*, 4, 1411 – 1417.

HASHIN, Z. (1970). Complex moduli of viscoelastic composites - II Fibre reinforced materials. *International Journal of Solids and Structures*, 6, 797 – 807.

HASHIN, Z. and SHTRIKMAN, S. (1962). A variational approach to the theory of the elastic behavio of multiphase materials. *J. Mech. Phys. Solids*, 11, 127 – 140.

HAYES, B. S. and GAMMON, L. (2010). *Optical microscopy of fiber-reinforced composites.* ASM international.

HERSHEY, A. V. (1954). The elasticity of an isotropic aggregate of anisotropic cubic crystals. *Journal of Applied Mechanics*, 21, 236 – 240.

HILL, R. (1965). A self-consistent mechanics of composite materials. *Journal of the Mechanics and Physics of Solids*, 13, 213 – 222.

HUYSMAN, G., VERPOEST, I. and HOUTTE, P. V. (1998). A poly-inclusion approach for the elastic modelling of knitted fabric composites. *Acta Materialia*, 46, 3003 – 3013.

ISHIKAWA, T. and CHOU, T.-W. (1982). Elastic behavior of woven hybrid composites. *Journal of Composite Materials*, 16, 2–19.

IVANOV, D. S., BAUDRY, F., BROUCKE, B. V. D., LOMOV, S. V., XIE, H., VERPOEST, I. and CURRENT, K. (2009). Failure analysis of triaxialy braided composites. *Composites Science and Technology*, 69, 1372 – 1380.

KIM, H. J. and SWAN, C. C. (2003). Voxel-based meshing and unit-cell analysis of textile composites. *International Journal for Numerical Methods in Engineering*, 56, 977–1006.

KIRBY, A. J. (1992). *Polyimides: Materials, Processing and Applications*, vol. 5, Number 11, Report 59. Rapra Technology Limited.

KOBAYASHI, S. and TAKEDA, N. (2002). Experimental characterization of microscopic damage behavior in carbon/bismaleimide composite effects of temperature and laminate configuration. *Composites Part A: Applied Science and Manufacturing*, 33, 1529 – 1538.

LAFARIE-FRENOT, M. (2006). Damage mechanisms induced by cyclic ply-stresses in carbon–epoxy laminates: Environmental effects. *International Journal of Fatigue*, 28, 1202 – 1216. The Third International Conference on Fatigue of Composites The Third International Conference on Fatigue of Composites.

LAFARIE-FRENOT, M., ROUQUIÉ, S., HO, N. and BELLENGER, V. (2006). Comparison of damage development in c/epoxy laminates during isothermal ageing or thermal cycling. *Composites Part A: Applied Science and Manufacturing*, 37, 662 – 671. Internal Stresses in Polymer Composites.

LAHELLEC, N. and SUQUET, P. (2007). Effective behavior of linear viscoelastic composites: A time-integration approach. *International Journal of Solids and Structures*, 44, 507 – 529.

LANG, E. J. and CHOU, T.-W. (1998). The effect of strain gage size on measurement errors in textile composite materials. *Composites Science and Technology*, 58, 539 – 548.

LAWS, N. and MCLAUGHLIN, R. (1978a). Self-consistent estimates for the viscoelastic creep compliances of composite materials. *Proceedings of the Royal Society of London A*, 359, 251 – 273.

LAWS, N. and MCLAUGHLIN, R. (1978b). Self-consistent estimates for the viscoelastic creep compliances of composite materials. *Proceedings of the Royal Society of London A*, 359, 251 – 273.

LEVEQUE, D., SCHIEFFER, A., MAVEL, A. and MAIRE, J.-F. (2005). Analysis of how thermal aging affects the long-term mechanical behavior and strength of polymer-matrix composites. *Composites Science and Technology*, 65, 395 – 401. JNC13-AMAC-Strasbourg.

LÉVESQUE, M., DERRIEN, K., MISHNAEVSKY JR., L., BAPTISTE, D. and GILCHRIST, M. D. (2004). A micromechanical model for nonlinear viscoelastic particle reinforced polymeric composite materials at undamaged state. *Composites Part A: Applied Science and Manufacturing*, 35, 905 – 913.

LÉVESQUE, M., GILCHRIST, M. D., BOULEAU, N., DERRIEN, K. and BAPTISTE, D. (2007). Numerical inversion of the Laplace – Carson transform applied to homogenization of randomly reinforced linear viscoelastic media. *Computational Mechanics*, 40, 771 – 789.

LI, F., HUANG, L., SHI, Y., JIN, X., WU, Z., SHEN, Z., CHUANG, K. C., LYON, R. E., HARRIS, F. W. and CHENG, Z. D. (1999). Thermal degradation mechanism and thermal mechanical properties of two high-performance aromatic polyimide fibers. *Journal of Macromolecular Science, Part B: Physics*, 38, 107 – 122.

LI, S., ZHOU, C., YU, H. and LI, L. (2011). Formulation of a unit cell of a reduced size for plain weave textile composites. *Computational Materials Science*, 50, 1770 – 1780.

LOMOV, S., BERNAL, E., IVANOV, D., KONDRATIEV, S. and VERPOEST, I. (2005). Homogenisation of a sheared unit cell of textile composites: FEA and approximate inclusion model. *Revue europeenne des elements finis*, 14, 709 – 728.

LOMOV, S., IVANOV, D., TRUONG, T., VERPOEST, I., BAUDRY, F., BOSCHE, K. V. and XIE, H. (2008). Experimental methodology of study of damage initiation and development in textile composites in uniaxial tensile test. *Composites Science and Technology*, 68, 2340 – 2349.

LOMOV, S. V., IVANOV, D. S., VERPOEST, I., ZAKO, M., KURASHIKI, T., NAKAI, H. and HIROSAWA, S. (2007). Meso-FE modelling of textile composites: Road map, data flow and algorithms. *Composite Science and Technology*, 67, 1870 – 1891.

LOWE, A., FOX, B. and OTIENO-ALEGO, V. (2002). Interfacial ageing of high temperature carbon/bismaleimide composites. *Composites Part A: Applied Science and Manufacturing*, 33, 1289 – 1292.

MARTIN, R., éditeur (2008). *Ageing of Composites Ageing of Composites Ageing of composites*. Woodhead publishing limited.

MONSTESANO, J., SELEZNEVA, M., POON, C., FAWAZ, Z. and BEHDINAN, K. (2011). Application of fiber optic sensors for elevated temperature testing of polymer matrix composite materials. *Science and Engineering of Composite Materials Science and Engineering of Composite Materials Science and Engineering of Composite Materials*, 18.

MONTESANO, J. (2012). *Fatigue damage characterization of braided and woven fiber reinforced polymer matrix composites at room and elevated temperatures.* Ph.D thesis, Ryerson University.

MONTESANO, J., FAWAZ, Z., BEHDINAN, K. and POON, C. (2013). Fatigue damage characterization and modeling of a triaxially braided polymer matrix composite at elevated temperatures. *Composite structures*, 101, 129–137.

MORI, T. and TANAKA, K. (1973). Average stress in matrix and average elastic energy of materials with misfitting inclusions. *Acta Metallurgica et Materialia*, 21, 597 – 629.

MOURID, A. E., GANESAN, R. and LÉVESQUE, M. (2013). Comparison between analytical and numerical predictions for the linearly viscoelastic behavior of textile composites. *Mechanics of Materials*, 58, 69 – 83.

MURA, T. (1982). *Micromechanics of Defects in Solids.* Kluwer Academic Publishers, Dordrecht, Netherlands.

NA, W.-J., AHN, H.-C., PARK, K.-M., KANG, H.-M. and YU, W.-R. (2012). In-situ damage monitoring of textile compsites using x-ray computed tomography. *15th european conference on composite materials, Venice.*

NAIK, N. K. and SHEMBEKAR, P. (1992). Elastic behavior of woven fabric composites: I-lamina analysis. *Journal of Composite Materials*, 26, 2196 – 2225.

NELSON, J. B. (1984). Long-term thermal aging of two graphite/polyimide composite materials. Rapport technique, NASA.

ODEGARD, G. and KUMOSA, M. (2000). Elastic-plastic and failure properties of a unidirectional carbon/pmr-15 composite at room and elevated temperatures. *Composites Science and Technology*, 60, 2979 – 2988.

OKABE, Y., YASHIRO, S., KOSAKA, T. and TAKEDA, N. (2000). Detection of transverse cracks in cfrp composites using embedded fiber bragg grating sensors. *Smart Materials and Structures*, 9, 832.

POCHIRAJU, K. and TANDON, G. P. (2009). Interaction of oxidation and damage in high temperature polymeric matrix composites. *Composites Part A: Applied Science and Manufacturing*, 40, 1931 – 1940. Special Issue: CompTest 2008.

REKIK, A. and BRENNER, R. (2011). Optimization of the collocation inversion method for the linear viscoelastic homogenization. *Mechanics Research Communications*, 38, 305 – 308.

RICAUD, J.-M. and MASSON, R. (2009). Effective properties of linear viscoelastic heterogeneous media: Internal variables formulation and extension to ageing behaviours. *International Journal of Solids and Structures*, 46, 1599 – 1606.

ROBITAILLE, F., LONG, A., JONES, I. and RUDD, C. (2003). Automatically generated geometric descriptions of textile and composite unit cells. *Composites Part A: Applied Science and Manufacturing*, 34, 303 – 312.

RUGGLES-WRENN, M. B. and BROECKERT, J. L. (2009). Effects of Prior Aging at 288C in Air and in Argon Environments on Creep Response of PMR-15 Neat Resin. *Journal of Applied Polymer Science*, 111, 228 – 236.

SANKAR, B. V. and MARREY, R. V. (1997). Analytical method for micromechanics of textile composites. *Composites Science and Technology*, 57, 703 – 713.

SCHAPERY, R. A. (1962). Approximate methods of transform inversion for viscoelastic stress analysis. *Proceedings of the 4th US National Congress of Applieds Mechanics*. vol. 2, 1075 – 1085.

SCHAPERY, R. A. (1964). Application of thermodynamics to thermomechanical, fracture, and birefringent phenomena in viscoelastic media. *Journal of Applied physics*, 35, 1451 – 1465.

SCHOEPPNER, G., TANDON, G. and RIPBERGER, E. (2007). Anisotropic oxidation and weight loss in pmr-15 composites. *Composites Part A: Applied Science and Manufacturing*, 38, 890 – 904.

SELEZNEVA, M., MONTESANO, J., FAWAZ, Z., BEHDINAN, K. and POON, C. (2011). Microscale Experimental Investigation of Failure Mechanisms in Off-axis Woven Laminates at Elevated Temperatures. *Composites Part A*, 42, 1756 – 1763.

STRUIK, L. C. E. (1978). *Physical Aging in Amorphous Polymer and other Materials*. Elsevier Scientific Publishing Company.

TALON, O. (2007). Polyimides linéaires. Techniques de l'ingénieur.

TAN, P., TONG, L. and STEVEN, G. (1997). Modelling for predicting the mechanical properties of textile composites,a review. *Composites Part A: Applied Science and Manufacturing*, 28, 903 – 922.

TANDON, G., POCHIRAJU, K. and SCHOEPPNER, G. (2006). Modeling of oxidative development in pmr-15 resin. *Polymer Degradation and Stability*, 91, 1861 – 1869.

TANDON, G., POCHIRAJU, K. and SCHOEPPNER, G. (2008). Thermo-oxidative behavior of high-temperature pmr-15 resin and composites. *Materials Science and Engineering: A*, 498, 150 – 161. International Conference on Recent Advances in Composite Materials (ICRACM 2007).

TUTTLE, M. E. and BRINSON, H. F. (1986). Prediction of the long-term creep compliance of general composite laminates. *Experimental Mechanics*, 26, 89 – 102.

UPADHYAYA, P. and UPADHYAY, C. (2011). A three-dimensional micromechanical model to predict the viscoelastic behavior of woven composites. *Composite Structures*, 93, 2733 – 2739.

VERPOEST, I. and LOMOV, S. V. (2005a). Virtual textile composites software wisetex: Integration with micro-mechanical, permeability and structural analysis. *Composites Science and Technology*, 65, 2563 – 2574. 20th Anniversary Special Issue.

VERPOEST, I. and LOMOV, S. V. (2005b). Virtual textile composites software wisetex: Integration with micro-mechanical, permeability and structural analysis. *Composites Science and Technology*, 65, 2563 – 2574. 20th Anniversary Special Issue.

VU, D. Q., GIGLIOTTI, M. and LAFARIE-FRENOT, M. C. (2012). Experimental characterization of thermo-oxidation-induced shrinkage and damage in polymer–matrix composites. *Composites Part A: Applied Science and Manufacturing*, 43, 577 – 586.

WONG, C., LONG, A., SHERBURN, M., ROBITAILLE, F., HARRISON, P. and RUDD, C. (2006). Comparisons of novel and efficient approaches for permeability prediction based on the fabric architecture. *Composites Part A: Applied Science and Manufacturing*, 37, 847 – 857. Selected Contributions from the 7th International Conference on Flow Processes in Composite Materials held at University of Delaware, USA.

ZAOUI, A. (2002). Continuum micromechanics: Survey. *Journal of Engineering Mechanics*, 128, 808 – 816.

APPENDIX A

Crack density counting

This appendix section covers the methodology used to count the number of cracks form edge replicas and cross-sections. The edge replicas were obtained at different load levels for room temperature and wet-$T_g - 28°C$ tests.

Figure A is used for illustrating the crack counting. This figure shows an edge replica of a Direction 1 sample at room temperature at 80% of UTS. The 0° yarns appear as long strands while the ±60° yarns appear as ellipses. Several transverse cracks can be seen in the picture. A characteristic transverse crack is circled and is counted as 1 crack. When a transverse cracks spans over 2 different yarns, it is counted as 2 cracks since they would have a bigger influence on the stiffness degradation. In this image, 9 cracks can be counted, and divided by the replica area of 2.5 mm^2 lead to a crack density of 3.6 cracks/mm^2. The cracks were counted on 10 images at different locations of the same replica, covering an area of 25 mm^2, to provide a better representation of the crack density across a replica. The replication procedure was performed on one sample for each direction and temperature.

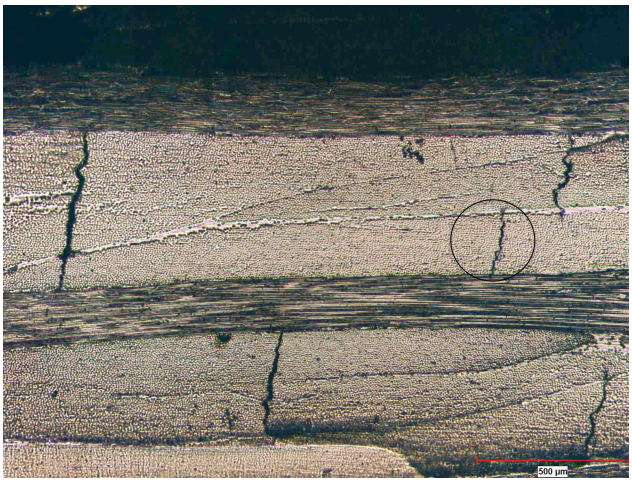

Figure A.1 Direction 1 edge replica at 80% of UTS.

APPENDIX B

Tested samples data

This appendix section provides information about all tested samples. For confidentiality reasons, every composite property was normalized by the equivalent matrix property at room temperature for unaged samples. E_m, σ_m^u and ε_m^u refer to the matrix Young's modulus, ultimate tensile strength and tensile strain at room temperature. Table B.1 presents the data for room temperature tests while Table B.2 presents experimental results at wet-$T_g - 28°$C. Averages as well as the standard deviation of each test group are provided.
The modulus and strength retention for each of the aged samples are presented for Direction 1 (Table B.3) and Direction 2 samples (Table B.4). Averages as well as the standard deviation of each test group are provided.

Table B.1 Tensile testing of unaged composite samples at room temperature

Sample	E_c/E_m	E_c/E_m at failure	σ_c^u/σ_m^u	$\varepsilon_c^u/\varepsilon_m^u$
Direction 1-1	8.75	7.92	8.2	0.95
Direction 1-2	8.82	7.74	8.3	1.01
Direction 1-3	8.93	7.76	8.6	1.00
Average Direction 1	**8.83**	**7.8**	**8.35**	**0.99**
Std deviation Direction 1	**0.090**	**0.098**	**0.2**	**0.03**
Direction 2-1	13.7	10.77	11.5	0.91
Direction 2-2	13.8	13.2	11.7	0.86
Direction 2-3	13.9	10.74	11.3	0.88
Average Direction 2	**13.8**	**11.8**	**11.5**	**0.88**
Std deviation Direction 2	**0.10**	**1.4**	**0.18**	**0.025**

Table B.2 Tensile testing of unaged composite samples at wet-$T_g - 28°C$

Sample	E_c/E_m	E_c/E_m at failure	σ_c^u/σ_m^u	$\varepsilon_c^u/\varepsilon_m^u$
Direction 1-4	8.48	8.37	7.7	0.88
Direction 1-5	8.40	8.21	8.1	0.92
Direction 1-6	8.27	8.30	7.9	0.91
Average direction 1	**8.37**	**8.29**	**7.9**	**0.90**
Std deviation Direction 1	**0.11**	**0.07**	**0.1**	**0.02**
Direction 2-4	13.44	9.86	9.2	0.70
Direction 2-5	13.22	10.69	10.2	0.80
Direction 2-6	13.28	10.58	10.4	0.82
Average direction 2	**13.30**	**10.40**	**9.9**	**0.78**
Std deviation Direction 1	**0.11**	**0.45**	**0.73**	**0.06**

]

Table B.3 Normalized tensile tests of Direction 1 composite samples after different aging times at wet-$T_g - 28°C$

Sample #	Aging time (months)	Modulus retention	UTS retention
Direction 1-7	1	101	99.7
Direction 1-8	1	95.5	97.2
Direction 1-9	1	100	103.7
Average	**1**	**99.5**	**1002**
Std deviation	**1**	**3.3**	**3.3**
Direction 1-10	4	101	94.6
Direction 1-11	4	97.3	99.4
Direction 1-12	4	102.2	84.0
Average	**4**	**100.5**	**92.7**
Std deviation	**4**	**2.5**	**7.9**
Direction 1-13	9	99.8	70.4
Direction 1-14	9	101.3	71.2
Direction 1-15	9	98.5	73.2
Average	**9**	**100.2**	**71.6**
Std deviation	**9**	**1.38**	**1.46**
Direction 1-16	12	97.3	71.5
Direction 1-17	12	95.8	66.4
Direction 1-18	12	102.9	72.6
Average	**12**	**99.0**	**70.2**
Std deviation	**12**	**3.7**	**3.3**
Direction 1-19	17	95.5	57.8
Direction 1-20	17	98.3	65.8
Direction 1-21	17	95.5	59.3
Average	**17**	**96.7**	**61.0**
Std deviation	**17**	**1.59**	**4.3**

]

Table B.4 Normalized tensile tests of Direction 2 composite samples after different aging times at wet-$T_g - 28°C$

Sample #	Aging time (months)	Modulus retention	UTS retention
Direction 1-7	1	95.2	107.2
Direction 1-8	1	103.3	114.8
Direction 1-9	1	93.4	96.5
Average	**1**	**97.3**	**106.2**
Std deviation	**1**	**5.2**	**9.17**
Direction 1-10	4	99.9	97.9
Direction 1-11	4	903.3	110.0
Direction 1-12	4	100.3	07.9
Average	**4**	**101.1**	**101.9**
Std deviation	**4**	**1.87**	**7.0**
Direction 1-13	9	98.3	76.0
Direction 1-14	9	95.6	89.7
Direction 1-15	9	99.5	73.2
Average	**9**	**97.8**	**79.6**
Std deviation	**9**	**1.95**	**8.8**